MEASUREMENT OF THE RATE OF HYDROGEN ATOM ABSTRACTION FROM METHANE AND ETHANE BY MUONIUM

By

Rodney James Snooks

B.Sc. (hons) Saint Mary's University, 1990

A THESIS SUBMITTED IN PARTIAL FULFILLMENT OF

THE REQUIREMENTS FOR THE DEGREE OF

MASTER OF SCIENCE

in

THE FACULTY OF GRADUATE STUDIES

CHEMISTRY

We accept this thesis as conforming

to the required standard

THE UNIVERSITY OF BRITISH COLUMBIA

1993

In presenting this thesis in partial fulfilment of the requirements for an advanced degree at the University of British Columbia, I agree that the Library shall make it freely available for reference and study. I further agree that permission for extensive copying of this thesis for scholarly purposes may be granted by the head of my department or by his or her representatives. It is understood that copying or publication of this thesis for financial gain shall not be allowed without my written permission.

(Signature)

Department of Chemistry

The University of British Columbia
Vancouver, Canada

Date April 30 1993

Abstract

Reaction rates for the gas-phase reactions

$$Mu + CH_4 \rightarrow MuH + CH_3$$

and

$$Mu + C_2H_6 \rightarrow MuH + C_2H_5$$

have been measured using μSR over the temperature ranges 626–821 K and 511–729 K respectively. The usual Arrhenius plots for each data set are linear. The measured parameters A are $5.7^{+4.8}_{-2.5} \times 10^{-8}$ and $1.0^{+0.7}_{-0.4} \times 10^{-9}$ cm^3 molecule^{-1} s^{-1}, and the parameters E_a, $24.66^{+0.88}_{-0.82}$ and $15.35^{+0.65}_{-0.59}$ kcal/mol respectively. The E_a values are 11.5 and 5.5 kcal/mol higher than for the corresponding H atom reactions. The very large increases in E_a seem to indicate drastic differences between the Mu and H variants of the title reactions, in location of the transition states on the potential energy surfaces. Also, for the Mu variants, the reaction rates seem to be reduced less for vibrationally excited states of CH_4 and C_2H_6 than for the ground states than is the case for the corresponding H atom reactions, an effect which contributes to the large increase in activation energy for Mu.

Table of Contents

List of Figures

List of Tables

Acknowlegements

I would like to thank my thesis advisor, Donald G. Fleming, for patient research direction and a "hands-off" attitude allowing me to pursue my many interests at U.B.C. Also owed thanks are the other members of our research group in my time at U.B.C.—Masa Senba, James Kempton, Susan Baer, Donald Arseneau, James Pan, and Mee Shelley—all of whom were invaluable helpers with the present study, and offered much help with technical details and theoretical interpretations.

As well, this thesis would not have been possible without the help of many engineers and technical workers at TRIUMF. Particularly notable were the contributions of George Clark, the designer of the reaction vessel used in the present study; Keith Hoyle and Curtis Ballard, μSR technical workers, who went beyond the call of job descriptions on many occasions; and members of TRIUMF's machine shop, for quality metal work, often on very short notice.

Lastly I would like to thank my favorite undergraduate professors, Jack Ginsburg and Robert Kruse, both of whom offered clear answers to my many questions, and without whom I may never have made it into graduate school.

Chapter 1

Introduction

1.1 Background and Motivation

The field of reaction kinetics calculations has become a particularly active area of chemical research in recent years (see [1–5] and references therein). Recent rapid advances in computer technology have allowed theorists to contemplate the possibility of truly accurate computations of gas-phase reaction rates from first principles (*ab initio*).

Experimental kinetics data are already available in abundance; see [6] and [7] for compilation of rate data for the abstraction reactions:

$$H + CH_4 \rightarrow H_2 + CH_3 \tag{1.1}$$

$$H + C_2H_6 \rightarrow H_2 + C_2H_5 \tag{1.2}$$

of which the title reactions

$$Mu + CH_4 \rightarrow MuH + CH_3 \tag{1.3}$$

$$Mu + C_2H_6 \rightarrow MuH + C_2H_5 \tag{1.4}$$

are isotopic variants. The data have been measured by a variety of methods. Another report [8] on the reaction (1.1) has appeared since the beginning of the present study. Also studied have been the hot tritium (T^*) variant of reaction (1.1) [9–12] and the H^* and T^* variants of reaction (1.2) [13, 14]. The substitution reaction

$$H_a + CH_4 \rightarrow CH_3H_a + H \tag{1.5}$$

Table 1.1: Selected rate data for $H + CH_4 \rightarrow H_2 + CH_3$.

T/K	$A/(10^{-10}\text{cm}^3\ \text{molecule}^{-1}\ \text{s}^{-1})$	$E_a/(\text{kcal mole}^{-1})$	Reference
426–747	1.0	11.7 ± 0.2	*a*
673–763	5.3	15.1	*b*
640–818	3.2	13.2 ± 0.8	*c*
827–1729	1.8	12.8 ± 0.2	*d*
400–1800	1.3	11.9 ± 0.2	*e*
1100–1800	3.3	11.5	*f*

a) Flow system and ESR detection of H atom [16].

b) Inhibition of the first limit in $H_2 + O_2$ by CH_4; $CH_3 + O_2$ and $CH_3 + H_2$ ignored [17].

c) Flow discharge system; k obtained from a fitting of 14 reactions [18].

d) Most recent study, measured by flash photolysis/shock tube technique [8].

e) From global fit to several data sets given in reference [18]. Consistent as well with compilation of Shaw [7].

f) Low pressure flames of $CH_4/H_2/O_2/N_2O$; $OH + CH_4$ and $H_2 + CH_3$ reactions neglected; k relative to $k(H + N_2O)$ [19].

Table 1.2: Selected rate data for $H + C_2H_6 \rightarrow H_2 + C_2H_5$.

T/K	$A/(10^{-10}\text{cm}^3\ \text{molecule}^{-1}\ \text{s}^{-1})$	$E_a/(\text{kcal mole}^{-1})$	Reference
281–347	0.83	9.1	*a*
357–544	1.8	9.2	*b*
503–753	3.1	9.8	*c*
876–1016	8.7	11.0 ± 0.2	*d*

a) H atoms produced by electrical discharge and monitored by spectroscopic measurement of reaction product with HgO [20].

b) Flow discharge system [21].

c) Simultaneous determination with rates of H atom reactions with CH_3 and C_2H_5 fragments [22].

d) H atoms monitored by atomic resonance absorption [23].

has recently [15] undergone a mechanistic study using deuterated methane (CD_4), which shows the reaction to proceed by a standard inversion mechanism. Selected experimental thermal rate data for the reaction (1.1) are shown in Table 1.1, and for reaction (1.2), in Table 1.2. The parameters listed are defined by the standard

Arrhenius equation $k = A\exp(-E_a/\mathrm{R}T)$, with E_a the activation energy and A the pre-exponential factor, reviewed in Chapter 2. The measured reaction rates are of course greater for C_2H_6 than for CH_4, as expected from the simplest of chemical arguments.

Thermal rate data for the T atom isotopic variant of reaction (1.1) is not available, and two studies [24, 25] for the D variant, in which the rate parameters were determined indirectly, were complicated by calibration problems, resulting in absolute measured rates of uncertain accuracy. However, in the study of reference [25], an E_a of 11.1 kcal/mol was found by comparison with H atom data of the same study, for which an E_a of 11.7 kcal/mol was measured. This isotope effect is in reasonable agreement with the theoretical calculations of Schatz *et al.* [26], discussed in Chapter 4.

As calculated reaction rates approach measured rates in accuracy, a detailed comparison between experimental data and the most accurate calculations should reveal the strengths and weaknesses of the theory underlining the calculations, allowing for further refinement of the theory and/or calculation methods. Well-characterized kinetic isotope effects allow a particularly meaningful comparison between the experimental and theoretical results. Isotopic substitution in reactants affects reaction rates in several ways. Of no real interest is the rate difference due to the difference in mean velocities, known as the "trivial" isotope effect, owing to the mass difference of the reactants. However, isotopic substitution also affects reaction rates due to the shifting of the energy levels of the rovibrational quantum states in reactants, products, and most importantly, in transition states, resulting from the change in mass. The mass difference changes both the energy spacing (density of states) and the value of the zero point energies (the difference between the ground state energy and zero) of these levels. In addition tunneling, the quantum phenomenon of particles passing through classically forbidden ("negative energy") regions, is more likely for lighter species than for heavier ones.

In general the zero point energy and/or tunneling effects on reaction kinetics are manifest more strongly in lighter isotopes. Accounting for these effects is the challenge facing reaction rate theory. Because of the complicated results of the relevant isotope effects, theoretical calculations giving results comparable to experiment for more than one isotopic combination for a given reaction are less likely to be in agreement fortuitously, and so examination of isotope effects gives a stringent test of theoretical calculations when compared to experiment.

Aside from being the lightest atom, hydrogen also has the highest mass ratio between its isotopes (T(3):D(2):H(1)) as compared to any other element; therefore it is the element displaying the greatest degree of isotopic effects in its behaviour. A further extension to this series is made possible by μSR, an experimental technique in use since the 1970's (see [27–30]) at the TRIUMF cyclotron in Vancouver. TRIUMF provides beams of the particle known as the muon, μ^-, and of its antiparticle μ^+, the latter being used in the present study.

The positive muon at high (~MeV) energies can capture an electron to form a system known as muonium (μ^+e^-, abbreviated Mu) [27]. Since the muon mass is ~1/9 that of the proton, 206 times that of the electron, the reduced mass of the combined system (defined as $m_\mu m_e/(m_\mu + m_e)$, with m's the particle masses of μ^+ and e^+) is virtually unchanged from that of the electron, as is the case for the H atom. As well, the charge of the muon is the same as for a proton. From elementary physics, the equation of motion of the electron in Mu is then essentially the same as that of the electron in H: that of an electron moving in a force field of a very heavy nucleus of unit positive charge. Muonium is therefore chemically equivalent to, and can be considered an isotope of hydrogen.

The mass of Mu, being only 1/9 that of the mass 1 a.u. isotope (H), and 1/27 that of tritium, leads to isotope effects of greater magnitude than those seen in conventional

chemical studies. For example, the standard heat of reaction ΔH° for the reaction (1.1) is [31] -2.6 kcal/mol; the zero point energy of MuH is [32] is $\sim$7.5 kcal/mol higher than for H_2 resulting in a ΔH° of 4.9 kcal/mol for the Mu variant reaction (1.3). For the corresponding reaction with C_2H_6 (1.2), Mu substitution raises ΔH° from -3.1 to 4.3 kcal/mol[1]. In both cases an exothermic reaction becomes endothermic. A striking example of a *kinetic* isotope effect is the abstraction reaction

$$\mathrm{Mu} + \mathrm{F_2} \rightarrow \mathrm{MuF} + \mathrm{F} \tag{1.6}$$

in which pronounced tunneling is obvious from the kinetics data [34]. The kinetic isotope effect is especially striking in comparison to data of corresponding H and D atom reactions, in which such tunneling is much less evident than for Mu.

The μSR technique allows observation of the chemical behaviour of Mu using equipment developed for nuclear and particle physics experiments. Together with conventional studies of H, D, and T, muonium studies can provide a wide range of kinetic isotope effects.

Being the simplest element, hydrogen is the most amenable to theoretical calculation of reaction rates. Hydrogen atom reactions have received more theoretical attention than those of any other species for this reason. The chemical reaction for which the most rate calculations exist is, predictably, the abstraction reaction

$$\mathrm{H_a} + \mathrm{H_bH_c} \rightarrow \mathrm{H_aH_b} + \mathrm{H_c} \tag{1.7}$$

for which completely *ab initio* calculations have reached the point of chemical accuracy (see [35]). This includes the isotopic variant

$$\mathrm{Mu} + \mathrm{H_2} \rightarrow \mathrm{MuH} + \mathrm{H} \tag{1.8}$$

[1] Using $\Delta H^\circ = 120 \pm 3$ kJ/mol for C_2H_5 from reference [33].

for which there is remarkably close agreement between Schatz' reactive scattering calculations [36] and rates measured by μSR [37]. This agreement represents one of the most impressive demonstrations of the utility of μSR.

The same level of accuracy has not been reached for the abstraction reaction (1.1) or the substitution reaction (1.5) but these have received much attention, being the simplest non-trivial reactions involving a hydrocarbon species, as well as key reactions in the combustion of methane; see [38] for many references, and [39, 40] for recent, *ab initio*, calculations. The calculations of Gonzalez-Lafont [39] *et al.* for the abstraction reaction (1.1) show fair general agreement with the shape of Arrhenius plots of the best available rate data, but calculations of the accuracy of those performed by Schatz on Mu + H_2 are not available. Also, some calculations exist for the analogous H + C_2H_6 reactions, but at a much more approximate level (see [41] and references within).

Clearly, theoretical study of the reaction dynamics of polyatomic molecules, though rapidly growing in feasibility, remains in its infancy. The complex nature of these dynamics, as compared to those found in reactions of diatomics, may lead to features not observed in the reactions of the smaller molecules, resulting in a need for approximations of a more general nature than those usually applied. Advances in laser and detector technology have made possible state-selected and state-to-state reaction rate measurements (i.e. with preselected reactant and/or known product quantum state distributions) on polyatomics (see [42] and references therein). These provide more detailed information on reaction dynamics than conventional, thermal rate measurements, and thus supplement, and can influence, theoretical treatments.

Such measurements were recently reported [43] for the H + CD_4 deuterium abstraction reaction. This study shows the product distribution of HD states to have a positive correlation between vibrational and rotational energy, contrary to "all known" studies of reactions of atoms with diatomics. Initially termed "anomalous", the same

results were more recently observed [44], to a greater degree of magnitude, in a similar study of the H + C_2H_6 abstraction reaction (1.2) and to a greater degree still in the corresponding reaction with C_3H_8. These results, combined with the present results for the Mu isotopic variants of reactions (1.1) and (1.2), and intrinsic interest in the reactions, should motivate theoretical treatments.

1.2 Organization of the Thesis

This thesis consists of seven chapters including this Introduction, and an Appendix.

The second chapter briefly reviews the standard empirical equations of bimolecular kinetics, with some interpretation of these equations in terms of molecular processes. The third chapter, which reviews electronic structure theory and recent progress in this field, is included for completeness and is optional. The fourth chapter comprises a brief overview of the best-known methods for computation of chemical reaction rates, with discussion of recent progress and in particular, application to the title reactions. All of the popular theories of reaction rates share the need for preliminary computations of electronic state functions; progress in this area has continued since the 1920's [45] but has been rapidly accelerated in recent years through advances in computer technology and algorithm design; current methods are outlined.

In the fifth chapter is outlined the theory of μSR, with mention of some of the various applications of the technique, and the essentials of the setup of a μSR gas chemistry experiment, some of which go beyond experimental considerations. Also discussed briefly are earlier results of Mu kinetics experiments. Included is a discussion of the design, fabrication, and testing of the reaction vessel used in the experiments here reported.

In the sixth chapter is discussed the results of the experiments, with a comparison

to older theoretical and experimental results for isotopic variants of the title reactions. The seventh chapter comprises concluding remarks. The Appendix consists of plots of the experimental data.

Chapter 2

Bimolecular Reaction Kinetics

In this chapter is reviewed the basic equations of bimolecular reaction kinetics needed to interpret the experimental data reported herein[1]. The title reactions fall in the category of elementary bimolecular reactions, "elementary" meaning a "one-step" or "direct" mechanism. The equations describing the bulk kinetics of such a reaction are simple in form and well-known. The general *elementary* bimolecular reaction is of the form

$$\mathrm{A} + \mathrm{B} \rightarrow \mathrm{C} + \mathrm{D} \tag{2.9}$$

and proceeds at the rate defined for a closed system as

$$R \equiv -\frac{d[\mathrm{A}]}{dt} = -\frac{d[\mathrm{B}]}{dt} \tag{2.10}$$

where [A] represents the concentration of A and similarly for B.

The reaction rate R for reaction (2.9) is proportional to the product of the concentrations of A and B:

$$R = k[\mathrm{A}][\mathrm{B}] \tag{2.11}$$

where k is known as the rate constant or, more appropriately, the rate coefficient, since it depends on temperature. Reaction conditions such as pressure can be accounted for by the use of activities, rather than concentrations, of A and B. Equation (2.11) is said to be a second order equation since the powers of the reactant concentrations appearing in

[1]Standard constants used in thesis without explanation: k, Boltzmann constant, h, Planck constant, $\hbar = h/2\pi$, R, gas constant, c, speed of light.

the equation add to two. This equation, though of an empirical nature, has found wide applicability in both gas- and liquid-phase bimolecular reactions and is generally obeyed for elementary reactions. Compound (two or more step) reactions can be analyzed as combinations of elementary reactions obeying equation (2.11). Unimolecular and trimolecular elementary reactions obey similar equations.

Now, and for the remainder of this work, specializing reaction (2.9) to reactions where A is *an atom*, the parameter k can be considered an average of k_i, with i the individual molecular quantum states of B:

$$R_i = k_i[\mathrm{A}][\mathrm{B}_i] \tag{2.12}$$

defining k_i as the rate coefficient between A and B with B in the ith internal state, and the average weighted by the initial distribution of the B states. The *fraction* $[\mathrm{B}_i]/[\mathrm{B}]$, the *weight* of the ith state of B, is denoted w_i, and is the *probability* for B to be in the state i and so is called the distribution function for B. Then, the average k over the k_i takes the form

$$k \equiv \langle k_i \rangle = \sum_{\text{B states}} w_i k_i \tag{2.13}$$

and similarly R represents an average of R_i. These sums conventionally omit the translational energies of A and B, which are treated as separable from internal motion. The k_i are measured by reactant state-selected reaction rate measurements, and are in general a function of temperature. This equation is correct for an ideal gas and displays explicitly that k is not a fundamental quantity but an average over distinct processes. The kinetic isotope effect will in general be different for each such process. As one example, recent [46] reactant state-selected measurements of the reaction

$$\mathrm{O_2^+ + CH_4 \rightarrow H + CH_3O_2^+} \tag{2.14}$$

at ~500 K give a rate coefficient ~17 times higher for vibrationally excited CH_4 than for the ground state.

The *reaction cross-section* σ between A and B in state i can be defined using

$$k_i(T) = \int d\mathbf{v}\, w(T, \mathbf{v})\sigma_i(\mathbf{v}) \tag{2.15}$$

where μ is the reduced mass of A and B_i, $\mathbf{v}$ is the relative velocity (prior to "collision"), which is assumed is separable from the other types of motion, and w is the distribution of $\mathbf{v}$, a continuous function if translational motion is treated classically. The reaction cross-section can also be defined in terms of *reaction probability* for a given molecular "collision", which itself can be defined as an A-B encounter close enough to have an appreciably high probability of reaction, say, some arbitrary threshold. The integral serves to sum σ jointly with the *frequency of collision*, resulting from relative translational motion of A and B_i. For the reactant molecules far enough apart that they do not affect each others' collision processes appreciably, i.e. a gas, σ can be classically interpreted as a cross-sectional area, per reactant molecule, which needs to be collided with in order for reaction to occur.

For an ideal gas at equilibrium, the internal states of B will be individually weighted by the Boltzmann distribution (see any statistical mechanics text), that is,

$$w_i = \frac{[B_i]}{[B]} = \frac{g_i e^{(\epsilon_i - \epsilon_0)/kT}}{q_B} \tag{2.16}$$

where ϵ_i is the energy of the ith state of B, g_i its degeneracy, ϵ_0 the energy of the ground state, T the temperature of the system, and q_B the molecular partition function of B. The partition function is computed by taking the sum of equation (2.16) over all states and noting $\sum[B_i]/[B] = 1$. The translational energy of A or B obeys the same equation given our assumptions but the energy in this case is continuous.

Using the distribution of equation (2.16) for translational energies of A and B. and applying the result to equation (2.15), the resulting equation can be written as

$$k_i = \left(\frac{8kT}{\pi\mu}\right)^{1/2} \int_0^\infty d\left(\frac{E}{kT}\right)\left(\frac{E}{kT}\right)\sigma_i(E)e^{-E/kT} \tag{2.17}$$

with μ the reduced mass of A and B_i and E their relative translational energy. The equation is in such a form as to explicitly display the dimensions, velocity times area, of k_i. This equation strongly displays the "trivial" kinetic isotope effect due to reactant mass; the factor multiplying the integral is inversely proportional to $\sqrt{\mu}$.

Another well-known empirical reaction rate equation is the Arrhenius equation

$$k = Ae^{-E_a/\mathrm{R}T} \tag{2.18}$$

where k is as defined in equation (2.11) and T is the absolute temperature. The parameter E_a is called the activation energy, and A, a constant, is the pre-exponential factor. The equation is frequently generalized to allow A to be a function of T. When fitted to experimentally measured thermal reaction rates, it holds very well for many reactions. For bimolecular reactions for which equation (2.18) holds, E_a is of the same order of magnitude (see Chapter 4) as the reaction's energy barrier per mole of reactant, as suggested by its resemblance to the Boltzmann distribution of reactants in equation (2.16). Taking the natural logarithm of each side gives

$$\ln k = \ln A - \frac{E_a}{\mathrm{R}T} \tag{2.19}$$

which, when plotted as $\ln k$ *vs.* $1/T$, fits well to a straight line for many reactions, corresponding to constant A.

The equation (2.18) is reproduced by use of simple models for the reactants. For example, suppose A and B are assumed to be hard spheres, ignoring any internal structure, and all collisions with relative kinetic energy of below a threshold energy E_0 do not result in reaction, while above E_0,

$$\sigma(E) = \sigma_0 \left(1 - \frac{E_0}{E}\right) \tag{2.20}$$

with σ_0 and E_0 constants. This cross-section expression [47] is intended to include the effect of the relative angular momentum of the reactants, and is commonly referred to

as the "line of centers" model. Using the equation (2.17), the equation

$$k = \sigma_0(8\mathrm{k}T/\pi\mu)^{1/2}e^{-E_0/\mathrm{k}T} \tag{2.21}$$

results [47], clearly a form of equation (2.18).

The activation energy E_a can be interpreted [48] as the difference between the average energy (above ground state) of those reactant atoms A and molecules B that actually react, commonly denoted $\langle E^* \rangle$, and the average for all A and B, $\langle E \rangle$.

$$E_a = \langle E^* \rangle - \langle E \rangle \tag{2.22}$$

For relatively small molecules such as CH_4, $\langle E \rangle$ is within an order of magnitude of $\mathrm{k}T$; with a large enough reaction energy barrier it can be ignored compared to $\langle E^* \rangle$. If $\langle E^* \rangle$ is also only weakly temperature dependent, A is observed to be a constant. The observed A will in general have a temperature dependence where $\langle E \rangle$ is not negligible compared to $\langle E^* \rangle$, or where $\langle E^* \rangle$ is reasonably temperature dependent, most notably in the case of a high degree of quantum tunneling. Where this is the case, equation (2.18) is often used with A of the form of a constant times some power of T, inspired mainly by the $T^{1/2}$ dependence exhibited by the simple model with cross-section given by equation (2.21). Experimental data fitted to equation (2.18) with increased upward curvature at low T is often taken as an indication of reaction facilitated by quantum tunneling since that corresponds to reaction with reactants of energy less than the barrier height; the extra curvature results since the presence of tunneling is obscured at higher temperatures by "normal" (classical) reaction paths.

The equations (2.11), (2.12), and (2.16) are rigorously correct for an ideal gas in equilibrium; see any introductory text on reaction dynamics. For the experiments reported in this thesis, measurements were performed on CH_4, C_2H_6, and N_2, whose compressibility curves, found in many physical chemistry texts, show ideal gas behaviour to a very good approximation up to the gas pressures used. A few sample

calculations with functions fitted to these curves show negligible deviation from ideal behaviour for these gases compared to experimental error.

Equation (2.11) therefore forms the starting point for the interpretation of the data from the μSR measurements. It does require a slight modification for this study. For the reactions (1.3) and (1.4):

$$\mathrm{Mu} + \mathrm{HR} \rightarrow \mathrm{MuH} + \mathrm{R} \tag{2.23}$$

equation (2.11) takes the form

$$R = k[\mathrm{Mu}][\mathrm{HR}] \tag{2.24}$$

without any modifications. Now, the nature of the time-differential μSR technique, in which muons enter the reaction vessel one at a time, dictates that the concentration of Mu cannot be defined in the normal manner; this is dealt with in Chapter 5. More consequentially, the number of muons entering the reaction vessel in the course of an experimental run dictate the maximum number of Mu atoms created in the run. The number of muons per run is negligible compared to the number of reactant molecules in a very small volume, therefore [HR] $\gg$ [Mu]. The result is that [HR] can be treated as a constant in equation (2.24) to a very good approximation. It can therefore be absorbed into the constant k giving the pseudo-first order equation

$$R = k'[\mathrm{Mu}] \tag{2.25}$$

where $k' = k[\mathrm{HR}]$. Recalling the definition of R in equation (2.10) and solving for [Mu] by integration,

$$[\mathrm{Mu}] = [\mathrm{Mu}]_0 e^{-k't} \tag{2.26}$$

where $[\mathrm{Mu}]_0$ is the "concentration" of Mu at time zero. Note that, since H atoms are very reactive and so tend to exist in very low concentrations, the same approximation applies to kinetics studies done on the H, D, and T variants of the reaction (2.24).

The parameters k' for the title reactions at various reaction temperatures are gotten from plots of the μSR data, obtained in the experiments here reported. As detailed in Chapter 6, k' for each of the title reactions (there referred to as "k"), plotted as a function of T, give very good fits to equation (2.18) with A constant.

Chapter 3

Electronic Structure

3.1 Introduction

The recent progress of the best-known chemical reaction rate theories provides the major motivation for this thesis work. These theories depend on lower-level theories of molecular structure, which are reviewed in this chapter. This chapter thus serves as essentially optional background for the next, and is included for completeness since progress in both has been highly correlated. Comprehensive reviews of virtually every topic discussed in this chapter and the next will be found in the recently published NATO Advanced Studies Institute workshop proceedings, "Methods in Computational Molecular Physics," reference [1].

For the problem of calculation of chemical reaction rates from theory it is possible to define three main approaches. The rigorous statistical approach computes the rate of reaction as a relaxation of the reacting system towards equilibrium, using the theorems of non-equilibrium statistical mechanics. Other approaches consider the detailed interactions of reacting species, using the concept of the potential energy surface. These include transition state theory and generalizations of collision theory. For gas-phase rates, these have been more popular in the recent literature, and have undergone rapid theoretical development. As well, transition state and collision theory results are often more easily understood by experimental chemists. Only the latter two approaches will be considered here.

The statistical approach may be more useful for condensed phase systems, in which the interactions of molecules are more complicated than for gas-phase systems. It is to be hoped, however, that progress in gas-phase reaction rate theory can provide greater understanding of the dynamics of condensed phase reactions, which are perhaps of more practical interest than gas-phase reactions. The relationship between gas-phase and solution reaction dynamics is not well established but is under study [49–52].

Following Johnson [48] a hierarchy for the computation of reaction rates can be established for theories which consider molecular level interactions:

1. Calculate a potential energy surface for the reacting system.
   (a) Calculate the "potential energy" for a series of nuclear positions.
   (b) Join the points thus calculated by a function representing the molecular interactions. The result is a multidimensional function of potential energy, a *potential energy surface* (PES).
2. Calculate the reaction probability on the PES for all initial conditions likely to contribute to the rate. These are the initial internal states of the reacting species.
3. Average over an appropriate set of initial conditions. This is generally done using the Boltzmann distribution given by equation (2.16).

Reaction rate theories, also applicable to atomic processes such as elastic scattering, are more difficult to apply for chemical reactions because chemical reactions simply represent more complicated processes. Particularly for chemical reactions of molecules of non-trivial size, each of the steps of the hierarchy is itself a rather complex problem. Consequently, approximations appear at each step. The interpretation of theoretical rate data is then complicated by the need to consider the approximations made at each level. The various approximations used to construct PES's are briefly reviewed in this

chapter; those resulting from the assumptions of reaction rate theories using PES's are reviewed in the next.

3.2 Potential Energy Surfaces in Reaction Rate Theory

For TST and collision theory, it is conventional to first construct a so-called *potential energy surface.* A potential energy surface (PES) is actually a multidimensional plot of the total electronic (potential and kinetic) energy plus the electrostatic energy due to the nuclei, as a function of the positions of the nuclei in all reacting molecules. Such a construction necessarily assumes the validity of the famous Born-Oppenheimer approximation which holds that the electronic motion is separable from the motion of the nuclei. Thus nuclear motion is assumed electronically *adiabatic*; reactions are assumed to proceed without change in overall electronic state. Because of the approximation, the surface is invariant to isotopic substitution, which allows isotopic variants of chemical reactions to be easily compared.

The validity of the approximation is dependent on the fact that the electrons are much lighter than the nuclei and so adjust their motion essentially instantaneously to that of the nuclei. The approximation has been found to hold very well for reactions involving molecules in their ground electronic states. In fact the calculations of Schatz [36] for the rate of reaction (1.8), a chemical reaction for which the effects of breakdown of this approximation would be expected to be among the most serious, show virtually exact agreement with accurately measured experimental results [37]. Within this approximation the potential energy surface is an effective force field for nuclear motion.

The majority of chemists are familiar with the concept of a potential energy surface. For the reaction of an atom and a diatomic molecule such a surface allows for easy

visualization of the molecular interactions. This surface is a function of three relative nuclear positions. Most commonly, such a potential energy surface is represented as a series of sheets, each with the same two nuclear positions as independent variables, the other being replaced by an angle variable θ. The dependent variable, energy, is then plotted as a series of contour lines on each sheet. Figure 3.1 shows one sheet for the general atom-diatom reaction

$$\mathrm{AB} + \mathrm{C} \rightarrow \mathrm{A} + \mathrm{BC}. \tag{3.27}$$

The part of the surface at the upper left, where A and B are close to each other and far from C, represents the reactants in the reaction. Similarly the part at the lower right represents the products. (The opposite convention is also used.) This

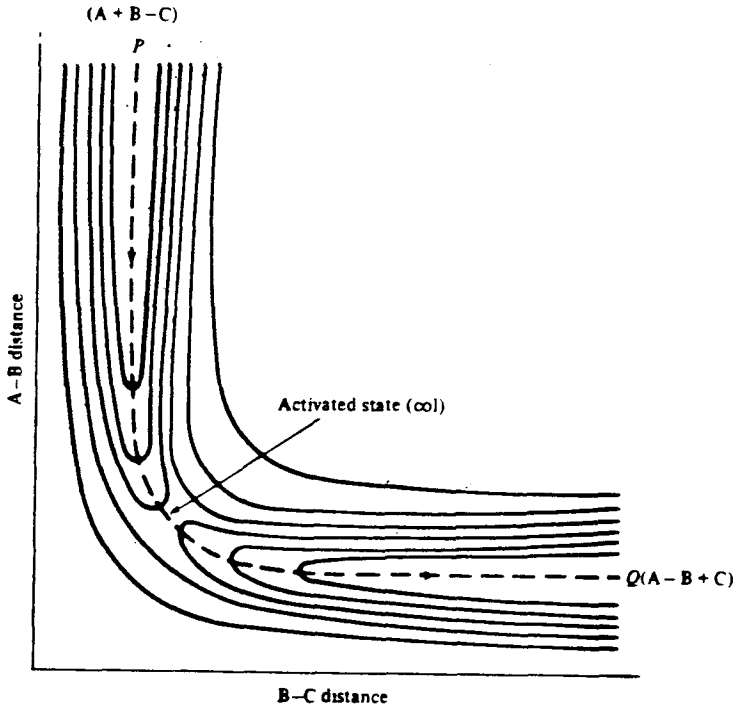

Figure 3.1: Potential energy surface for reaction (3.27) for a given angle $\angle$ABC; taken from [53].

easy visualization possible for an atom-diatom reaction is lost for more complicated reactions, though insight can be gained by examining selected projections (i.e. cross-sections) of the surface.

3.3 Molecular Electronic Structure

The problem of computing the electronic energy for a given point on the potential energy surface that is, a given set of relative nuclear positions, is itself a major computational problem. Probably, it has represented the greatest bottleneck in the computation of accurate reaction rates. The theory of electronic structure has undergone rapid development since the invention in the 1960's of the integrated circuit chip. Rapid improvements in computer power and speed have greatly increased the feasibility of truly accurate electronic structure calculations. Theoretical advances have also been made, most notably algorithmic developments designed to optimize the use of computer resources.

The standard form of the complete nonrelativistic electronic Hamiltonian for a molecule or complex, with nuclear motion separated but including the electrostatic energy due to the nuclei, is

$$\hat{H}_{el} = -\frac{1}{2}\sum_i \nabla_i^2 - \sum_{\alpha,i} \frac{Z_\alpha}{r_{\alpha i}} + \sum_{ij,i\neq j} \frac{1}{r_{ij}} + \sum_{\alpha\beta,\alpha\neq\beta} \frac{Z_\alpha Z_\beta}{r_{\alpha\beta}} \tag{3.28}$$

in atomic units: $\hbar = 1$, $m_e = 1$, $e = 1$. The distance r_{ab} is that between particles a and b. The Roman indices refer to the electrons, the Greek indices to the nuclei. The energies of the possible states are the constant eigenvalues E satisfying the equation

$$\hat{H}_{el}\psi = E\psi \tag{3.29}$$

together with appropriate boundary conditions. The "potential energy" mapped by a PES is, at a given point, the lowest eigenvalue of this Hamiltonian.

Equation (3.29) is the starting point of electronic structure theory. Note that, within the Born-Oppenheimer approximation, the last term of equation (3.28) has only the effect of shifting the total energy by a constant, and so need not be considered in the calculation, and can be simply added at the end. For systems of more than one electron more levels of approximation are necessary to actually compute an electronic state function, since equation (3.29) can not be solved in general without them. This equation is a special case of the many-body problem of physics, whose many applications include elementary particle interactions and the propagation of vibrations in solid matter.

Conventionally, an electronic structure calculation is begun by separating the motions of the individual electrons, giving a set of n one-electron Hamiltonians for an n-electron system. The one-electron state functions then must be combined to form the total electronic state function ψ in such a way as to take account of the facts that electrons are indistinguishable and obey the Pauli exclusion principle. The total electronic state function for an atom or molecule can be most simply represented as a linear combination of Slater determinants of the form

$$\psi = |\phi_1(1)\,\phi_2(2)\cdots\phi_{n-1}(n-1)\,\phi_n(n)| \tag{3.30}$$

where the ϕ's are the one-electron state functions of the n total electrons and all the rows of the determinant are formed from the one shown by permuting the electron indices (parenthesized) in all possible combinations. The ϕ_i are products of spatial functions with the two possible electron spin functions. The existence of electron spin gives 2^n possible Slater determinants for an n-electron configuration (e.g. a $1s1p$ atomic configuration). A linear combination of Slater determinants having the proper electron exchange symmetry is called a *configuration state function* (CSF).

Basic to the theory of electronic state functions formed from CSF's is the *variation theorem*, which holds [45] that the true ground state energy for any quantum system

with a time-independent Hamiltonian lies below that of any calculated approximate state function ψ_{approx}, whose energy is computed as the expectation value:

$$\langle E_{\text{approx}} \rangle = \frac{\langle \psi_{\text{approx}} | \hat{H} | \psi_{\text{approx}} \rangle}{\langle \psi_{\text{approx}} | \psi_{\text{approx}} \rangle} \tag{3.31}$$

which is self-evident when it is realized that any approximate state function obeying the correct boundary conditions of the physical system is a linear combination of the ground state plus states of higher E. This theorem leads to an approximate method for calculation of ground state functions: try a function with parameters which can be varied, and minimize the function with respect to the expectation value $\langle E_{\text{approx}} \rangle$. With the Born-Oppenheimer approximation, the theorem applies to equation (3.29). This provides a guide to creating algorithms for the calculation of electronic structure: systematically minimize $\langle E_{\text{approx}} \rangle$.

When calculating equilibrium properties of molecules, the same theorem states that the equilibrium nuclear positions are those which give the lowest "potential energy" for nuclear motion, as defined above. To find this set of relative nuclear positions it is necessary to follow an optimization procedure which systematically varies the set positions and does a series of electronic structure calculations, one at each set. Each such calculation constitutes a point on a PES for the molecule. This PES can be used to calculate the rovibrational state function(s) for the molecule by solving or estimating the solutions of the nuclear motion Hamiltonian—the part of the Hamiltonian of the molecule omitted from $\hat{H}_{el}$. The rovibrational state functions must be found for the use of transition state theory, and are also of interest because they determine the spectroscopic constants for a molecule. Note that the rovibrational motion is *not* isotopically invariant, which is of great importance to comparison of reaction dynamics. The theory of nuclear motion in molecules has lead to development of general computational methods [54,55], including an adaptation of the SCF method [56] for electrons,

described in the this section. Alternatively, or in combination, the use of analytic properties of the electronic state function such as that expressed by the Hellmann-Feynman theorem (see articles in reference [57]), can lead to these solutions. For electronic state functions from the various theories incorporating CSF's, this theory is particularly well developed [58,59], but is not a "solved problem."

3.3.1 SCF State Functions

There are many ways to form the ϕ_i of the CSF depending on the accuracy desired for the calculation. If the CSF is to be used without modifications, it has been shown (references listed in [45]) that the best possible state function, in the sense of having the most accurate calculated energy, is given by the Hartree-Fock self-consistent field (SCF) theory. In this theory, the contribution to the one-electron Hamiltonian for an individual electron due to the other electrons is replaced by a continuous charge distribution. The continuous charge distribution due to electron j is just the probability density function, that is, $\rho_j = \phi_j^2$. This represents an average as opposed to instantaneous interaction, and has the effect of raising the energy of the calculated electronic state function as compared to the true value, because *electron collisions*, which allow electronic energy transfer, are neglected. This "mean-field" approximation leads to a Hamiltonian separable in the individual electron motions.

Replacing the third term of the Hamiltonian in equation (3.28) with the contributions due to the continuous charge distributions and substituting into equation (3.29), a series of n one-electron eigenvalue problems

$$\hat{F}_i \phi_i = \epsilon_i \phi_i \tag{3.32}$$

is obtained, where

$$\hat{F}_i\phi_i = \left(-\frac{1}{2}\nabla_i + \sum_\alpha \frac{Z_\alpha}{r_{i\alpha}} + \sum_{j\neq i}[\hat{J}_j - \hat{K}_j]\right)\phi_i \tag{3.33}$$

with the Coulomb ($\hat{J}_j$) and exchange ($\hat{K}_j$) operators defined as

$$\hat{J}_j\phi_i = \phi_i \int d\tau \, \frac{|\phi_j|^2}{r_{ij}} \tag{3.34}$$

and

$$\hat{K}_j\phi_i = \phi_i \int d\tau \, \frac{\phi_j^*\phi_i}{r_{ij}} \tag{3.35}$$

with integration $\int d\tau$ over all space including the spin part of the ϕ_j. The Fock operator $\hat{F}_i$ represents an effective one-electron Hamiltonian. It is dependent on its own eigenfunctions and so must be calculated by a series of successive approximations, which are done in such a way as to minimize the total energy, following the variational principle. The ϕ_i are usually constrained to be orthogonal to each other. The resulting total energy is

$$E = \sum_i \epsilon_i - \sum_{ij,j\neq i}(J_{ij} - K_{ij}) \tag{3.36}$$

where the Coulomb integral J_{ij} is related to the corresponding operator $\hat{J}_j$ by

$$J_{ij} = \int d\tau \, \hat{J}_j\phi_i^* \tag{3.37}$$

and similarly for the exchange integral K_{ij}.

The one-electron state functions furnished by SCF theory are easily interpretable in terms of electron interactions, and the theory gives an intuitively pleasing view of the total electronic state function. The spatial part of the one-electron state functions obtained are the orbitals of atomic (AO) and molecular orbital (MO) theory. Together with the spin-dependent parts, they are called spin-orbitals.

The orbitals are frequently used in qualitative arguments to rationalize molecular structure by synthetic chemists. The CSF obtained generally includes [60] ~99% of the

total energy. However, as has been frequently noted (e.g. [45]), the error in the energy introduced by the neglect of instantaneous electron interactions is comparable to the energy change in chemical reactions.

The difference between the energy of the SCF state function and the exact nonrelativistic energy is called the *correlation energy* after the term *electron correlation* for the neglected instantaneous interactions. Therefore it is necessary to go beyond the SCF procedure to obtain an accurate potential energy surface. This is to be intuitively expected since the electron interactions change drastically in the course of a chemical reaction.

For molecules, the spin-orbitals are almost universally built up as *linear combinations* of atomic orbitals centered on the various atoms in the molecule; this approach, abbreviated LCAO, provides molecular one-electron state functions with a very clear physical interpretation in terms of the orbitals of the constituent atoms. As well this approach is relatively easy to implement as a computer algorithm. First proposed by Roothan in 1951 [45], this theory treats the atomic orbitals as basis functions of a vector space. The molecular orbitals are then formed as projections onto this basis satisfying the one-electron eigenvalue problems of equation (3.32). The only disadvantage, greatly outweighed by the ease of computation, is that some accuracy is lost, because the basis set is incomplete. This can be alleviated by judicious choice of a basis set.

Since the set of atom-centered functions used, called the basis set, is finite, therefore incomplete, any functions which uniformly converge to zero at infinity, whether centered on an atom or not, are legitimate basis functions, so it is advantageous to use the computationally most expedient functions. The functions actually used for the atomic orbitals are linear combinations of three-dimensional Gaussian functions ($\propto e^{-cr_{i\alpha}^2}$, with c a positive constant) fitted by a least-squares procedure to *Slater-type orbitals* (STO's), which resemble the actual atomic orbitals. The resulting computation is comparably

easy because "the product of two Gaussians is a Gaussian". Some calculations add functions not centered on atoms, but then the simple LCAO interpretation is lost.

When the molecular orbitals are expanded in the basis functions χ_s

$$\phi_i = \sum_s c_{is}\chi_s \tag{3.38}$$

there results, inserting ϕ_i into equation (3.32), the Roothan equation

$$\sum_s c_{is}\hat{F}_i\chi_s = \epsilon_i \sum_s c_{is}\chi_s \tag{3.39}$$

or, premultiplying by χ_r and taking expectation values, the matrix form

$$\mathbf{FC} = \epsilon\mathbf{SC}. \tag{3.40}$$

Without affecting the total energy computed [45] the χ_s can be redefined to be orthogonal to each other resulting in

$$\mathbf{F'C'} = \epsilon\mathbf{C'} \tag{3.41}$$

the standard eigenvalue equation. The algorithm to find the ϵ_i is well established and even hardware-encoded in some computers.

A basis set of as many AO's (with spin) as there are electrons is a *minimal* basis set. For especially large molecules, it may be desirable to constrain the lower energy (core) orbitals to be unperturbed from the initial AO's; this is the *valence electron* approximation. In the other direction, when a larger-than-minimal basis set is used, a number of orbitals beyond the "occupied" orbitals used in the CSF are obtained, called *virtual* orbitals. These are omitted from the potential energy terms of the Fock operator but are generally still calculated. Roughly speaking, the virtual orbitals represent one-electron "excited states"; the CSF with one or more ϕ_i replaced by virtual orbitals then represents an excited electronic state of the molecule. This concept is the starting point of the *configuration interaction* (CI) theory of electron correlation.

3.3.2 Post-Hartree-Fock Procedures

Although Hartree-Fock CSF state functions are often useful in rationalizing molecular structure and other static concepts, they are, as noted above, not generally of sufficient accuracy for a potential energy surface of use in predicting chemical reaction rates. For example, for the reaction (1.1), calculation [61] with a DZ-SCF basis set predicted a barrier height of ~34 kcal/mol compared to the experimental value [26] of ~12 kcal/mol. This theoretical result was improved by post-Hartree-Fock theory (CI) to ~17 kcal/mol.

The three best-known procedures which start with a CSF state function and systematically convert it to an improved state function including electron correlation are briefly discussed here:

1. Configuration Interaction or Mixing (CI or CM)
2. Multi-Configuration SCF (MCSCF)
3. Various perturbational approaches, in particular the Møller-Plesset (MP) Perturbation Theory

Combinations of these are possible, especially the first two [62].

Much of the recent theoretical work in electronic structure (see [57]) has focused on the use of the mathematical properties of CSF's to obtain unambiguous algorithms to obtain such properties as multipole moments and energy derivatives analytically. The energy derivatives are particularly useful in obtaining a potential energy surface with accurate local curvature between fitted points. The multipole moments are required for the accurate calculation of rovibrational molecular states. Analytic energy derivatives are now available in standard computational software for CI, MCSCF, and MP theory.

The CI theory is based on the idea of forming new CSF's by "promotion" of one or more electrons of the Hartree-Fock CSF from filled orbitals to virtual orbitals, called

excitation. It has been shown that with a complete basis set, all possible CSF's form a complete vector space, whose properties can be used to algorithmic advantage. The true state function ψ is a linear combination of the possible CSF's Φ_l

$$\psi = \sum_l C_l \Phi_l. \tag{3.42}$$

including the Hartree-Fock calculated CSF and the C_l are found by substituting into equation (3.28) and solving the resulting equations to minimize the total energy. The expansion is (in the nonrelativistic theory) exact for a complete basis set.

To get reasonably accurate results, the initial basis set must be of reasonable size since this dictates the number of Φ_i available. Generally, for molecules the size of CH_4 or C_2H_6, only excitations of the highest energy (valence) orbitals are included in the Φ_l; this is called the *frozen core* approximation. The effect of the expansion on the Hartree-Fock CSF, as succinctly explained in reference [63], is to place the "excited" electrons into a linear combination of so-called *polarized orbital pairs* which allows the electrons to "'avoid'" each other.

In principle, in the CSF basis, the possible vectors $\mathbf{C}$ $(= \{C_l\})$ are eigenvectors of $\hat{H}$. Since the forming of the matrix elements $\langle\Phi|\hat{H}|\Phi\rangle$ is a time and computer memory-consuming process, a method has been developed, called *direct* CI, allowing the computation of the lowest energy eigenvector $\mathbf{C}$ without forming the full Hamiltonian. A detailed analysis is to be found in reference [64]. Generally, only a small subset of the possible CSF's are included in the expansion. Much work has been done in determining which excitations can be omitted with the least damage to the calculation's accuracy. Another advance has been development of alternate schemes to Hartree-Fock to get the initial CSF, since there is no reason why the SCF orbitals will necessarily be the computationally most expedient in the CI calculation. Similar techniques are possible for other theories of electron correlation.

The MCSCF theory, often used in combination with CI, is an expansion of the true state function in a series of CSF's

$$\psi = \sum_l D_l \Phi_l \tag{3.43}$$

but in this case the CSF's Φ_l are formed using different orbitals from each other, that is, each CSF is separately optimized. So the resulting approximate state function is a combination of several electron configurations. As with CI, the state function is determined by iterations to minimize the total energy. In this case the chief challenges are in selecting the configurations making the greatest contribution to the true state function and in constraining the Φ_l so that they do not collapse into one another; see reference [65]. As with CI, algorithms have been developed to obtain MCSCF state functions more easily (see, for example, [66]). MCSCF combined with CI is called *multi-reference* CI (MRCI).

As described in reference [63], with variational theories such as CI and MCSCF, when an incomplete basis set is used, there is a problem of *size inconsistency*, meaning that the average error for a given level of approximation will not produce the same fractional total energy error for different molecules. This is a problem if a potential energy surface describing a chemical reaction is to be constructed, since the parts of the surface with the reactants near each other (the "transition state") will have a different correlation energy error than the reactants, leading to extra error in the calculated reaction rates.

This problem does not occur for perturbational approaches such as the MP theory. MP theory treats the sum of the Fock operators $\sum_i \hat{F}_i$ as a reference Hamiltonian and $\hat{H}_{el} - \sum_i \hat{F}_i$ as a perturbation on the reference Hamiltonian's eigenfunctions, leading by standard methods (Rayleigh-Schrödinger perturbation theory [63]) to an infinite series of CSF's with, generally, diminishing contributions to the true state function as the

series is continued. Also a series in energy terms is obtained. The CSF series evaluated up to nth order furnishes terms in the energy correction series up to order $2n+1$. The series are truncated after an arbitrary number of terms but within this approximation the CSF's included in the expansion are non-arbitrary, as opposed to usual application of CI, in which informed guesses provide the list of CSF's to use. MP also gives a guide to which CSF's are most important in the expansion. For example, the second order correction to the single-CSF state function given by MP theory consists of double excitations only. MP, up to fourth-order corrections in the energy, is the correlation theory routinely used for molecules the size of CH_4 (see [39,67,68]).

Recently, "benchmark" full CI calculations, in which every possible CSF arising from a "moderate-sized" basis set, have set a standard for electron correlation calculations. The full CI calculations, on H_2O, CH_2, N_2 and F^-, are critiqued in reference [60] in comparison with currently more widely applied MP calculations. It was found that perturbational calculations, even through fourth order, failed to give an adequate description of bond stretching in H_2O, in which the error in the energy increased by an order of magnitude on doubling the O–H bond length from equilibrium. The error is attributed to the use of a single reference function; the authors conclude that accurate descriptions of dynamical processes will require the use of several configurations as the starting point for electron correlation. Such calculations have not yet been performed on CH_4 to the knowledge of the present author.

3.3.3 Other Approaches to Electronic State Functions

Ab initio molecular orbital theory coupled with the use of electron correlation theories such as those described previously has been the subject of the majority of recent theoretical developments in electronic structure theory, but other approaches have received some attention.

Semi-empirical state functions are normally calculated using the SCF-MO theory with the valence-electron approximation, but with some integrals J_{ij} and K_{ij} neglected and some others obtained by fitting state functions to experimental data. The famous Hückel π MO theory is the ultimate "semi-empirical" theory, using a total of two parameters to describe the state functions of every π-conjugated hydrocarbon system. Despite its deep approximations it is still used today in descriptions of electron structure, often with useful qualitative accuracy. On the more accurate side, MNDO (*modified neglect of differential overlap*) and its successors such as AM1 and PM3, fit the integrals not neglected in such a way as to reproduce experimental heats of combustion. These theories are most useful for systems similar to the systems used to obtain the parameters, but for systems the size of CH_4 they have been superseded by *ab initio* methods. Semi-empirical theory can be applied to much larger molecules than is possible with *ab initio* calculations. Also, it can be expected that for many systems semi-empirical calculations may perform better than *ab initio* calculations neglecting electron correlation since the parameterized J_{ij} and K_{ij} include electron correlation. Semi-empirical theories not using SCF have also been devised.

In the *valence bond* VB theory, the approximate function consists not of MO's but of linear combinations of atomic orbital product states. For example, a diatomic molecule AB has its first-order VB state function given by

$$\psi_{\mathrm{VB}} = \frac{1}{2(1+S_{\mathrm{AB}}^2)^{1/2}}[1s_{\mathrm{A}}(1)1s_{\mathrm{B}}(2) + 1s_{\mathrm{A}}(2)1s_{\mathrm{B}}(1)]\,[\alpha(1)\beta(2) - \alpha(2)\beta(1)] \qquad (3.44)$$

where the electron numbers are parenthesized, and S_{AB} is the overlap integral $\langle 1s_{\mathrm{A}}|1s_{\mathrm{B}}\rangle$. This approximate state function is a linear combination of two Slater determinants of atomic orbitals $1s_{\mathrm{A}}(1)\alpha(1)\,1s_{\mathrm{B}}(2)\beta(2)$ and $1s_{\mathrm{A}}(1)\beta(1)\,1s_{\mathrm{B}}(2)\alpha(2)$. This type of state function is designed to describe the bonding in terms of electron exchange between the atomic orbitals of individual atoms. Each "exchange" which is allowed gives rise to

two Slater determinants of AO's. The linear combination is needed to account for the exchange symmetry of electrons.

In the *generalized* VB theory, the atomic orbitals are replaced by variational functions and the total energy minimized. It is actually a form of MCSCF [63]. For a polyatomic molecule such as CH_4 the atomic orbitals would be replaced by "hybrid" orbitals, linear combinations of atomic orbitals on a single atom combined in such a way as to conform to the geometry of the molecule. The hybridization allows the electrons to "avoid" one another and so the GVB theory has electron correlation built in. Because the AO's on different atoms cannot be be constrained to be orthogonal to each other, GVB state functions are generally more difficult to obtain than MO CSF's.

Another well-known theory of electronic structure is density-functional theory in various forms, which are based on the fact that there is a unique functional relationship between the electron density ρ and the state function ψ [45]. The problem of density-functional theory is to find the electron density and also the form of the relationship between ρ and the energy. The state function need not be calculated.

For the theories and methods described in this section, casual examination of the literature will reveal a huge number of acronyms and abbreviations used without explanation; in a modern quantum chemistry text such as I.N. Levine's "Quantum Chemistry", 4th. ed. [45] will be found the majority of those in common use. An accessible review of recent progress is reference [69], and reference [63] gives an overview of physical interpretation of the theory.

3.4 Constructing Potential Energy Surfaces

Once the "potential energy" has been calculated for a reasonably large series of points, a potential energy surface can be constructed. The electron motion has been "integrated

out" so the potential energy surface is a function of the relative nuclear positions. If the Born-Oppenheimer approximation was not invoked, the topographical features of the potential energy function for the nuclei would be dictated mainly by the analytical properties of the electron interactions. For the practical problem of constructing a potential energy surface it is necessary to represent these *electron* interactions implicitly by an essentially arbitrary function of the nuclear coordinates. The function is fitted to the points, normally using a standard least-squares procedure, which minimizes the average estimated error.

The function used is dictated mainly by the intended use of the surface, since presently available potential energy surface calculations are of insufficient quality to avoid major trade-offs between accuracy in computing various quantities of interest. This arises partly due to the fact that only a limited number of points can be initially calculated due to limited computer resources. For example, the very accurate LSTH surface for $H + H_2$ reaction has $\sim$300 points calculated. Also problematic are the potentially rapid changes in energy at short distances, and the aforementioned "size inconsistency".

For the best available potential energy surface for the $H + CH_4$ abstraction reaction, published by Joseph *et al.* in 1987 [70], gives an excellent example of the trade-offs involved in the construction of a semi-empirical PES. For this surface, no attempt is made to reproduce the the experimental rates for the substitution reaction (1.5). Used with the transition state theory of reaction rates, it is in good agreement with experiment for the abstraction reaction (1.1), over a reasonable temperature range. Rate coefficients calculated with this surface, discussed later, are in very good agreement with experiment. In contrast, both reactions are intended to be modelled by the surface of Raff [71] *et al.*, which reproduces the CH_4 and CH_3 experimental harmonic frequencies quite well. However, it leads to transition state theory computed rate coefficients in

very poor agreement with experiment.

The trade-offs are resolved by the choice of empirical parameters used to fit the surface; modern potential energy surfaces must be fitted using some empirical parameters and are therefore semi-empirical in nature even if the points are computed using *ab initio* theory. An example is the H + CH_4 surface [26, 72, 73] of Walch *et al.* For this surface the experimental values of the reaction endoergicity of reaction (1.1) and vibrational frequencies of CH_4 were initially used, with the barrier height adjusted to reproduce experimental rate coefficients after other treatment of the data.

It is notable that the first calculated potential energy surface of "chemical accuracy" ($<\sim$1 kcal/mol) was computed as early as 1973 [74]. An analytical function later fitted to this surface is the LSTH (Liu-Siegbahn-Truhlar-Horowitz) surface mentioned earlier. It is fully *ab initio* yet more accurate than any surface ever calculated for a larger system, because the computational effort for constructing a PES increases very quickly with the number of electrons. This surface was used in Schatz' accurate calculations [36] for the Mu + H_2 reaction (1.8), and remains a benchmark for the quality of new PES's. Only on this surface can the accuracy of rate calculations be reliably attributed to the rate theory used. The surface has undergone further development to the even more accurate DMBE (double many-body expansion) surface [74].

A variety of functions and combinations thereof are in common use for the calculation of potential energy surfaces. A few well-known ones, described in Johnston's 1965 book [48] "Gas Phase Reaction Rate Theory", are still in routine use. The famous Lennard-Jones 6-12 potential

$$V(R) = 4\epsilon \left[\left(\frac{\sigma}{R}\right)^{12} - \left(\frac{\sigma}{R}\right)^{6} \right] \tag{3.45}$$

with σ obtained from experimental data or *ab initio* calculations, is found to reproduce well the interactions between two atoms at distance R in many cases. Also well known

is the Morse function

$$V(R) = D_e(e^{-2\beta r} - 2e^{-\beta r}) \tag{3.46}$$

where D_e is the dissociation energy from the energy minimum to infinity, β a parameter, and r is $R-R_e$ with R_e the equilibrium (minimum energy) distance. Where this function accurately represents the potential between two atoms in an overall *singlet* electronic state (total electron spin zero), the Sato-Morse potential

$$V(R) = D_e(e^{-2\beta r} + 2e^{-\beta r}) \tag{3.47}$$

may accurately represent the potential for the case of a triplet (total electron spin one). The LEPS potential energy theory uses for singlets and triplets respectively the energy expressions

$$E_S = \frac{Q + \alpha}{1 + \Delta} \tag{3.48}$$

$$E_T = \frac{Q - \alpha}{1 - \Delta} \tag{3.49}$$

which are identical to the energy expressions obtained for VB state functions of diatomic molecules from equation (3.44), where Q corresponds to the Coulomb integral

$$J_{\mathrm{AB}} = \left\langle 1s_{\mathrm{A}}(1)1s_{\mathrm{B}}(2) \left| \frac{1}{r_{12}} \right| 1s_{\mathrm{A}}(1)1s_{\mathrm{B}}(2) \right\rangle, \tag{3.50}$$

α to the exchange integral

$$K_{\mathrm{AB}} = \left\langle 1s_{\mathrm{A}}(1)1s_{\mathrm{B}}(2) \left| \frac{1}{r_{12}} \right| 1s_{\mathrm{B}}(1)1s_{\mathrm{A}}(2) \right\rangle, \tag{3.51}$$

and Δ to the overlap integral

$$S_{\mathrm{AB}} = \langle 1s_{\mathrm{A}} | 1s_{\mathrm{B}} \rangle. \tag{3.52}$$

However these parameters are in general fit empirically rather than calculated.

Calculated surfaces for polyatomic molecules may use modifications of these functions to represent the interactions, including generalizations to three- and more-body

interactions, which are needed [38] to properly represent the surface features for short relative nuclear distances. As well, it is common to use an average of singlet and triplet terms for pairwise interactions between nuclei since usually a spin-independent surface is desired, otherwise at least two surfaces would be needed to compute rates for a given reaction. For example, the surface of Joseph *et al.* uses an average of functions (3.46) and (3.47) for pairwise interactions. This type of averaging has lead in the past [38] to spurious features on PES's arising from the difference in the properties for singlet and triplet potentials, particularly false local minima near the point of closest approach of reactants, and was not initially recognized as an artifact of the calculations. Modern PES's overcome this problem.

Chapter 4

Reaction Rates from Theory

4.1 Introduction

In this chapter are reviewed the best-known chemical reaction rate theories employing PES's. Many such theories have been proposed, and only a few are discussed here. It is worth noting that many theories, such as transition state theory, are developed by introducing rather restrictive assumptions, then trying to correct for the error produced by the assumptions. At the other extreme, development proceeds from formally exact equations to suitable approximations devised in such a way as to try to retain the rigour of the parent theory; an example is variational coupled channels theory.

For all types of theories, many general types of approximations have been tried; most notably, restricting the degrees of freedom of the reactants leads to simpler equations in every theory. For example, many atom-diatom reactions have been treated by restricting the reactants to collinearity. Also, coordinate transformations [48] of various types can simplify calculations.

Transition state theory (TST), and its many variants, has long been the most popular reaction rate theory. First proposed in 1935 by Eyring, Evans, and M. Polanyi [53], the theory combines equilibrium statistical mechanics with potential energy surfaces. A review, with definitions of the various versions of the theory, is to be found in reference [75]. *Conventional* TST (CTST) focuses on the properties of the *transition state* (TS) in a given reaction. The TS can be defined as a "saddle point" or "col"

on the minimum (i.e. least extreme) energy path on a PES between the reactants and products.

From the TS can be defined the *vibrationally adiabatic* (VA) reaction barrier E^{VA} as

$$E^{\mathrm{VA}} = V^b + \sum_{\nu} E^{\ddagger}_{\nu} - \sum_{\nu} E_{i,\nu} \tag{4.53}$$

with V^b the (classical) PES barrier height and $\sum_\nu$ denoting the sum of energy in each vibrational mode (with rotational states averaged), $\ddagger$ the TS, and i the reactants. This quantity denotes the actual energy barrier for reaction where the reactants evolve to the TS with no change of vibrational state. As normally seen in the literature, this quantity is usually quoted as the vibrationally adiabatic energy barrier with reactants and TS in their ground vibrational states. This quantity, denoted V^{G} here, then corresponds to the sums $\sum E_\nu$ counting zero-point energies only.

The energy V^{G} should give a better estimate of E_a than V^b. It is possible for V^{G} to be less than V^b. The two can in fact be significantly different, and the use of V^{G} in any rate theory partially takes account of the quantization of internal states of reacting molecules. It is certainly a better estimate of the true average energy barrier than is V^b.

For isotopic variants of a reaction, when the vibrational energy is included with the electronic energy given by the PES, the energy profile of the reaction is no longer isotopically invariant. The V^{G} differences for isotopic variants can be expected to give a reasonable estimate of E_a differences for given reaction. For example, comparing reactions of two isotopic variants A_a and A_b of atom A:

$$V^{\mathrm{G}}(\mathrm{A}_a) - V^{\mathrm{G}}(\mathrm{A}_b) = \sum_{\nu,a} E^{\ddagger}_{\nu} - \sum_{\nu,b} E^{\ddagger}_{\nu} \tag{4.54}$$

so the difference in V^{G} is just the difference in vibrational energy of the respective transition states, certainly an intuitively reasonable estimate of the E_a difference. For a

reaction with significant populations of excited reactants, such as the title reaction (1.3), the agreement of isotopic V^{G} and E_a differences may not be as good since these reaction dynamics are more complicated than for reactions of only ground states.

Comparing the D and H atom variants of reaction reaction (1.3), the V^{G} value for the D atom variant given by the *ab initio* surface of Walch *et al.*, [26] is 0.93 kcal/mol lower than that for H. This is reasonably close to their theoretical E_a difference (using CTST at 500 K) of 0.8 kcal/mol, and consistent as well with an experimental value of uncertain accuracy [25], (mentioned in Chapter 1), of 0.6 kcal/mol.

Following a variational principle analogous to that for stable molecules, the TS can be gotten using variational optimization of geometry to get a stationary value of $\langle E \rangle$, starting with a geometry near the expected TS. That is, the TS is located at the highest energy point on a path requiring the lowest energy to transverse classically. This path, called the minimum energy path, is for the PES of Figure 3.1, the dotted path.

4.2 Transition State Theory

Essentially, this theory assumes the following [53]:

1. Once the path s has been followed to the col, the reactants do not turn back. This is called the *no-recrossing rule.*

2. The reactant molecules obey the Boltzmann distribution of equation (2.16). Furthermore, *equilibrium theory* can be used to find the concentration of the TS in relation to the reactants.

3. The motion along s is separable from all others. Formally this results in an imaginary frequency for this unbound motion.

4. Motion along s is classical.

Clearly, this theory will perform best for reactions with high reaction barriers with the product side steeper than the reactant side, like the "cliff" on the left side of Figure 4.2. Compare the shape of the barriers V^b and V^G from a PES for the H atom variant of the title reaction (1.1). For a barrier of this shape the TS will be unlikely to go back to reactants. Also, when the TS is high in energy it will be formed rarely enough that it will be unlikely to exceed the calculated equilibrium value of concentration.

These assumptions lead to a rate coefficient

$$k = \frac{kT}{h} \frac{q_\ddagger}{\prod_i q_i} \epsilon^{-E_0/RT} \tag{4.55}$$

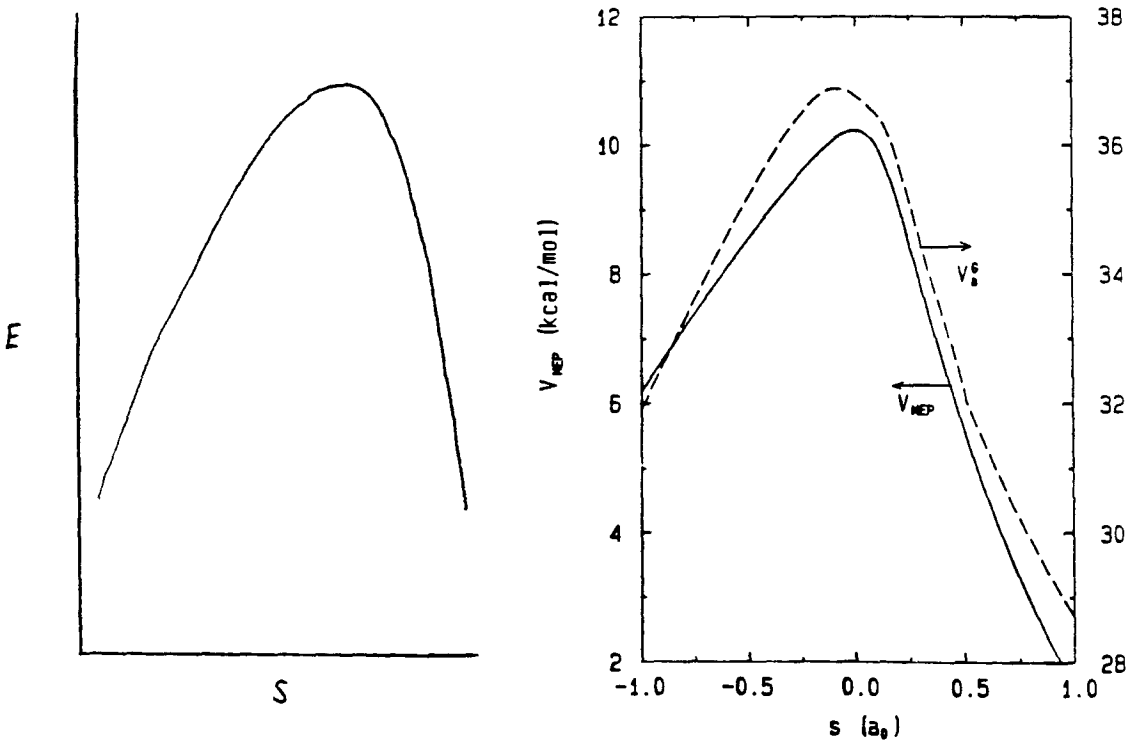

Figure 4.2: Left: potential energy "cliff"; ideal system for TST. Right: profile of classical reaction barrier (called V^b in text; here called V_{MEP}, left scale) and vibrationally adiabatic reaction barrier (V^G, right scale) from a recent semi-empirical potential energy surface for the title reaction (1.1); reproduced from [70].

where $q_\ddagger$ is the partition function of the TS with motion in the s-direction omitted, E_0 the molar value of V^G (*not* the reaction's threshold energy), and q_i the partition functions of the reactant species i. This expression is, within a multiplicative constant, the formal equilibrium constant[1] of the TS species [53]; that is, the reaction rate is proportional to the concentration of the TS. Furthermore, the resemblance of this equation to the Arrhenius equation (2.18) is rather striking.

It is to be noted that the full PES is not at all needed to do this calculation, only the regions of the reactants and the TS, needed to calculate the partition functions q_i and $q_\ddagger$. These are weighted sums of the state functions for nuclear motion in the molecule i or $\ddagger$ as discussed in Chapter 2. The nuclear state functions can be estimated without the use of a PES for the reaction, by considering the motions of the reactants and TS separately. Therefore a CTST rate coefficient can be gotten without a full PES.

TST has the advantage over other rate theories of having a very simple form for kinetic isotope effects. The only difference in the TST k for isotopic variant reactants is the difference in $q_\ddagger$ and the q_i. It is to be expected that the isotopic *ratios* from TST may be more accurate than the absolute rates since many factors cancel in this calculation, leaving [48]

$$\frac{k_1}{k_2} = \frac{q_\ddagger^1 q_2}{q_\ddagger^2 q_1} e^{-(E_0^1 - E_0^2)/RT} \tag{4.56}$$

for isotopic variants 1, 2 of any of the reactant species i. In the case of the present study, some of the CH_4–Mu TS vibrational frequencies will be significantly higher than for CH_4–H, and TST would be expected to predict correspondingly high ratios k_H/k_{Mu}. In comparing Mu and H atom data, the initial partition functions are not changed and so there results

$$\frac{k_{Mu}}{k_H} = \frac{q_\ddagger^{Mu}}{q_\ddagger^{H}} e^{-(E_0^{Mu} - E_0^{H})/RT} \tag{4.57}$$

[1] Following the use of the term "rate coefficient", the "equilibrium constant" might better be called the "equilibrium activity quotient".

a simpler result still.

More sophisticated versions of this theory partly or completely remove some of the assumptions of CTST. *Generalized* TST is TST with an arbitrary location of the TS. Use of an alternate TS can remove some of the inaccuracy introduced by the no-recrossing assumption, by moving the TS to a location where less recrossing occurs for the real system. *Variational* TST is based on the fact [75] that classically, the k of TST is an upper bound to the true rate coefficient. Therefore, VTST finds the generalized TS giving the lowest k. This is not true quantum-mechanically but VTST is still generally more accurate than CTST. Of course, far more computation is required: an optimization procedure must be followed, with a TST calculation at each point.

Many other procedures [53,75] have been tried to improve TST and cancel the errors resulting from its assumptions. For example, even in the variational form, the no-recrossing assumption still leads to error. Also, the theory fails to account for quantum effects such as tunneling. As well, various features of the PES such as that for H + H_2, can affect the behaviour of the TS. For example, the conventional TS on a completely symmetric PES such as that of H + H_2 is equally likely to go back to reactants as to proceed to products. It would then be appropriate to multiply expression (4.55) by one-half. On an essentially *ad hoc* basis, these effects are combined to form a *transmission coefficient*, κ, defined such that the rate coefficient takes the form

$$k = \kappa \frac{\mathrm{k}T}{h} \frac{q_{\ddagger}}{\prod_i q_i} e^{-E_0/\mathrm{R}T}. \tag{4.58}$$

The problem of the quantization of the reaction coordinate s and its nonseparablility from the other coordinate in the real TS have also been addressed. Reference [76] discusses the requirements for "an exact quantum mechanical" TST. Practical application of many such methods is discussed in reference [77].

The review [75] considers some of the ways used to seek an accurate value for κ, and reference [78] explores the requirements for "exact" tunneling corrections by comparing TST calculations to accurate scattering calculations. Frequently used is the Wigner first-order tunneling correction, whose accuracy is discussed in reference [79]. This gives the transmission coefficient

$$\kappa^{\mathrm{W}}(T) = 1 + \frac{1}{24}\left(\frac{\hbar\omega^{\ddagger}}{\mathrm{k}T}\right)^2 \tag{4.59}$$

which can improve some TST calculations (*ibid.*). It is to be noted though that this expression is most accurate at *high* T, where tunneling is less important in determining the reaction dynamics than at low T.

4.3 Some Forms of Collision Theory

Theories which directly calculate the reaction cross-section of equation (2.15) are essentially variants of *collision theory.* For an elementary bimolecular reaction between species A and B the rate is given [53] by the expression

$$R = \sigma(v) v N_{\mathrm{A}} N_{\mathrm{B}} \tag{4.60}$$

with N_{A} and N_{B} the number density of A and B, and other quantities defined in equation (2.15). Using the definition of k_i that equation is obtained.

Simple collision theory assumes that A and B are hard spheres, that the potential energy between A and B is zero beyond the sum of set radii for A and B, and infinite at closer range. A "collision" then corresponds to the classical idea of solid objects hitting each other. The theory then assumes that all collisions result in reaction. These assumptions lead [53] to the expression

$$k = (r_{\mathrm{A}} + r_{\mathrm{B}})^2 \left(\frac{8\pi\mathrm{k}T}{\mu}\right)^{1/2} \tag{4.61}$$

for the reaction, with μ the reduced mass of the reactants. This agrees with the expression obtained [48] by CTST for this potential. This is the same as the simple "line of centers" model discussed in Chapter 2, with zero energy threshold. Of course, even with appropriate values of r_A and r_B, the theory is often not even of qualitative use due to its deep approximations. Early work focused on correcting k by multiplying by a "steric factor" P to correct for such things as the real geometry of molecules, but was inadequate as a general theory.

Trajectory theory calculates σ using a PES, essentially by placing the molecules in close proximity, letting them go, and observing the result—a "black box" approach. A suitable set of initial conditions is used to devise the initial conditions for a set of trajectory calculations, whose results are then averaged. Frequently, the initial conditions are chosen at random assuming the Boltzmann distribution of initial states. The motion of the nuclei on the PES are generally found by numerical solution of Hamilton's classical equations of motion [80]:

$$\frac{dq_i}{dt} = \frac{\partial H}{\partial p_i} \tag{4.62}$$

$$\frac{dp_i}{dt} = -\frac{\partial H}{\partial q_i} \tag{4.63}$$

with H the classical Hamiltonian, q_i the generalized coordinates of the system (not the partition functions), and p_i the momenta conjugate to the coordinates q_i.

The theoretical results are often competitive with those of TST in comparison with experimental data. For one series of comparisons, of calculations on the isotopic variants of reaction (1.7), see [81]. Normally, the initial states are quantized if the quantum-mechanically correct states are used to form them; the final states typically must be "binned" by an essentially arbitrary procedure to the correct quantized final states, since the reactants drift under Hamilton's equations to a continuum of states. This is *quasi-classical* trajectory theory. Extensions are possible to further increase the

quantum-mechanical correctness of the theory, the most obvious being the addition of zero-point molecular vibrational energies to the PES energies. Truhlar compares a variety of versions of this theory with TST in reference [82].

Versions of *reactive scattering theory* have been widely used in the study of nuclear and particle interactions for many years, and the theory is well developed; a modern advanced quantum mechanics text will contain much detail on this subject. Scattering theory calculates the cross-sections from rigorous quantum-mechanical principles, by computing the evolution from initial to final states by the solution of an appropriate version of the Schrödinger equation.

Normally, the time dependence is factored out [83] by representing the total state function as a sum of ingoing and outgoing "waves", but a calculation has been done [84] for the rate of reaction (1.7) using the full time dependent wave packet formalism. The **S** matrix, which when combined with appropriate boundary conditions, gives the relative amplitudes of initial and final states, is obtained by substituting the ingoing/outgoing sum into the time-dependent Schrödinger equation. The **S** matrix is essentially [85] an operator for transforming the initial state (reactants) at time $-\infty$ to the final state (products) at time ∞.

Many types of approximate methods exist for rigorous scattering theory, but for chemical reactions a key development has been the development of variational methods. The variational principle for scattering does not follow as simply as those for TST and electronic energy, but as shown by Ramachandran and Wyatt [86], variational methods similar to those used in MO theory can give accurate answers with less computational effort than nonvariational methods. In the *coupled channels* theory, the state function is expanded in a basis set as in SCF-MO theory, with the expansion coefficients found by considering the boundary conditions matching initial to final states. This is a very

complicated mathematical theory when applied to molecules, and a common approximation is *centrifugal sudden*, which essentially [87] assumes rotational adiabaticity in the reaction. This is the theory applied so successfully to reaction (1.8) by Schatz.

4.4 Theoretical Rate Parameters for the Title Reactions

4.4.1 $Mu + CH_4 \rightarrow MuH + CH_3$

There are no available calculations for the Mu atom isotopic variant of the reaction (1.1). However a number of calculations exist for other isotopic variants. For the translationally excited ("hot") tritium (T^*) atom variant trajectory calculations were first done [88] using a semi-empirical PES that treated the CH_3 group in CH_4 as a single mass point. Later calculations [89], treating all H atoms as equivalent and reactive, gave good agreement for T^* above 400 kcal/mol. The semi-empirical surface of Joseph *et al.* [70] is a modification of this surface, and has been used to get the most accurate (albeit semi-empirical) available theoretical rates for reaction (1.7) using VTST; see Figure 4.3, which compares these calculations to *ab initio* calculations of Schatz *et al.* [73]. More recently [40,90], the surface has been used in studies of various isotopic variants of this reaction, and its reverse, partly to establish benchmarks for application of VTST to polyatomic molecules.

Ab initio calculations using a large basis set and CI (POL-CI), of Walch [72], extended by Schatz *et al.* [26,73], on only the region of the reaction barrier (CH_4–H) and reactants (CH_4) were used (*ibid.*) to calculate conventional TST rate coefficients. In the same reference, TST results for one other *ab initio* surface and several semi-empirical ones were calculated, and compared to the POL-CI results. These showed the latter to compare the best with experiment. The Arrhenius fit is compared to the calculations of Joseph *et al.* in Figure 4.3. Noting that the curve from the POL-CI calculations is too

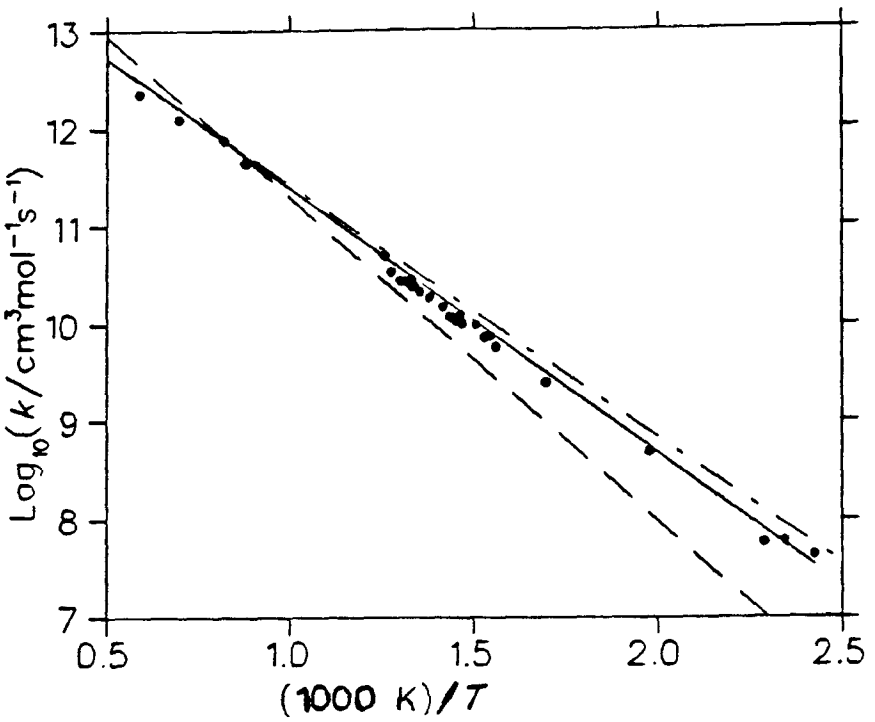

Figure 4.3: Arrhenius plot of experimental and theoretical rate coefficients for H + CH_4 abstraction reaction. Experimental data (solid line) from reference [18]. Dashed line data from POL-CI CTST calculations of Schatz *et al.* [73]; dash-dot line from VTST calculations of Joseph *et al.* [70] on a semi-empirical surface. Reproduced from [31].

steep, it is to be expected that the POL-CI calculated barrier of 13.5 kcal/mol is too high. Later work [26] shows that the (arbitrary) use of a barrier height of 12.5 kcal/mol gives results in better agreement with experiment.

The same POL-CI geometries were used [26] to calculate rates for a variety of isotopic variants of reaction 1.1, shown in Table 4.3 for two forms of the (generalized) Arrhenius equation. As discussed in the previous chapter, comparing the H + CH_4 and D + CH_4 results, the E_a difference is 0.8 kcal/mol compared to a V^G difference of 0.9 kcal/mol from the same reference; the D atom reaction is lower in each quantity, which would be expected since the TS involving D will have lower vibrational energy

Table 4.3: Rate coefficients for H + CH_4 and isotopic variants, using $V^{\ddagger} = 13.5$ kcal/mole. Parameters k, A' and A are in L/(mol s), B' in ln(K), and temperatures in K. Activation energy at 500 K in kcal/mol. Table from reference [26].

$$\ln k = A' + B' \ln T - C/T = \ln A(T) - E_a(T)/RT$$

reaction	A'	B'	C'	$k(500)$	$E_a(500)$	$A(500)$
H + CH_4	10.91	1.974	5640	1.5×10^5	13.2	8.4×10^{10}
H + CD_4	13.10	1.692	6462	4.4×10^4	14.5	9.8×10^{10}
D + CH_4	9.21	2.169	5157	2.4×10^5	12.4	6.3×10^{10}
D + CD_4	11.31	1.898	5963	7.2×10^4	13.7	7.2×10^{10}
H + $CH_3D \rightarrow H_2$	10.81	1.951	5646	1.1×10^5	13.2	6.4×10^{10}
H + $CH_3D \rightarrow$ HD	11.0	1.781	6422	1.0×10^4	14.5	2.3×10^{10}
D + $CH_3D \rightarrow$ HD	9.103	2.146	5162	1.8×10^5	12.4	4.8×10^{10}
D + $CH_3D \rightarrow D_2$	9.217	1.986	5926	1.6×10^4	13.7	1.7×10^{10}
H + $CH_2D_2 \rightarrow H_2$	10.59	1.928	5648	7.9×10^4	13.1	4.4×10^{10}
H + $CH_2D_2 \rightarrow$ HD	11.92	1.752	6434	2.1×10^4	14.5	4.6×10^{10}
D + $CH_2D_2 \rightarrow$ DH	8.886	2.123	5167	1.3×10^5	12.4	3.2×10^{10}
D + $CH_2D_2 \rightarrow D_2$	10.14	1.958	5936	3.4×10^4	13.7	3.5×10^{10}
H + $CHD_3 \rightarrow H_2$	10.10	1.903	5655	4.1×10^4	13.1	2.2×10^{10}
H + $CHD_3 \rightarrow$ HD	12.56	1.723	6446	3.2×10^4	14.5	7.1×10^{10}
D + $CHD_3 \rightarrow$ HD	8.382	2.100	5169	6.6×10^4	12.4	1.7×10^{10}
D + $CHD_3 \rightarrow D_2$	10.78	1.929	5948	5.3×10^4	13.7	5.3×10^{10}

due to the higher mass of the D atom compared to H. This is a good example of a kinetic isotope effect resulting from the zero-point energy shift in the TS. Note that the D atom relative rate increase may be partially offset by its less ready tunneling, but this effect does not appear strong. On the basis of these results the Mu atom reaction TS might be expected to be raised by several kcal/mol, but it is important to recognize that this figure assumes that the TS is unchanged in location from that in the H atom reaction. A significant change in the location of the TS for the Mu atom reaction could have other effects on the E_a depending on the detailed features of the PES and vibrational energy in the TS involving Mu.

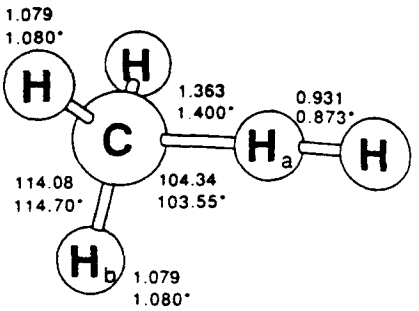

Figure 4.4: Diagram of TS for the H + CH_4 reaction. Distances are in Å, angles in degrees, and are for two different *ab initio* calculations. Reproduced from reference [39].

Most recent *ab initio* CTST calculations [39] use only TS and reactant geometries optimized by SCF with MP theory to fourth order. The results are almost as good as the POL-CI ones with a corrected barrier height, but k is systematically underestimated. This is attributed to the too-large barrier height of 13.0 kcal/mol. The geometry of the TS, shown in Figure 4.4, is similar to that calculated by the POL-CI calculations and the geometry of a TS found [40] with VTST on the surface of Joseph *et al.*

From the reaction profile in Figure 4.2, it is clear that this reaction is similar in its reaction profile to the ideal "cliff" system; therefore TST should be expected to work well, as the available calculations seem to indicate.

4.4.2 $Mu + C_2H_6 \rightarrow MuH + C_2H_5$

For the corresponding C_2H_6 reaction, calculations of the same quality as for CH_4 do not exist. As stated in reference [44], "nothing is known" about the PES for H + C_2H_6.

The only recent calculation of any kind considering this reaction is a 1991 article [41], which gives the results of calculations using SCF/(second-order MP) for the reactants, TS, and products. The theory used is the "curve crossing model" which [91] essentially calculates the energy along the reaction coordinate from the overlap between the state

functions of reactants, products, and TS along the reaction coordinate, giving a reaction barrier. The vibrationally adiabatic barrier, which the authors called the "activation energy", is computed to be 22.9 kcal/mol, but the relationship between this energy and the experimentally measured E_a, though commented upon, is not given.

This study also treated the corresponding methane reaction. Their barrier for the corresponding reaction of CH_4 is 25.6 kcal/mol, slightly lower than that given by the PES's of Walch *et al.* and Joseph *et al.* discussed above (both ~26.5 kcal/mol). The barrier difference for these two reactions, 2.7 kcal/mol, is reasonably close to the E_a difference obtained from the experimental values of reference [6].

Given the similarities in the electronic structures of CH_4 and C_2H_6, it is likely that the salient features of their respective PES's with respect to reaction with H (or Mu) are similar. Therefore, isotopic substitution H $\rightarrow$ Mu is likely to have similar effects on the reaction dynamics, and therefore the bulk kinetics, of both reactions.

Chapter 5

Experimental Setup

5.1 Positive Muons and μSR

The μSR technique is possible because of the parity-violating (chiral) nature of the decay of the μ^+ parent, the positive pion π^+:

$$\pi^+ \rightarrow \mu^+ + \nu_\mu \tag{5.64}$$

which arises because the neutrino ν can have only negative helicity (the maximum spin projection opposite the direction of momentum). By conservation of angular momentum the μ^+ ($s = 1/2$) is then also required to have negative helicity when produced from such a decay. This fact allows scientists to obtain nearly 100% polarized beams of μ^+, and also μ^- by the analogous π^- decay, in modern particle accelerators. The muon decays with a mean lifetime of 2.2 μs:

$$\mu^+ \rightarrow \mathrm{e}^+ + \nu_\mathrm{e} + \bar{\nu}_\mu \tag{5.65}$$

and the helicity of the neutrinos again leads to a chiral decay, resulting in a preferred direction of positron motion along the decaying muon's spin, with the number of positrons emitted in the angle pattern

$$\mathrm{N_e}(\theta) \propto (1 + A\cos\theta) \tag{5.66}$$

where θ is the angle between a given direction and the maximum projection of the muon spin, and A is called the decay *asymmetry*. The average of A for emitted positrons of

all possible energies is 1/3. In experimental practice, the detected A is not 1/3, and is always measured empirically.

For an initially 100% polarized muon beam, the excess spin in the direction opposite the initial motion with respect to the decaying pion constitutes left-handed polarization, when the muons are treated as an ensemble. The ergodic principle allows the muons in the beam, an ensemble in time, to be treated the same as an ensemble in space. The effect is to treat the muons in a beam over a period of time as if they were a single, macroscopic pulse of particles.

When a beam of energetic (~MeV) μ^+ enters an experimental target such as the gases under study here, these muons undergo [27] Bethe-Bloch ionization of the stopping medium, falling to an energy in the ~100 keV [30] range for gases. This process does not affect the muon polarization. The regime of slowing from ~100 keV to thermal energy does affect the polarization, through a repeated process of *cyclic charge exchange*:

$$\mu^+ + \mathrm{e}^- \leftrightarrow \mathrm{Mu} \tag{5.67}$$

with electrons from the molecules of the stopping medium. This process continues down to muon energy ~10 eV depending on the gas (*ibid.*). Assuming an initially 100% polarized muon beam (all μ^+ in state $|\alpha_\mu\rangle$) two spin states of Mu can be formed, with the muon and electron spins parallel $|\alpha_\mu\alpha_\mathrm{e}\rangle$, or antiparallel $|\alpha_\mu\beta_\mathrm{e}\rangle$; in the antiparallel state, as discussed below, the muon spin is affected by the hyperfine interaction due to the electron spin. In a dilute gas, residence times of a muon in a neutral (Mu) environment may be long compared to the time needed to depolarize the muon in Mu from the initial ensemble polarization; in a denser medium collisions are more common and residence times will be correspondingly shorter. The characteristic time for depolarization is the time $1/\omega_0$, where $\nu_0 = \omega_0/2\pi$ is the hyperfine frequency, 4463 MHz for Mu.

Following the charge-exchange regime, muons slow down by elastic, inelastic, and reactive collisions in gases (*ibid.*) to thermal kinetic energies. After thermalization, some fraction of incident muons will be in the form of Mu and some in diamagnetic environments, such as molecular ions (e.g. N_2Mu^+), or diamagnetic molecules such as MuH, which are indistinguishable from bare muons μ^+ given current experimental resolution. In some gases muons may also thermalize in muonated free radicals such as C_2H_4Mu. The fraction thermalizing in each environment is a strong function of the stopping gas density and composition. The phenomena contributing to the determination of the relative fractions have recently received much experimental and theoretical study. They provide a way, albeit model-dependent, to estimate hot atom (Mu^*) reaction rates [92], similar to that used in hot hydrogen (H^*) and tritium (T^*) studies. These rates have been measured for several reactions of Mu^* including the title reactions; see *ibid.* for a recent summary.

In gases, the muons will stop (i.e. thermalize) over a range of distances into the gas target. The average stopping distance is inversely proportional to the electron density in the medium since the energy loss processes of the muon principally involve collisions with electrons. The entire thermalization process typically takes ~50 ns [93] for gas pressures ~1 atm; less for higher pressures.

5.1.1 μSR and MSR

If the muon target in which a polarized muon beam is stopped is in a uniform magnetic field **B**, μSR (muon spin rotation, or relaxation, or resonance) studies are possible. Conventionally, this field is either along the direction of initial muon polarization ("longitudinal") or perpendicular to it ("transverse"). The acronym μSR denotes several types of studies employing muon polarization. In general each works by providing data which is fitted to the solution of appropriate equations of spin motion, with suitable

variable parameters.

The asymmetry in the decay (equation (5.66)) has the same motion as the muon spin, and the motion is observed by the pattern of detection of the positrons from muon decay. In the limit of an infinite number of "events" (muon decays included in the fit), the ensemble will reproduce the equations of spin motion. A suitably high number of events for a reasonable approximation to this limit depends on the parameters of most interest in the particular experiment; for the experiments here reported approximately two million events were collected for each experimental run.

The detectors used in μSR are the same as those used in nuclear and particle physics scattering experiments, which are also components of the experimental program at TRIUMF, as is detector development. Commonly called "counters" since they "count" decay events, they are made of a plastic which produces a "cascade" of light, called a "scintillation", when struck by a particle, such as e^+, at high energy[1]. This is converted to a current pulse by a photomultiplier and transmitted down a coaxial cable. For many applications it is desirable to reduce background signal from false counter triggering by using counters in coincidence: requiring simultaneous triggering of several counters placed parallel to each other to register a signal.

The pulse from a counter is converted to a digital one and usually, treated by a "discriminator" which filters low height pulses, easily distinguishable from the true signal by visual observation. The signal is then treated by a logic circuit, which combines the signals from the various counters to physically meaningful data. The data is collected by a minicomputer program receiving input from the logic circuit.

In *time-differential* μSR experiments A is a function of time, called the "signal" $S(t)$. For a particular muon, the time zero is set by the time at which it enters the target medium, through a thin scintillation counter, and t is defined by the time at

[1] compared to thermal.

which a decay positron is detected by another counter. With the radioactive decay of the muons due to the mean muon decay lifetime, denoted τ, a normalization factor N_0, and a background parameter B_g to account for noise in the positron counter and background radiation, the events are fitted to the function

$$N(t) = N_0 e^{-t/\tau}[1 + S(t)] + B_g \tag{5.68}$$

for each positron counter (or counters in coincidence) in use. The time resolution is finite, set in principle by the time for light to travel the spatial dimensions of the counters, and the events are histogrammed into "bins", each of a given width, typically ~20 ns. "Veto" mechanisms in the logic circuit ensure that the positron detected at time t indeed comes, with great certainty, from the muon detected at time zero. The total length of the histogram is typically several muon mean lifetimes (~10 μs), beyond which few muon decays are detected, and whose length is also determined to optimize the veto mechanisms.

In *integral* μSR $S(t)$ is obtained by forming the quantity

$$S(t) = \frac{N_- - \alpha N_+}{N_- + \alpha N_+} \tag{5.69}$$

where the N's are numbers of detected decays over a reasonable period of time and + and - denote positron counters oppositely placed with respect to the target, with the empirical parameter α accounting for the difference in counting efficiency of the two counters.

The equation of motion for the muon spin in either the Mu or diamagnetic environments have been solved many times (e.g. [27,30]) and will not be discussed in detail here. Briefly, for a muon in a diamagnetic environment the muon spin evolves according to the Hamiltonian

$$\hat{H} = \boldsymbol{\mu}_\mu \cdot \mathbf{B} \tag{5.70}$$

where $\boldsymbol{\mu}$ is the magnetic moment operator defined for any particle p as

$$\boldsymbol{\mu}_{\mathrm{p}} = \frac{g_{\mathrm{p}} e_{\mathrm{p}}}{2 m_{\mathrm{p}} c} \mathbf{J}_{\mathbf{p}} \tag{5.71}$$

with the quantities $\mathbf{J}$ the particle's angular momentum operator, m its mass, g its quantum "g-factor" and e its charge. For a free muon, $\mathbf{J}$ is just its spin angular momentum $\mathbf{S}$, which has the same eigenvalues $\pm\hbar/2$ as the electron. Then $|\boldsymbol{\mu}_{\mu}|$ takes the value [27] 4.47×10^{-23} erg/G, reduced from that of electron just by the ratio of their masses, 207.8. For later reference is defined

$$\beta_{\mathrm{p}} = \frac{e_{\mathrm{p}} \hbar}{2 m_{\mathrm{p}} c} \tag{5.72}$$

the "Bohr magneton".

In a longitudinal field, either spin eigenstate of the bare muon is an eigenstate of the Hamiltonian and the signal detected by a positron detector is of the form (*ibid.*)

$$S(t) = A_{\mathrm{D}} G(t) \tag{5.73}$$

where A_{D} is a constant representing the amplitude of the diamagnetic signal and $G(t)$ is a *relaxation function* accounting for loss of polarization due to interactions of the muon spin with the medium. While A_{D} is intended to represent A of equation (5.66) integrated over the area of the positron detector, it is, as mentioned earlier, always measured empirically by fitting $S(t)$. For a tranverse field, the signal takes the form (*ibid.*):

$$S(t) = A_{\mathrm{D}} \cos(\omega_{\mathrm{D}} t + \phi_{\mathrm{D}}) \tag{5.74}$$

for a detector in a direction perpendicular to the applied field. The fitted parameter ϕ_{D} accounts for rotation of the spin direction during beam delivery and thermalization. The parameter ω_{D} is the Larmor frequency $2\pi g_{\mu} |\mathbf{B}|/\hbar$ of the muon, corresponding to

classical magnetic moment "precession" in a magnetic field: the maximum muon spin projection "sweeping" past the counter with the angular frequency

$$\omega_{\mathrm{D}} = 2\pi\gamma_{\mu}|\mathbf{B}| \tag{5.75}$$

where the gyromagnetic ratio γ_{μ}, gotten from μ_{μ} and g_{μ}, is 0.0136 MHz/G.

For free muonium (in the $1s$ electronic state) in a uniform magnetic field the Hamiltonian is (*ibid.*)

$$\hat{H} = \boldsymbol{\mu}_{\mu} \cdot \mathbf{B} + \boldsymbol{\mu}_{\mathrm{e}} \cdot \mathbf{B} + \hbar\omega_0 \, \mathbf{S}_{\mathrm{e}} \cdot \mathbf{S}_{\mu} \tag{5.76}$$

in which the first two terms represent the individual interactions of the muon and electron spins with the external field, the third term the isotropic *hyperfine interaction* between their spins. The hyperfine frequency $\nu_0 = \omega_0/2\pi$, as above, is 4463 MHz, given by

$$\nu_0 = \frac{8\pi}{3} g_{\mathrm{e}} g_{\mu} \beta_{\mathrm{e}} \beta_{\mu} |\psi_{1s}(0)|^2, \tag{5.77}$$

proportional to the electron amplitude squared, $|\psi_{1s}(0)|^2$ at the muon, and about three times that of the hydrogen atom (1420 MHz).

The interaction results in coupling between the individual spin eigenstates. The energies of the four eigenstates of this Hamiltonian are shown, as a function of $\mathbf{B}$, in Figure 5.5, which also details the asymptotic features of the eigenstates, labelled by usual μSR convention. The most notable features of the figure are the approach to product eigenstates at high field as well as approach of the energies to linear functions of $\mathbf{B}$. It is also of note here that there is not any evidence for Mu surviving in excited electronic states after thermalization in gases, which would be obvious from a signal of much different characteristic frequency, although some may be initially formed (*ibid.*) in excited states. As well it should be noted the frequencies ν_{34} and ν_{14} are too high to be measured by μSR whose best time resolution is $\sim$1 ns, leading to a Mu signal reduced in amplitude by just one-half.

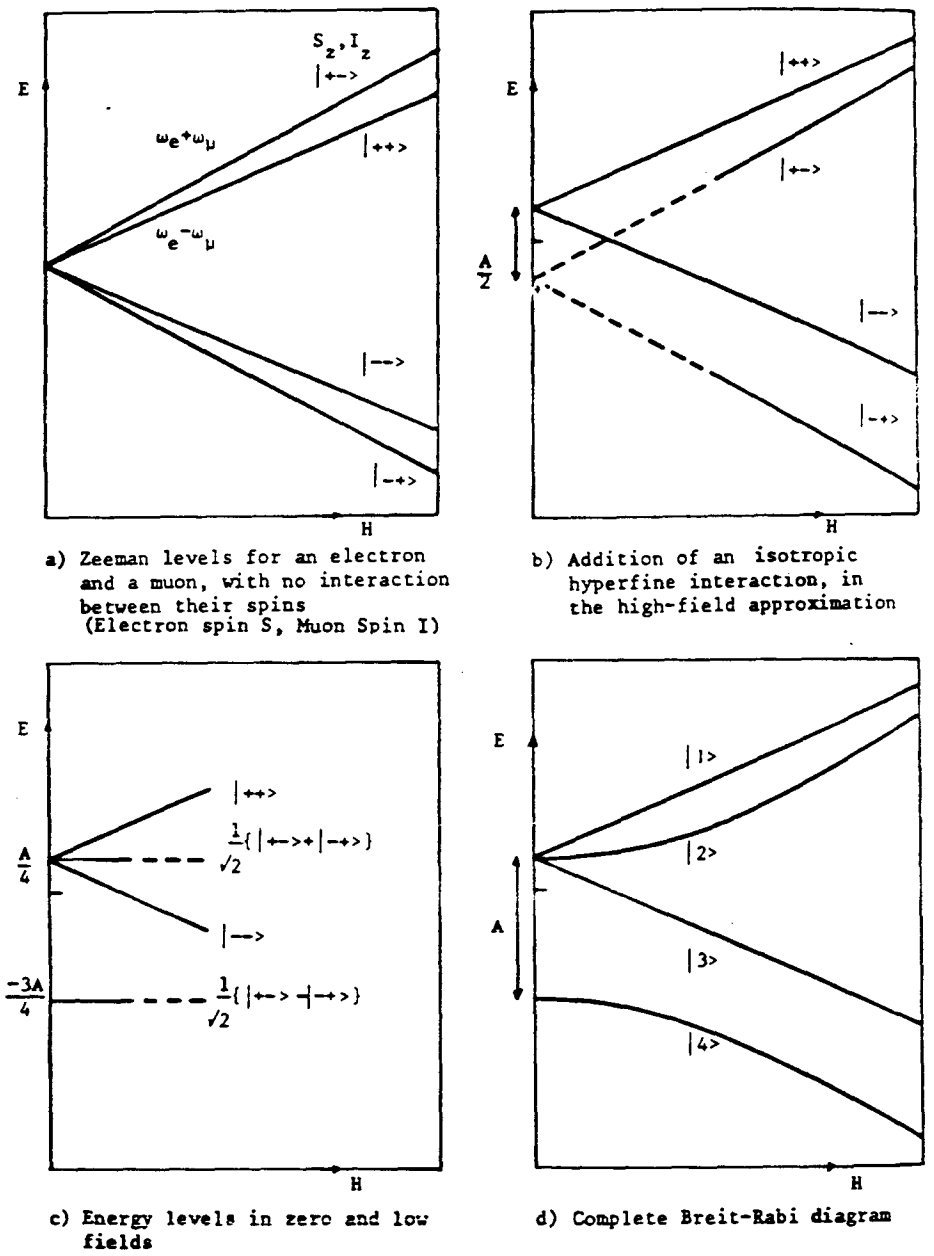

Figure 5.5: Progressive construction of the Breit-Rabi diagram for eigenenergies of stationary states of free muonium as a function of magnetic field. At low field, the eigenstates are close to the coupled representation states $|Fm_F\rangle$ with F the total spin of muon and electron. At high fields the eigenstates approach the totally uncoupled individual spin product eigenstates $|m_{s,e}m_{s,\mu}\rangle$. The magnetic-dipole allowed radiative transitions are shown. The parameter "A" on the energy scales is $h\nu_0$. Reproduced from [94].

At very low fields (< 10 G), the frequencies ν_{12} and ν_{23} are essentially degenerate, at a frequency just about half that of the electron precession frequency—the signal is dominated by the electron spin precession. This is the field regime of the present study. Two frequencies are thus observed: the single coherent Mu frequency and the μ^+ (diamagnetic) precession frequency. The frequencies ν_{12} and ν_{23} lead to an observable signal because Mu is not initially formed in its hyperfine eigenstates. This μSR regime, weak field Mu precession, is sometimes called MSR (muonium spin rotation), and has found use as the method of choice for measurement of Mu reaction rates with gases. The signal resulting under these conditions is

$$S(t) = A_D \cos(\omega_D t - \phi_D) + A_{\mathrm{Mu}} G_{\mathrm{Mu}}(t) \cos(\omega_{\mathrm{Mu}} t - \phi_{\mathrm{Mu}}) \tag{5.78}$$

with the A's separate asymmetry parameters for the diamagnetic and muonium fractions, and G_{Mu} the relaxation function of the muonium fraction. The Mu frequency ω_{Mu} has the opposite sense of ω_μ and its value, given by

$$\omega_{\mathrm{Mu}} = 2\pi\gamma_{\mathrm{Mu}}|\mathbf{B}| \tag{5.79}$$

where $\gamma_{\mathrm{Mu}} = \nu_{12}/|\mathbf{B}| = \nu_{23}/|\mathbf{B}| = 1.39$ MHz/G, is just half of the free electron precession frequency, but 103 times the diamagnetic frequency ($\omega_{\mathrm{Mu}} = 103\omega_{\mathrm{D}} = \omega_{\mathrm{e}}/2$). With very few exceptions [30], even for low ionization potential gases, in which 100% Mu formation might be expected by capture of the weakly bound electrons, the diamagnetic fraction is always present for the pressure regimes (< 20 atm) of the present study. For such low fields, no relaxation is observable for the diamagnetic fraction since it goes through less than a full cycle over several mean muon lifetimes.

For chemical reactions which place Mu in diamagnetic environments, such as the title reactions (1.3) and (1.4), and under the pseudo-first order conditions mentioned in Chapter 2, the ratio $A_{\mathrm{Mu}}(t)/A_{\mathrm{Mu}}(0)$ corresponds to $[\mathrm{Mu}](t)/[\mathrm{Mu}]_0$. The "concentration" [Mu] need not be known. Then, the relaxation function in the MSR regime, by

comparison of the result of chapter 2, is just

$$G_{\mathrm{Mu}}(t) = e^{-\lambda t} \tag{5.80}$$

where the relaxation rate parameter

$$\lambda = k[\mathrm{HR}] + \lambda_0 \tag{5.81}$$

and the "background" relaxation λ_0, is attributed to experimental artifacts, the most likely being an imperfectly homogenous magnetic field over the stopping range of the muons. Standard linear least-squares fitting procedures give the parameters λ_0 and k and their estimated experimental uncertainties. This relaxation, due to a thermal chemical reaction is shown in Figure 5.6 in which MSR signals of N_2 and CH_4 gas at 821 K are compared at equivalent muon stopping densities.

The relaxation of the muonium ensemble for this type of chemical reaction comes about because the process of chemical reaction, which places the muon in a different magnetic environment, removes the reacting Mu atom from the ensemble by changing its precession frequency to essentially random values during the course of reaction. In general, the molecular interaction times in the process of individual chemical reactions are short (typically ≤ 1 ns [30]) compared to the time resolution of the measurement, resulting in essentially instantaneous loss of coherence from the ensemble.

The parameters k and λ_0 can be obtained for a given gas temperature by measuring λ at several concentrations (i.e. partial pressures) of the reactant gas HR. The reaction under study has a relatively small rate coefficient and so high pressures (up to $\sim$17 atm) of reactant, and high temperatures (up to 821 K) were used. Under these conditions, in order to maintain a constant magnetic environment of the reacting Mu, it is necessary to add a inert "moderator" gas, N_2 in this study, to maintain a constant average Mu stopping distance at each concentration other than the highest. Also a run with just

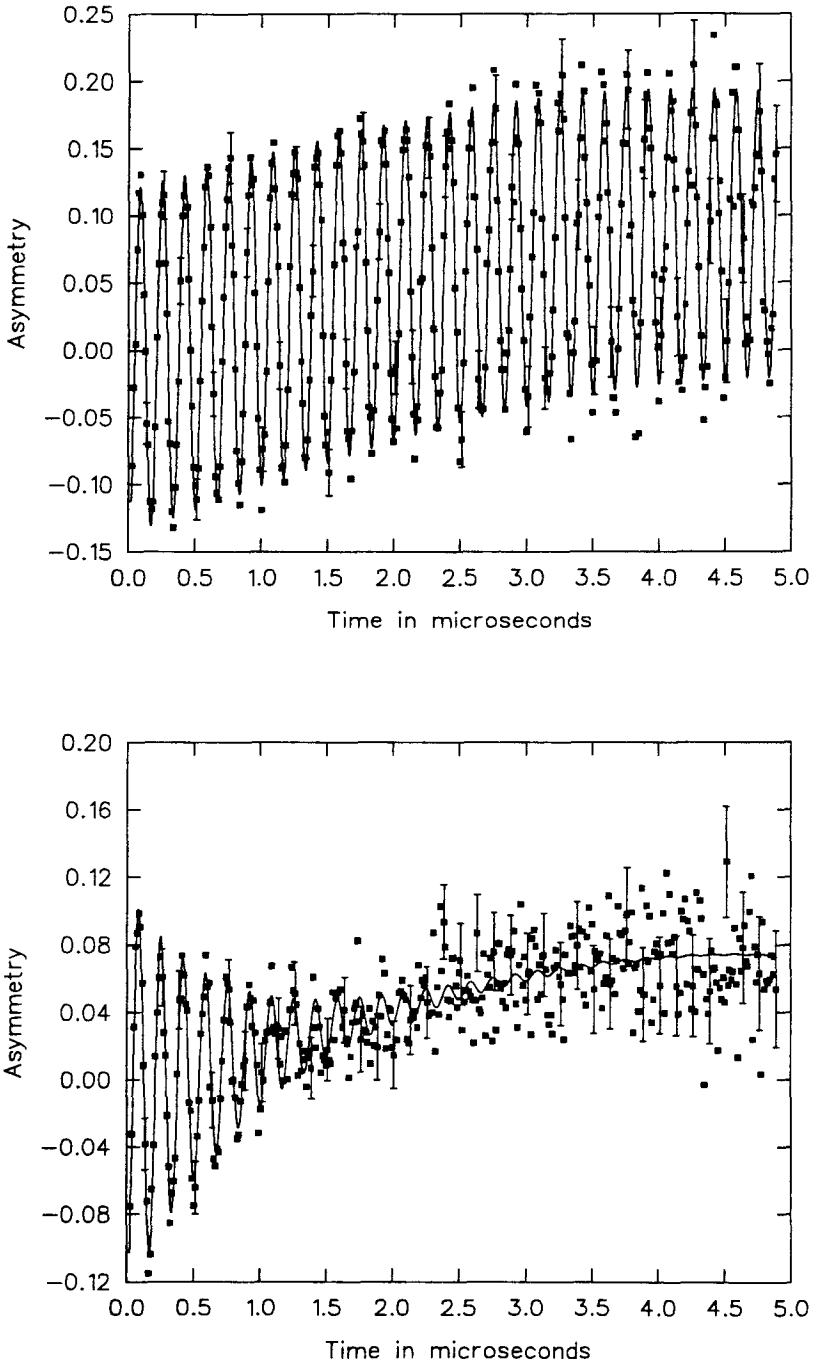

Figure 5.6: MSR signals for N_2 and CH_4 at 6.1 and 8.6 atm pressure, respectively, both at ~821 K. The small relaxation in the N_2 signal (top), 0.026 μs^{-1}, is identified with the "background" relaxation λ_0. The relaxation 1.147 μs^{-1} in the CH_4 signal (bottom) is attributed to chemical reaction resulting in loss of Mu coherence. Signals are nonlinear least-squares fits using the program MINUIT [95]. The λ vs. concentration plot for CH_4 at this temperature is shown in Figure 5.7.

the moderator gas is performed to increase the accuracy in the determination of the intercept λ_0. Plots of the equation (5.81) at each experimental temperature, for each of the two reactions studied, are to be found in the Appendix. Again for reference, the reactions of interest are:

$$\mathrm{Mu} + \mathrm{CH_4} \rightarrow \mathrm{MuH} + \mathrm{CH_3} \tag{5.82}$$

and

$$\mathrm{Mu} + \mathrm{C_2H_6} \rightarrow \mathrm{MuH} + \mathrm{C_2H_5} \tag{5.83}$$

and a representative plot, for the $\mathrm{Mu} + \mathrm{CH_4}$ reaction at 821 K, is given in Figure 5.7.

It should be noted that to attribute λ to a chemical reaction, it is necessary to be

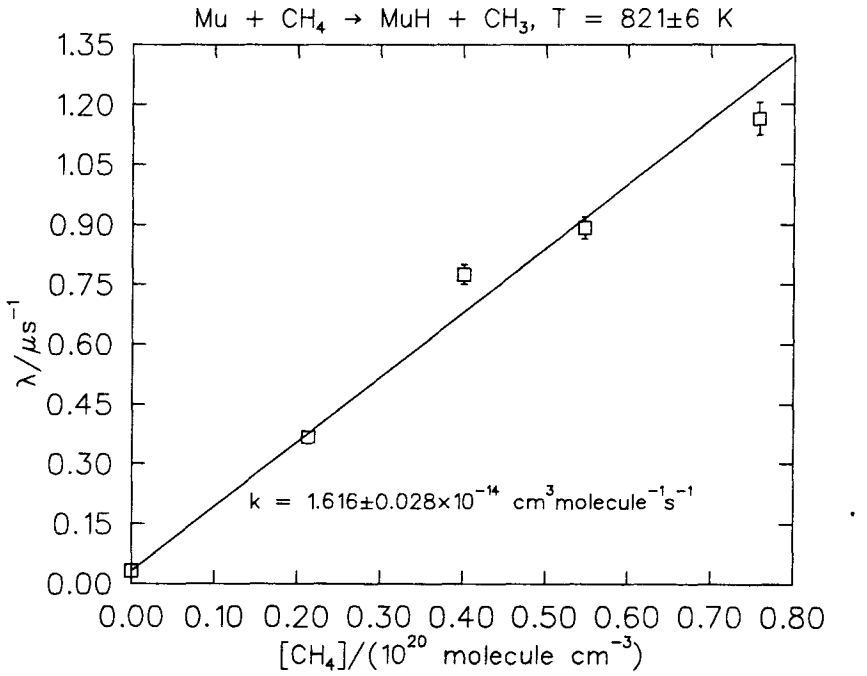

Figure 5.7: Fit of the rate coefficient of the reaction $\mathrm{Mu} + \mathrm{CH_4} \rightarrow \mathrm{MuH} + \mathrm{CH_3}$. Rate coefficient k fitted on plot of measured relaxation rates λ versus concentration of reactant, at 821 K, by linear least-squares. At each $\mathrm{CH_4}$ concentration, two measurements were made, with that shown in the figure the average. All measurements included in the fit of k.

certain that no other processes occur to relax the Mu signal. In the present study, the only other processes competing with the reactions above to any degree are the Mu bimolecular substitution reactions displacing H. In the case of CH_4, experimental and theoretical studies [31] show the bimolecular substitution reaction to be ~20 kcal/mol in E_a above that of abstraction, indicating that the signal relaxation due to substitution is negligible compared to the abstraction reaction. For C_2H_6 it is also to be expected that the substitution reaction would be far above the abstraction reaction in E_a.

Earlier measurements of the same type have included the hydrogen abstraction from H_2, reaction (1.8) mentioned in Chapter 1, as well as the gas-phase reactions [34,96]

$$\mathrm{Mu} + \mathrm{X_2} \rightarrow \mathrm{MuX} + \mathrm{X} \tag{5.84}$$

and

$$\mathrm{Mu} + \mathrm{HX} \rightarrow \mathrm{MuH} + \mathrm{X} \tag{5.85}$$

with $\mathrm{X} = \mathrm{F}, \mathrm{Cl}, \mathrm{Br}$. Similar techniques have been used to measure Mu gas-phase addition reactions such as [97]

$$\mathrm{Mu} + \mathrm{C_2H_4} \rightarrow \mathrm{C_2H_4Mu} \tag{5.86}$$

as well as gas-phase spin exchange of Mu (spin flip of the Mu atom electron from collisions in the medium) with Cs atoms [98] and O_2 [99]. Also measured have been many solution-phase Mu reaction rates (e.g. [100]) and hyperfine parameters of gas-phase muonated radicals [101] (some by integral μSR). As mentioned earlier with regards to μ^+ slowing down, epithermal μ^+ and Mu processes have been studied in gases, including N_2, CH_4, C_2H_6, and C_3H_8 [102,103]. Among the many muon experiments *not* employing μSR, recent measurements of physical-chemical interest include observation [104] of chemiluminescence in μ^+-irradiated Ne gas, assigned to electronic transitions of the Rydberg molecule NeMu.

5.2 μSR Experiments at TRIUMF

TRIUMF, a cyclotron particle accelerator, accelerates H^- ions to a beam of high velocities by repeatedly having them transverse a region of high voltage produced by a huge capacitor-like device [106]. The ions are stripped of their electrons yielding protons at a kinetic energy of 500 MeV. The beam travels down a pipe of vacuum (a "beampipe") and then split several times, into a series of "beam channels." Some of these are available for nuclear and particle physics experiments. Of more current interest at TRIUMF are experiments employing pion and muon beams, for which one part of the initial beam is directed into the experimental area called the Meson Hall. The proton beam hits a series of pion production targets, of various substances such as carbon, beryllium, and water, to produce pions, both positive and negative, of various kinetic energies. Some of the pions are directed into secondary beam channels ("beamlines") used for experiments or biomedical applications, or to produce high-energy muons from "in-flight" decay.

For most μSR gas chemistry experiments, the useful pions are those that, at rest, decay to muons on the surface of the production target, producing a muon beam with essentially all of the rest mass energy difference $m_\pi c^2 - m_\mu c^2$, 4.1 MeV, converted to muon kinetic energy. Beams of muons in a small range about this average, called the *nominal* beam energy, are available for experiments, on TRIUMF beamlines M13, M15, and M20, and are called *surface muon* beams.

All beamlines consist of a series of magnets to keep the beam focused, and in the right direction. Focusing quadrupole magnets direct the beam particles towards the center of a square array of four magnets, of alternating polarities. Bending dipole magnets direct the particles in the beam, running between two pole faces of opposite polarity, around a series of angles depending on the particle velocities; only those

particles in a narrow range of velocity stay in the beampipe. The form of the magnetic force law $\mathbf{F} = e\mathbf{v} \times \mathbf{B}/c$ dictates the effect of the magnets on a distribution of velocities. From this law and the momentum-velocity relationship $\mathbf{p} = m\mathbf{v}$ it should also be evident that the average momentum delivered by a beamline is proportional to the magnetic fields, which are in turn proportional to the DC current delivered to the magnets. It is also clear that across a cross-section of the beam the average momentum will vary smoothly after passing one or more bending magnets. Dipole magnets are momentum selectors only and so do not remove positron contamination (typically $\sim$100 times the number of muons). DC separators, found at the end of each muon beamline (M15 has two), are large, high voltage capacitors with a crossed magnetic field; these remove the positrons, and also narrow the momentum range of the beam reaching the target. They also "rotate" the spins of the beam muons by precession and can be used to rotate the initial beam polarization to a preselected angle, typically 90° with respect to the initial direction. Also, vertical slits can be narrowed and widened to narrow or widen the momentum range sampled. Horizontal slits can be narrowed to further reduce the beam to optimum dictated by the logic circuit veto mechanisms. The magnets, separators and slits are collectively called beamline elements and are controlled by a computer program called TICS.

The M15 beamline is famous worldwide for its ability to deliver an intense beam of monoenergetic surface muons. In terms of "momentum bite", which is accelerator jargon for narrowness of the momentum distribution about the average of the beam (nominally 29.8 MeV/c, corresponding to muon energy 4.1 MeV), M15 is the best in the world. For gas chemistry experiments using μ^+ this feature is attractive because a narrow momentum distribution leads to a small background relaxation λ_0, through a more homogenous $\mathbf{B}$ field in the muon stopping distribution, than would be obtained for a wider distribution, giving higher quality data. For very slow chemical reactions

such as the title reactions, this feature is a necessity because the lowest measurable rate coefficients are of comparable magnitude to λ_0. Consequently the M15 beamline was requested and obtained for the present study. The beamline elements of M15 are shown in Figure 5.8.

5.3 Reaction Vessel for CH_4 and C_2H_6 Experiments

Preparation for the experiments reported in this thesis took far more work than the final collection of data, performed in two weeks in November 1992. The main task was the preparation of a reaction vessel appropriate to the conditions of the experiments, dictated by certain constraints. Specifically, the title reactions, as detailed in Chapter 4, were expected to be rather slow, and therefore to give a very low relaxation rate parameter λ. Consequently, moderately high reaction concentrations (partial pressures) and temperature range were considered necessary to achieve relaxation rates of detectable magnitude. The earlier experiments [37] of the same type for hydrogen gas (rate of reaction (1.8)) were used as a guide in deciding on the conditions to be used, estimated as temperatures 500–900 K and pressures up to 17 atm. The vessel had to be made of a material which could withstand such conditions, while being nonmagnetic, so that there would be no interference with the weak applied field $\mathbf{B}$. An earlier vessel designed for the hydrogen experiments was originally to be used, but developed a leak due to a design flaw [105].

Therefore, TRIUMF engineer G.S. Clark was asked to design a new, similar vessel, but this time following the world-recognized standards of the American Society of Mechanical Engineers (ASME) pressure vessel code wherever possible, with the expected behavior of the vessel estimated from the observed behavior of the original hydrogen vessel. The new vessel, delivered in July 1992, is essentially as shown in Figure 5.9,

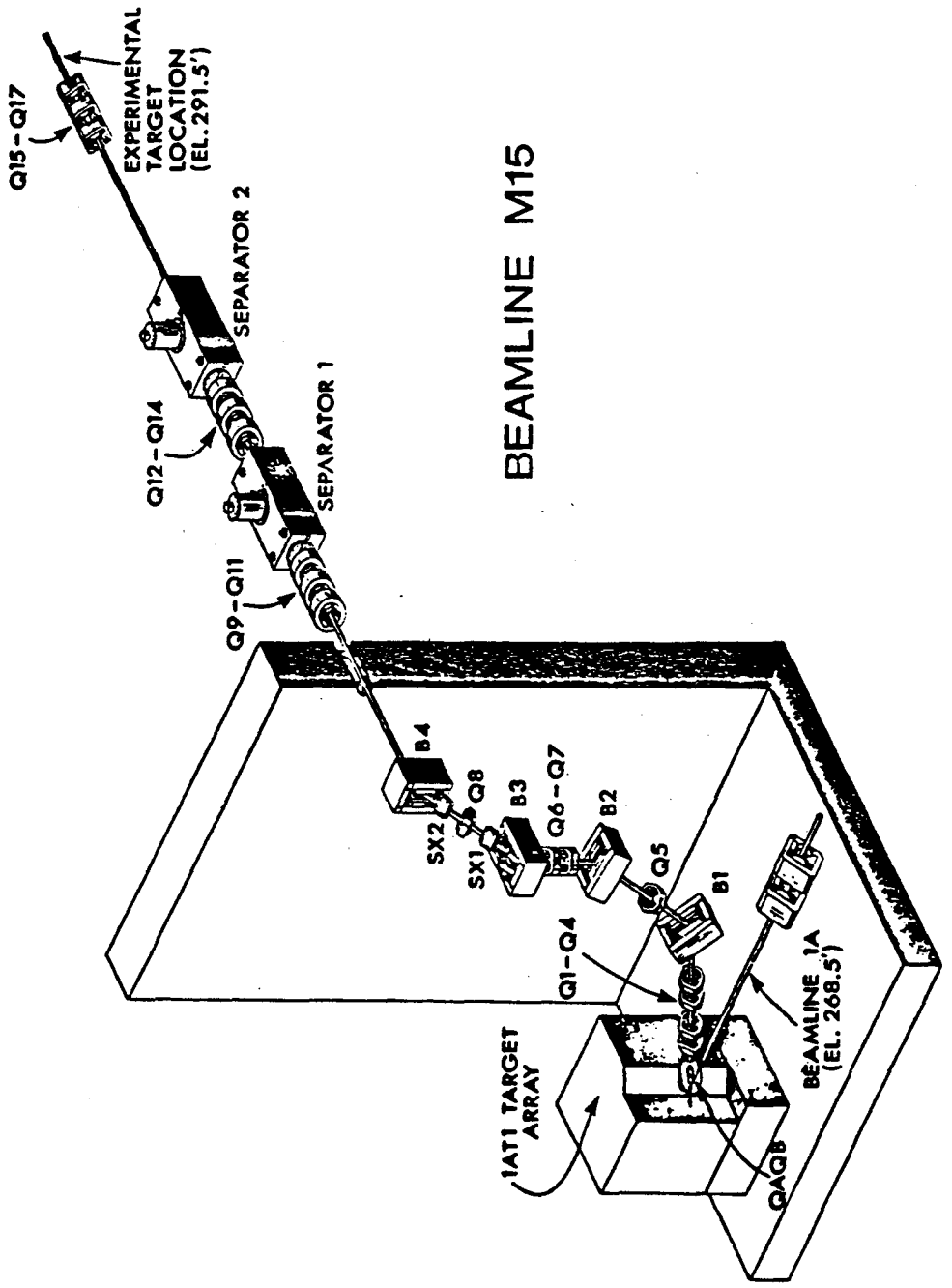

Figure 5.8: M15 secondary beam channel; reproduced from reference [106].

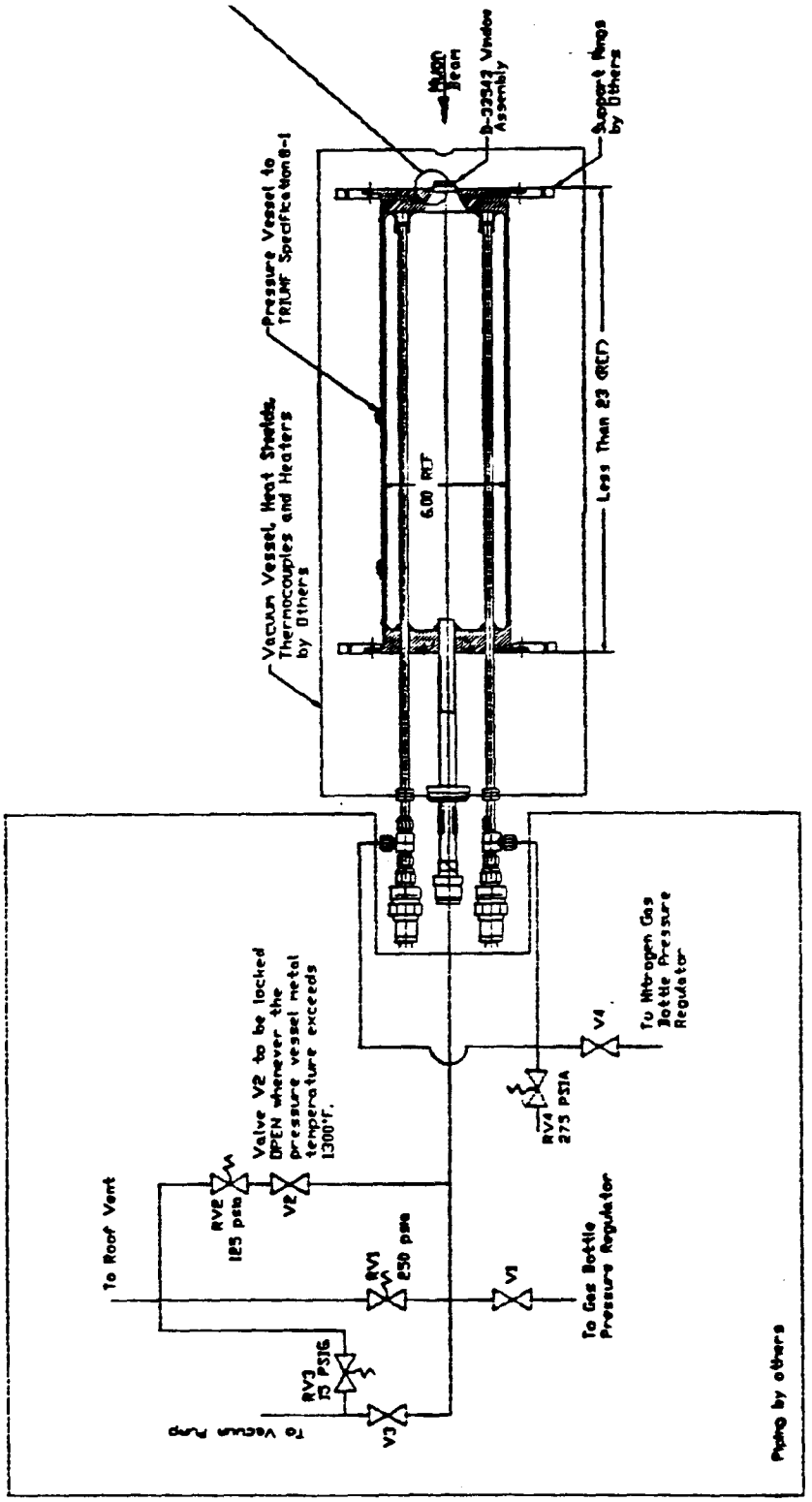

Figure 5.9: Diagram of reaction vessel used in present study; reproduced from reference [105]. Lengths are in inches.

reproduced from Mr. Clark's design note, reference [105].

The vessel is essentially a can with at one end, a thin muon entry window needed to allow the muon beam to pass into the reactant gas, and at the other, plumbing to allow the introduction and removal of gas. The "vacuum vessel" in the figure is mentioned later. The vessel, like the earlier counterpart was constructed of stainless steel because this material is essentially nonmagnetic. In the case of the present vessel, high carbon 316 stainless steel was used, to conform to the ASME code. The finished vessel does obey the code in every detail except for the window. Two details required much further development following receipt of the vessel: the window and the heating system.

5.3.1 Thin Muon Entry Window

The initial design of the window was essentially the same as that for the window used for the hydrogen vessel. It is shown in Figure 5.10. That window was made from 0.051 mm thick foil of inconel X–750 alloy (purchased from Metal Men), chosen for its heat-resistant qualities. The foil was formed to a dome under 5.5 MPa hydrostatic pressure, and welded onto a specially shaped 316 stainless steel ring, which was then itself welded to a hole at the head of the vessel. The dome forming gave a final product of approximately 0.043 mm thickness. No problems were ever experienced with that window [31], but that may have been merely good fortune, because the first window used on the present vessel study failed in high temperature/pressure safety testing. A second window broke in initial experimental runs. These occurred despite the fact that the windows were heat treated in an oven according to established ASME procedures to improve their resistance to shear stress. The window failures were of a gradual nature, with cracks appearing around the outside edge near the weld to the vessel. The failures were attributed to large forces developed in this region, which holds the entire window to the vessel, although the alloy [107] "is known to be susceptible to heat treatment

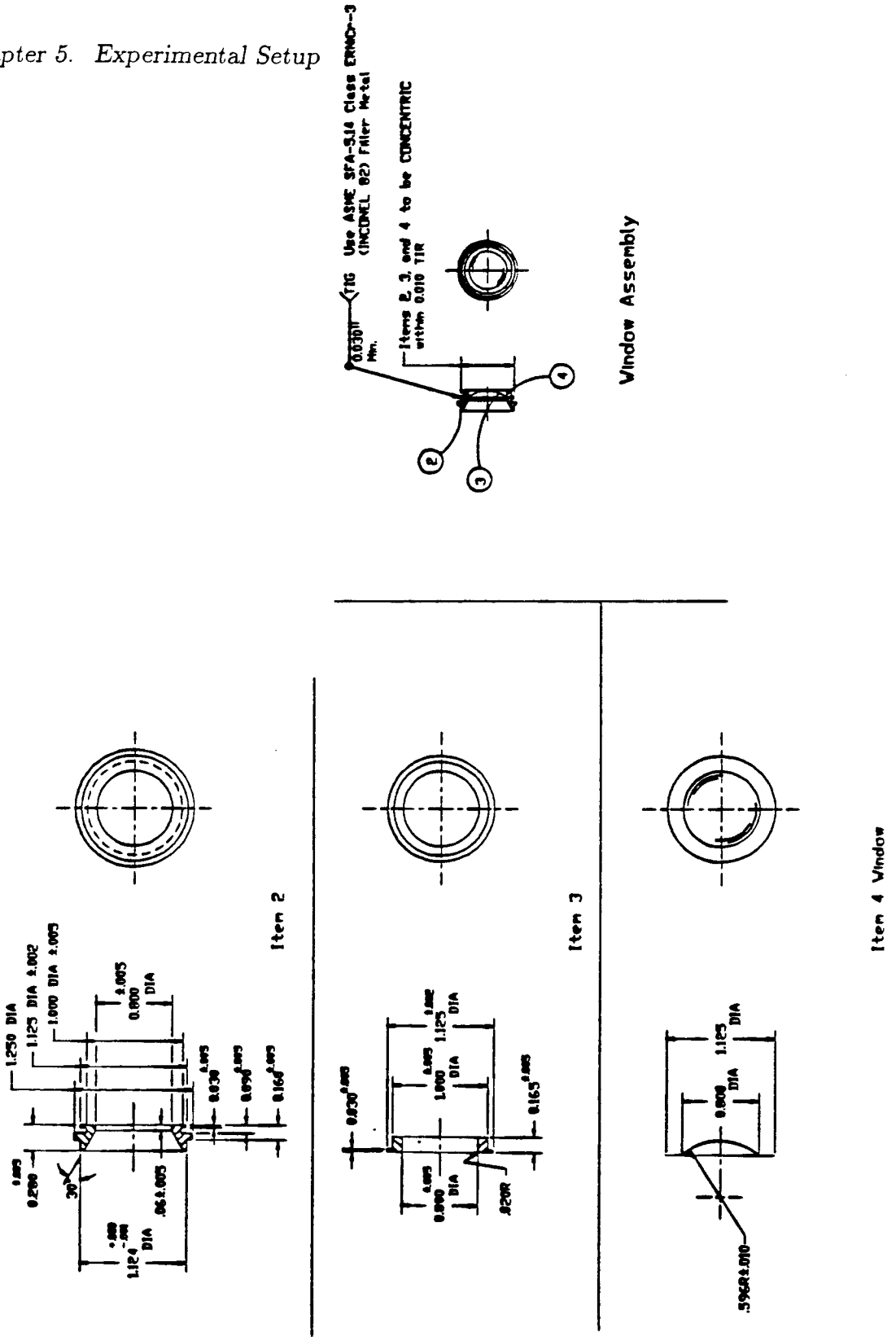

Figure 5.10: Design of the thin inconel window. Reproduced from reference [105]. Lengths are in inches.

embrittlement."

Following these failures in August 1992, a project was initiated to develop a window which could withstand the experimental conditions long enough to complete the experiments. The development essentially involved the use of different welding techniques (in TRIUMF's machine shop) to try to reduce the stress on the outside edge of the window during welding and in use. The heat treatment was omitted because it was judged to be of no advantage. Windows were then tested at conditions of high pressure and temperature, given in Table 5.4, more severe than those to be used in the experiments.

The tests were carried out by welding the windows, in the same manner as with the vessel, to specially-designed small, thick-walled vessels termed "jigs" with tubes to allow introduction of nitrogen gas for the tests. The jigs were placed in an oven with holes for the gas tubes, and heated to the temperatures given in the table. Nitrogen was added to the given pressures, and the pressure monitored with a gauge added to the plumbing. For some tests, after the pressure held for a while, the pressure was increased. For each test, the gas held at the given pressures for the times given. A few tests, not shown, were also performed on two types of 0.076 mm thick inconel foil which, curiously, were found to be inferior to the 0.051 mm foil. The thicker foils developed cracks in their grain structure when formed to domes.

Examination of the table clearly shows the progress made in improving the windows, though it is also clear that even the best of the windows can not be realistically expected to indefinitely withstand the experimental conditions. Window leak test failures *immediately after welding*, not shown on the table, also declined, and in the final batch of windows, none failed this test. In the beam time of November 1992, the window on the vessel lasted for the entire two weeks, then failed as the setup was being

Table 5.4: Selected results of tests of 0.051 mm thick inconel windows.

test	window temperature (°F)	pressure (psi)	time held
1	1250	255	3 min
		300	3 min
		340	4 min
		390	7 min
		450	5 min
		510	10 min
2	1250	256	5 min
		313	7 min
		400	5 min
3	1250	240	2.5 hr
		300	1 min
4	1250	150	17 hr
		200	1.5 hr
		250	1 hr
5	1100	150	4.2 hr
		250	3.5 days
6	1100	250	3.5 days
7	1250	150	4 days
	1150	300	2 days

prepared for dismantlement!

5.3.2 Heating of the Vessel

The metal used for the can, high carbon 316 stainless steel, while very nearly nonmagnetic, is a very poor heat conductor. To prevent heat loss, the vessel, like its predecessor, was mounted in a larger 316 stainless steel vessel which was continuously pumped to a good ($\sim 10^{-5}$ torr at the pump) vacuum. Also, thin copper and aluminum heat shields, their thinness dictated by the necessity of detecting escaping decay positrons,

minimized radiative heat loss. Cylindrical shields covered the curved part of the (inner) vessel, and flat circular shields the flat window end. In the beam path, the heat shields had circular holes cut which were occupied by much thinner heat shields. Two, nearest the inconel window, were of gold foil 0.0013 mm thick; four shields beyond this were of 0.0051 mm thick aluminum foil. Beyond this, the vacuum vessel had a muon entry window, of 0.051 mm thick aluminized mylar. The vessel was heated by heaters mounted on the plumbing end. This was necessitated by the fact that heaters around the curved surface would be likely to cause magnetic fields that would interfere with the applied field **B**.

The older hydrogen vessel, after considerable effort [37], had had a satisfactory heating system, but it involved the use of tapped holes in the plumbing end. TRIUMF safety officials required that, in keeping with the ASME code, no holes could be drilled into the new vessel's plumbing end, and so a new way of heating the vessel needed to be found. An additional constraint was the fact that the plumbing end is rather small, 15 cm in diameter, with large tubes taking up some of this space. Initially, two flat electrical contact heaters, purchased from Omega Industries, Inc. were initially (August 1992) mounted to the plumbing end. These heaters had a series of tiny coils of rather thin resistance wire, sheathed in a chromium alloy, and a maximum rating of 1000 W each. When used at high temperature in vacuum, these tended to short-circuit, resulting in immediate destruction. When these failed in experimental use, it was necessary to find another heating method, and to do some tests in advance of the November 1992 beam time, in order to be sure there would be no heater failure when trying to collect data.

While the technical details of heating the vessel are not of great scientific interest, the lack of data regarding the heating of a metal surface in a vacuum is remarkable. A large number of specialists were contacted, very few with any information. Contact

heaters specifically for vacuum were recently added to the Omega catalogue, but were judged too expensive. The eventual conclusion was to use tubular contact heaters from the same manufacturer. These heaters, approximately 51 cm long, 1.2 cm in diameter, consisted of a single thick resistance wire, with a few cm at each end of low resistance wire, sheathed in an inconel alloy. They had rating 1000 W each; three were welded to a thick stainless steel plate, mounted by bolts from another thick steel plate, to the vessel. It was hoped that the welding would result in good heat transfer from the heaters, allowing them to heat the vessel without being damaged by excessive heat. Two of these heaters failed in initial testing; none during experiments.

5.4 Measurement of the Title Reaction Rates

For the present study the vessel was placed, window facing the incoming μ^+ beam, between a pair of Helmholz coils (parallel circular DC current loops) 1.5 m in diameter, which produce a field "homogenous to 0.1% over a volume of 10 L" [37]. A field of $\sim$4 G was applied; this field, fitted as a parameter of $S(t)$, need not be initially known with great accuracy. Above and below the reaction vessel were two sets of two positron counters, used to collect two separate double-coincidence MSR signals.

All gas samples were purchased from Canadian Liquid Air. Nitrogen moderator gas was ultra-high purity grade ($\geq$ 99.999% pure), the ethane gas research grade ($\geq$ 99.98%), and the methane, superpure grade ($\geq$ 99.99%). Pressures over $\sim$2 atm were measured using a Borden test gauge (Matheson), and lower pressures with a Baratron capacitance pressure gauge (MKS Instruments, Inc.). Gas samples were introduced through a system of plumbing kept over 1 atm pressure at all times, except during pumping, to prevent any possibility of inward leak of air. The density corresponding to a given pressure was different at different points in the vessel because the

temperature within was not uniform (see later discussion) but again invoking the very good ideal gas behavior of the sample gases, it is to be expected that density would vary smoothly with temperature, resulting in uniform pressure throughout the gas system.

Temperatures in the gas were measured by a series of type E thermocouples (Omega) inserted through tubes passing into the vessel. The thermocouples shown in the figure as being on the outside of the vessel were for monitoring for safety purposes as well as to help identify temperature equilibrium. The temperature was controlled by an Omega temperature controller receiving its input from one of the thermocouples on the plumbing end of the vessel. At equilibrium the window was typically ~200 K cooler than the plumbing end, with the gas somewhat hotter than the window. Interestingly, for a given temperature controller setting, equilibrium temperatures rose with increasing CH_4 or C_2H_6 concentration relative to N_2.

Some discussion is in order here regarding the temperature error bars used in the Arrhenius plots of the next chapter. The addition of the heavy steel plates to mount the heaters apparently greatly reduced the radiative heat loss at the plumbing end. The result was that fairly large temperature gradients developed in the gas, typically ~50 K from one end to the other of the vessel. It is therefore necessary to determine which set of thermocouples gave the best indication of the actual temperature at the muon stopping region. Calculations using standard formulae (from reference [108]), standard data (from reference [109]), and M15 calibration data, show the average muon range at the lowest electron density in any of the experiments was less than 18.2 cm. The same μ^+ momentum setting was used for all experiments, so for all others the average range was less.

The stopping muons were closest, in every case, to a set of thermocouples in the gas located ~3 cm from the window end. These thermocouples, one above and one below the level of the beam, generally differed from each other by ~8 K. For a given

temperature point on the Arrhenius plots, the temperature uncertainty reported is the difference between the maximum and minimum readings for all of the runs at that temperature. The resulting estimated uncertainties are still modest, ~5–10 K. With the muon range increasing with increasing T, because of decreasing electron density with the same initial muon momentum, T may be systematically underestimated as it increases. However, this is expected to be a small effect, because the Arrhenius plot fits of the next chapter have reasonably small estimated uncertainties in the calculated parameters.

Chapter 6

Results and Discussion

The pseudo-first order rate coefficients (recall equation (2.25)) are calculated at each experimental temperature, for each of the two title reactions, according to the methods developed in the previous chapters. Two independent histograms for each run were collected, and fitted as separate data points, but averaged in the final plot for clarity. The fits giving each of the experimental rate coefficients are shown in the Appendix, with the 821 K fit also shown in the previous chapter. For each reaction, the rate coefficients are fitted by standard nonlinear least-squares procedures to the standard Arrhenius form $k = A\exp(-E_a/\mathrm{R}T)$, over the temperature ranges 626–821 K and 511–729 K for Mu + CH_4 and Mu + C_2H_6 respectively. They are shown in Figures 6.11 and 6.12. The data fit in the figures is shown in tabular form in Tables 6.5 and 6.6 along with the calculated Arrhenius parameters, and compared with those of the H atom variant, in Table 6.7, along with k values at selected temperatures. The errors in the Mu rate coefficients are due to counting statistics only.

Omitted from the C_2H_6 data are data taken above the temperature 729 K, which deviated very strongly from the straight line formed by the lower T points. This deviation was attributed to "cracking" of C_2H_6 to form appreciable concentrations of C_2H_4, whose addition reaction with muonium is considerably faster than the Mu reaction with C_2H_6 [97]. The C_2H_4 forms at an appreciable rate [23] from C_2H_6, compared to the reaction rate of Mu + C_2H_6, the rate-limiting step of this process being, interestingly enough, the rate of the corresponding reaction of H + C_2H_6. Indeed,

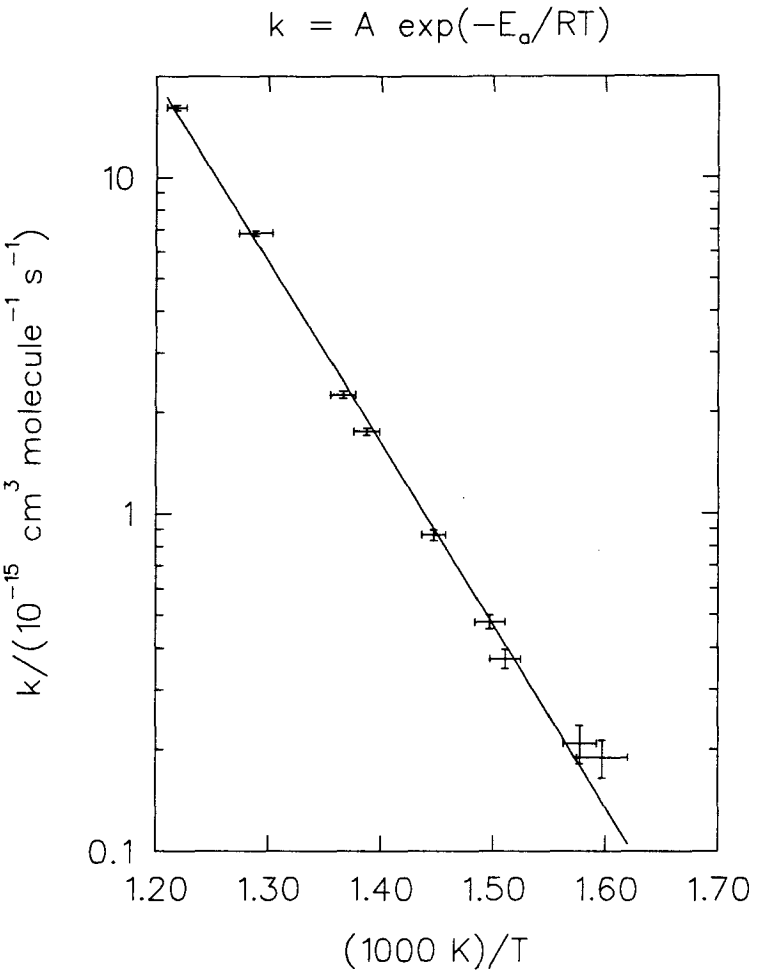

Figure 6.11: Arrhenius Plot for $Mu + CH_4 \rightarrow MuH + CH_3$.

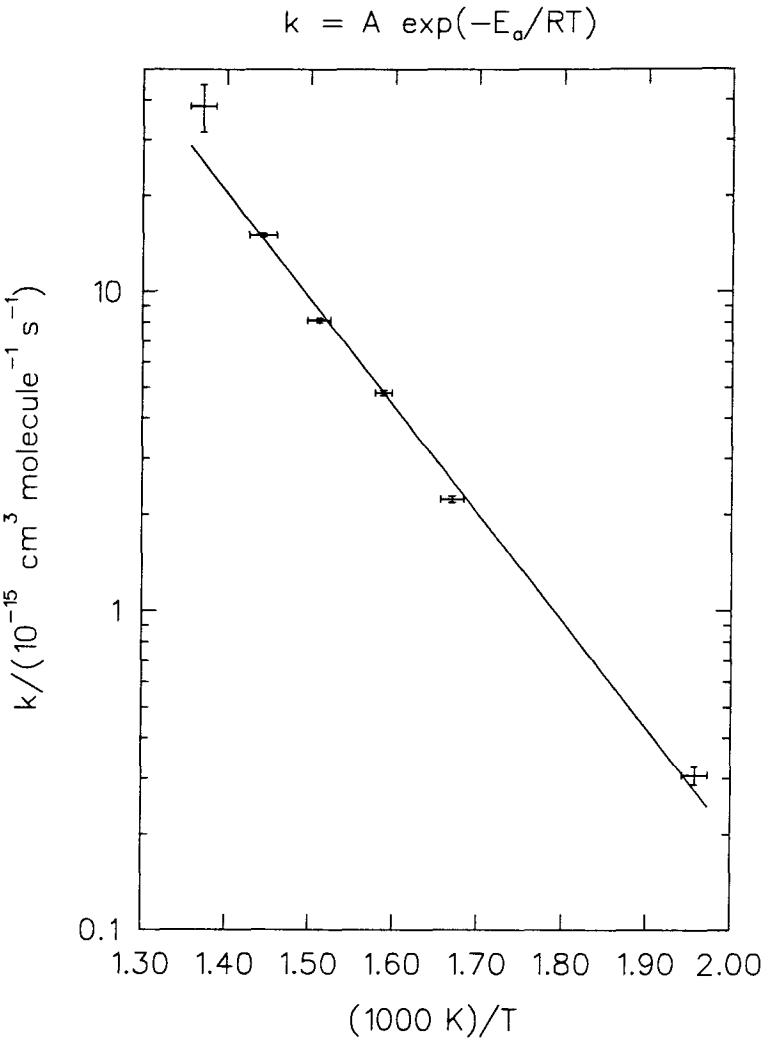

Figure 6.12: Arrhenius Plot for $Mu + C_2H_6 \rightarrow MuH + C_2H_5$.

Table 6.5: Measured Rate Coefficients for $Mu + CH_4 \rightarrow MuH + CH_3$.

T/K	k/(cm^3 molecule^{-1} s^{-1})
626 ± 9	$1.890 \pm 0.243 \times 10^{-16}$
634 ± 6	$2.082 \pm 0.272 \times 10^{-16}$
662 ± 6	$3.710 \pm 0.240 \times 10^{-16}$
668 ± 6	$4.778 \pm 0.225 \times 10^{-16}$
691 ± 5	$8.631 \pm 0.328 \times 10^{-16}$
721 ± 6	$1.748 \pm 0.044 \times 10^{-15}$
732 ± 6	$2.250 \pm 0.055 \times 10^{-15}$
776 ± 9	$6.818 \pm 0.117 \times 10^{-15}$
821 ± 6	$1.616 \pm 0.028 \times 10^{-14}$
$E_a = 24.66^{+0.88}_{-0.82}$ kcal/mol	
$A = 5.7^{+4.8}_{-2.5} \times 10^{-8}$ cm^3 molecule^{-1} s^{-1}	
$\chi^2 = 2.9$	

Table 6.6: Measured Rate Coefficients for $Mu + C_2H_6 \rightarrow MuH + C_2H_5$.

T/K	k/(cm^3 molecule^{-1} s^{-1})
511 ± 4	$3.066 \pm 0.202 \times 10^{-16}$
599 ± 5	$2.229 \pm 0.049 \times 10^{-15}$
630 ± 4	$4.793 \pm 0.090 \times 10^{-15}$
662 ± 6	$8.097 \pm 0.134 \times 10^{-15}$
693 ± 8	$1.500 \pm 0.021 \times 10^{-14}$
729 ± 8	$3.825 \pm 0.656 \times 10^{-14}$
$E_a = 15.35^{+0.65}_{-0.59}$ kcal/mol	
$A = 1.0^{+0.7}_{-0.4} \times 10^{-9}$ cm^3 molecule^{-1} s^{-1}	
$\chi^2 = 5.6$	

Table 6.7: Comparison of Mu and H Atom Data for Title Reactions. H atom data from reference [6].

Reaction	$E_a(\mathrm{Mu}) - E_a(\mathrm{H})$	$A_{\mathrm{Mu}}/A_{\mathrm{H}}$	$k_{\mathrm{Mu}}/k_{\mathrm{H}}$ (620 K)	$k_{\mathrm{Mu}}/k_{\mathrm{H}}$ (720 K)
$Mu(H) + CH_4$	11.5 kcal/mol	180	1/62	1/17
$Mu(H) + C_2H_6$	5.6 kcal/mol	3.2	1/28	1/15

short runs taken above 729 K were observed to have increasing λ with time from the introduction of the gas. The highest T point retained for the fit, at 729 K, deviates slightly above the line of the fit, indicating some C_2H_4 formation at this T.

The most remarkable feature of both Arrhenius plots are the rather large values of E_a, particularly for CH_4. The E_a values are also very large in comparison with the values for the corresponding H atom reactions at comparable temperatures, taken from reference [6]. The Arrhenius parameters and k values at selected temperatures (from the plots) are compared, for both title reactions, in Table 6.7. The E_a value for these reactions, 24.55 kcal/mol for CH_4 and 15.35 kcal/mol for C_2H_6, are surely among the highest ever measured for abstraction reactions of H, as are the E_a differences, $E_a(\mathrm{Mu}) - E_a(\mathrm{H})$, of 11.5 and 5.6 kcal/mol respectively. For the C_2H_6 reaction, the ratio $A_{\mathrm{Mu}}/A_{\mathrm{H}}$, 3.2, is near the 2.9 expected from the "trivial" isotope effect (see discussion of reaction cross-section in Chapter 2) due to isotopic mass ratios. The ratio for CH_4 is less reasonable but within an order of magnitude; such a large error in A can be gotten from a very small error in slope (E_a) on a logarithmic scale for k. However, both fits look reasonable and linear, with no obvious sign of curvature. Quantum tunneling is therefore not likely to be an important factor in the dynamics these reactions, in the temperature range studied.

The E_a differences seem too high to be accounted for by the V^{G} (vibrationally adiabatic barrier) difference between the isotopic variants. To see this for CH_4, it is necessary to examine the vibrational states of CH_4 and the transition state CH_4–H. (The corresponding information is not available for C_2H_6–H.) These are shown in the correlation diagram of Figure 6.13, adapted from reference [26] with the wavenumbers shown also from that reference. Three of the transition state frequencies are strongly correlated with CH_3 frequencies with almost no change in value and so should change very little on substitution H $\rightarrow$ Mu to give the transition state CH_4–Mu. This

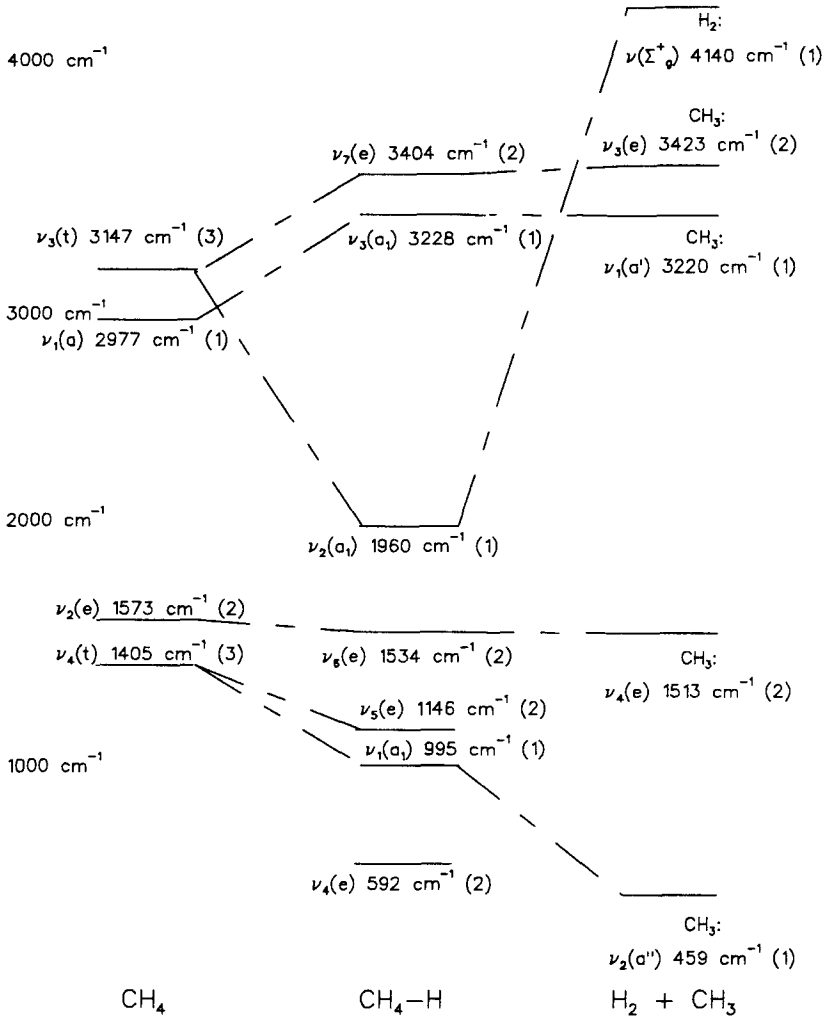

Figure 6.13: Correlation Diagram H + CH_4 → CH_4–H → H_2 + CH_3. At left are vibrational energy levels of CH_4; in centre, of CH_4–H; at right, of CH_3 + H_2. For each energy level, symmetry species, degeneracies, and wavenumber in cm^{-1} are shown. The energy levels and degeneracies, which assume harmonicity, are from the POL-CI calculations of Schatz *et al.*, reference [26]. The correlations, also given in that reference, are shown as dashed lines. For reference 349.75 $cm^{-1} \equiv 1$ kcal/mol.

Table 6.8: Standard Enthalpies of Title Reactions and H Atom Variants. Also given in Chapter 1.

Reaction	$\Delta H°$
$H + CH_4 \rightarrow H_2 + CH_3$	−2.6 kcal/mol
$Mu + CH_4 \rightarrow MuH + CH_3$	+4.9 kcal/mol
$H + C_2H_6 \rightarrow H_2 + C_2H_5$	−3.1 kcal/mol
$Mu + C_2H_6 \rightarrow MuH + C_2H_5$	+4.4 kcal/mol

is borne out by the comparison of Schatz *et al.* [26] of the transition states CH_4–H and CH_4–D. First noting that there is no zero-point energy difference in the reactants in going from H to Mu, and multiplying Schatz' *et al.* zero point energy difference by the ratio $\sqrt{m_D/m_\mu}$, an estimated E_a difference of only 1.9 kcal/mol is obtained. Comparing these TS's, the E_a for the reaction involving Mu is raised by much more than the zero point energy difference.

However, this comparison assumes no change in the *location* of the transition state CH_4–Mu as compared to the TS CH_4–H. It is likely that the respective transition states have very different locations. To see this, compare the reaction enthalpies of the two reactions, mentioned in Chapter 1, and shown here in Table 6.8. Also included in the table are the reaction enthalpies for the corresponding reactions of C_2H_6. Noting that the H atom reactions are exothermic, while the Mu reactions are endothermic, very different reaction barrier locations can be expected in comparing CH_4–H to CH_4–Mu or C_2H_6–H to C_2H_6–Mu. As has been discussed many times, the geometrical character of PES's causes exothermic reactions to have, in general, *early* barriers, in which the TS is relatively similar to the separated reactants. Similarly, for endothermic reactions, the TS will be relatively similar to the separated products. For the $Mu + CH_4$ reaction, the TS CH_4–Mu can be expected to be shifted towards products, whose vibrational

energy is much higher than that of the H + CH_4 transition state CH_4–H, due to the much lighter mass of Mu compared to H, which results in much higher vibrational frequencies. This combined with the isotopic shifts in vibrational energy, chiefly due to energy difference of MuH and H_2, could produce a drastic increase in the TS zero-point energy. A similar effect for H abstraction from C_2H_6 would be expected.

Some comparison with the previous measurements [37] for the reaction

$$Mu + H_2 \rightarrow MuH + H \tag{6.87}$$

is in order here. In this case the H atom variant is thermoneutral whereas the Mu variant is endothermic by 7.5 kcal/mol, and the E_a is 4.8 kcal/mol higher for Mu than for H [74]. As with the reactions of the present study this likely represents differing TS location in the isotopic variants, given the very different thermochemistry of the two reactions. VTST calculations [110] on the Mu and H variants of this reaction show the collinear TS to differ in geometry drastically, with the TS H_2–Mu much closer to products than the H atom variant H_2–H, which is symmetric with respect to the two H–H bond lengths.

The E_a difference, for CH_4 at least, is still too high to be explained by zero-point energy differences of the TS's. However, some of the difference might be explainable in terms of differences in dynamics for *excited states* of CH_4 with Mu compared to H. In the temperature range 626–821 K, the equilibrium concentration of vibrationally excited CH_4 is substantial. Even so, the extra vibrational energy is not comparable to the E_a difference of Mu/H. Using experimental wavenumbers listed in reference [70], CH_4 has an average of ~0.4 kcal/mol excess vibrational energy at 626 K, and at 821 K, ~1.0 kcal/mol. For the transition state, assuming harmonicity of the vibrational motion and using the theoretical calculations of Schatz *et al.*, the excess is ~1.2 kcal/mol at 626 K, ~2.3 kcal/mol at 821 K. Again, this is not comparable to the E_a difference.

Table 6.9: Estimated vibrational wavenumbers of the CH_4–Mu transition state, estimated from the corresponding CH_4–H wavenumbers of Schatz *et al.*, also given here, assuming harmonicity and using corresponding calculated CH_4–D wavenumbers.

Mode (Degeneracy)	Wavenumber in CH_4–H (cm^{-1})	Wavenumber in CH_4–Mu (cm^{-1})
ν_1 (1)	995	1017
ν_2 (1)	1960	3480
ν_3 (1)	3228	3228
ν_4 (2)	592	717
ν_5 (2)	1146	1187
ν_6 (2)	1534	1532
ν_7 (2)	3404	3406

The CH_4–Mu transition state wavenumbers estimated from this reference are shown in Table 6.9.

In the expected transition state structure CH_4–H, from the theoretical MP results (see Chapter 3), the leaving H atom is relatively far removed from the CH_3 group. Given this structure, it is certainly reasonable to expect that vibrationally excited CH_4, in which the average C–H distance is higher than for the ground state, will have a higher reaction probability with H. For the Mu variant, the leaving H atom will likely be even farther removed in the TS. As well, for Mu, with a higher average velocity than H, it is also reasonable to assume that the reaction probability will increase faster with average C–H distance, and H–C–H angles, for Mu than for H; Mu is expected due to higher average velocity to more easily approach the leaving H atom on noncollinear paths than H, which should become more important for a longer C–H distance and greater H–C–H angles.

The result of this hypothesis is that the rate coefficient depression in the substitution H $\rightarrow$ Mu should be less for excited CH_4 states than for the ground state, leading to

Table 6.10: Fit of CH_4 rate data to equation (6.88).

Parameter	Value
E	21.9 kcal/mol
A	3.6×10^{-10} cm^3 molecule^{-1} s^{-1}
A_4	16.6
A_2	109

a high apparent E_a, since the excited states form an exponentially higher fraction of the total as temperature increases. The same hypothesis is also applicable to the abstraction reaction from C_2H_5, whose H/Mu E_a difference is also very high.

To try to explore the source of the high value of E_a for the CH_4 reaction, the data was fit to a function of the form

$$k = \frac{Ae^{-E/RT}(1 + 3A_4e^{-(\nu_4+\Delta E_4)/RT} + 2A_2e^{-(\nu_2+\Delta E_2)/RT})}{1 + 3e^{-\nu_4/RT} + 2e^{-\nu_2/RT}} \tag{6.88}$$

with the wavenumbers ν_4 and ν_2 converted to energy using 349.75 cm^{-1} $\equiv$ 1 kcal/mol. This expression is intended to show differing reaction rates for the first two excited states of CH_4, the only ones of significant population up to 821 K. In this equation, ν_4 (= 1405 cm^{-1}, triply degenerate) and ν_2 (= 1573 cm^{-1}, doubly degenerate) are the wavenumbers corresponding to these vibrational states. Thus the denominator is the partition function. This expression is constructed to be of the form of equation (2.13), an average of k over excited states of the reactant CH_4. The parameters ΔE are the differences between the excited state energies above the ground state in CH_4, and the energies of the TS excited states to which they correlate. These energies are from the PES of Schatz *et al.* (The TS states to which ν_4 correlate were averaged.) The parameters A_4 and A_2 represent pre-exponential factors for ν_4 and ν_2 relative to the ground state of CH_4. The results are shown in Table 6.10. The fit is not of good quality;

the estimated uncertainties could not be established, and the fit certainly should not be taken very seriously. However the results are at least in the expected direction—the ground-state E_a is lowered, and the pre-exponential factors are higher for the excited states. Also, the overall pre-exponential factor is closer to that expected from the Mu/H mass ratio than for the fit of the standard expression $k = A\exp(-E_a/\mathrm{R}T)$.

Chapter 7

Conclusion

In this study, reaction rates for the gas-phase abstraction by Mu of H from each of CH_4 and C_2H_6 have been measured using μSR over the temperature ranges 626–821 K and 511–729 K respectively. The usual Arrhenius plots for each data set are linear, with reasonably small estimated uncertainties in the calculated parameters. Any large degree of tunneling in these reactions for the temperature ranges studied is not evident. The E_a for the two reactions, 24.66 and 15.35 kcal/mol respectively, are 11.5 and 5.5 kcal/mol higher than for the corresponding H atom reactions.

In the absence of theoretical calculations, the large E_a increases seem to indicate drastic differences between the Mu and H variants of the title reactions, in location of the transition states on the potential energy surfaces. As well, the reaction rates of the excited vibrational states of CH_4 and C_2H_6 with Mu seem to be reduced less in comparison with the rates with H, than are their ground states.

More cannot be said about the isotope effects on the reaction dynamics until theoretical or state-selected data, or more Mu kinetic data with gas-phase polyatomic molecules, are available. Since this is the first study of Mu kinetics in the gas-phase with molecules of this size, it may be, like the product internal state correlations of Germann *et al.* [43,44] on the same reactions, that these results are only "anomalous" in comparison with results from smaller molecules.

Bibliography

[1] Wilson, S., Diercksen, G.H.F., eds., "Methods in Computational Molecular Physics", Plenum Press, New York, 1991.

[2] Truhlar, D.G., ed., "Potential Energy Surfaces and Dynamics Calculations", Plenum Press, New York, 1981.

[3] Clary, D.C., ed., "The Theory of Chemical Reaction Dynamics", D. Reidel, Dordrecht, Holland, 1986.

[4] Laganà, A., ed., "Supercomputer Algorithms for Reactivity, Dynamics and Kinetics of Small Molecules", Kluwer Academic Publishers, Dordrecht, Holland, 1988.

[5] Gonzalez-Lafont, A., Truong, I.N., Truhlar, D.G., *J. Chem. Phys.*, (1991) **95**, 8875.

[6] Tsang, W., Hampson, R.F., *J. Phys. Chem. Ref. Data*, (1986) **15**, 1087.

[7] Shaw, R.J., *J. Phys. Chem. Ref. Data*, (1978) **7**, 1179.

[8] Rabinowitz, M.J., Sutherland, J.W., Patterson, P.M., Klemm, R.B., *J. Phys. Chem.*, (1991) **95**, 674.

[9] Seewald, D., Wolfgang, R., *J. Chem. Phys.*, (1967) **47**, 143.

[10] Wolfgang, R., *Prog. Reaction Kinet.*, (1965) **3**, 97.

[11] Chou, C.C., Rowland, F.S., *J. Chem. Phys.*, (1969) **50**, 2763.

[12] Root, J.W., Rowland, F.S., *J. Chem. Phys.*, (1967) **46**, 4299.

[13] Lee, E.K.C., Rowland, F.S., *J. Am. Chem. Soc.*, (1963) **85**, 897.

[14] Ferro, L.J., Spicer, L.D., *J. Chem. Phys.*, (1978) **69**, 4335.

[15] Chattopadhyay, A., Tasaki, S., Bersohn, R., Kawasaki, M., *J. Chem. Phys.*, (1991) **95**, 1033.

[16] Kurilo, M.J., Timmons, R.B., *J. Chem. Phys.*, (1969) **50**, 5076.

[17] Gorban, N.I., Nalbandyan, A.B., *Zhur. fiz. Khim.*, (1962) **36**, 1757.

[18] Sepehrad, A., Marshall, R.M., Purnell, H., *J. Chem. Soc. Faraday Trans. 1*, (1978) **75**, 835.

[19] Fenimore, C.P., Jones, G.W., *J. Phys. Chem.*, (1961) **65**, 2200.

[20] Lede, J., Villermaux, J., *Can. J. Chem.*, (1978) **56**, 392.

[21] Jones, D., Morgan, P.A., Purnell, J.H., *J. Chem. Soc. Faraday Trans. 1*, (1977) **73**, 1311.

[22] Camilleri, P., Marshall, R.M., Purnell, J.H., *J. Chem. Soc. Faraday Trans. 1*, (1974) **70**, 1434.

[23] Cao, J.-R., Back, M.H., *Can. J. Chem.*, (1984) **62**, 86.

[24] Klein, R., McNesby, J.R., Scheer, M.D., Schoen, L.J., *J. Chem. Phys.*, (1959) **30**, 58.

[25] Kurilo, M.J., Hollinder, G.A., Timmons, R.B., *J. Chem. Phys.*, (1970) **52**, 1773.

[26] Schatz, G.C., Wagner, A.F., Dunning, Jr., T.H., *J. Phys. Chem.*, (1984) **88**, 221.

[27] Walker, D.C., "Muon and Muonium Chemistry", Cambridge University Press, New York, 1983.

[28] Fleming, D.G., Garner, D.M., Vaz, L.C., Walker, D.C., Brewer, J.H., Crowe, K.M., *Adv. Chem.*, (1979) **175**, 279.

[29] Baer, S., Fleming, D.G., Arseneau, D.J., Senba, M., Gonzalez, A. *in* "Isotope Effects in Gas-Phase Chemistry", p. 111, Kaye, J.A., ed., American Chemical Society, Washington, 1992.

[30] Fleming, D.G, Senba, M., *in* "Perspectives in Meson Science", p. 219, Yamazari, T., Nakai, K, Nagamine, K., eds., Elsevier Science Publishers, Amsterdam, 1992.

[31] Fleming, D.G., TRIUMF proposal for Experiment 641, 1991.

[32] Tennyson, J., Miller, S., *J. Chem. Phys.*, (1989) **90**, 2524.

[33] Davies, J.W., Hanning-Lee, M.A., Pilling, M.J., Seakins P.W., *Spectrochim. Acta, Part A*, (1990) **46A**, 581.

[34] Gonzalez, A.C., Reid, I.D., Garner, D.M., Senba, M., Fleming, D.G., Arseneau, D.J., Kempton, J.R., *J. Chem. Phys.*, (1989) **91**, 6164.

[35] Neuhauser, D., Baer, M., *J. Chem. Phys.*, (1989) **90**, 5882.

[36] Schatz, G.C., *J. Chem. Phys.*, (1985) **83**, 3441.

[37] Reid, I.D., Garner, D.M., Lee, L.Y., Senba, M, Arseneau, D.J, Fleming, D.G., *J. Chem. Phys.*, (1987) **86**, 5578.

[38] Steckler, R., Dykema, K.J., Brown, F.B., Hancock, G.C., Truhlar, D.G., *J. Chem. Phys.*, (1987) **87**, 7024.

[39] Gonzalez, J.C., McDouall, J.W., Schlegal, H.B., *J. Phys. Chem.*, (1990) **94**, 7467.

[40] Lu, D-h., Maurice, D., Truhlar, D.G., *J. Am. Chem. Soc.*, (1990) **112**, 6206.

[41] Pross, A., Yamataka, H., Nagase, S., *J. Phys. Org. Chem.*, (1991) **4**, 135.

[42] Weston, Jr., R.E., Flynn, G.W., *Ann. Rev. Phys. Chem.*, (1992) **43**, 559.

[43] Germann, G.J., Huh, Y-D., Valentini, J.J, *J. Chem. Phys.*, (1992) **96**, 1957.

[44] Germann, G.J., Huh, Y-D., Valentini, J.J, *J. Chem. Phys.*, (1992) **96**, 5746.

[45] Levine, I.N., "Quantum Chemistry", 4th. ed., Allyn and Bacon, Toronto, 1991.

[46] Viggiano, A.A., Morris, R.A., Van Doren, J.M., Paulson, J.F., *J. Chem. Phys.*, (1992) **96**, 275.

[47] Levine, R.D., Bernstein, R.B., "Molecular Reaction Dynamics and Chemical Reactivity", Oxford University Press, New York, 1987.

[48] Johnston, H.S., "Gas Phase Reaction Rate Theory", Ronald Press, New York, 1966.

[49] Li, Y.S., Wilson, K.R., *J. Chem. Phys.*, (1990) **93**, 8821.

[50] Rivail, J.L., *in* "New Theoretical Concepts for Understanding Organic Reactions", p. 219, Bertrán, J., Csizmadia, eds., Kluwer Academic Publishers, Dordrecht, Holland, 1989.

[51] Bertrán, J., *in* "New Theoretical Concepts for Understanding Organic Reactions", p. 231, Bertrán, J., Csizmadia, eds., Kluwer Academic Publishers, Dordrecht, Holland, 1989.

[52] Berne, B.J., Borkovec, M., Straub, J.E., *J. Phys. Chem.*, (1988) **92**, 3711.

[53] Laidler, K.J., "Chemical Kinetics", 3rd ed., Harper & Row, Philadelphia, 1987.

[54] Cyvin, S.J., ed., "Molecular Structures and Vibrations", American Elsevier Publishing Company, New York, 1972.

[55] Fogarasi, G., *in* "Modelling of Structure and properties of Molecules", p. 191, Maksić, Z.B., ed., Ellis Horwood, Toronto, 1987.

[56] Gerber, R.B., Ratner, M.A., *Adv. Chem. Phys.*, (1988) **70, part 1**, 97.

[57] Jørgensen, P., Simons, J., eds., "Geometrical Derivatives of Energy Surfaces and Molecular Properties", D. Reidel, Dordrecht, Holland, 1986.

[58] Fogarasi, G., Pulay, P., *Ann. Rev. Phys. Chem.*, (1984) **35**, 191.

[59] Pulay, P., *Adv. Chem. Phys.*, (1987) **69, part 2**, 241.

[60] Bauschlicher, Jr., C.W., Langhoff, S.R., Taylor, P.R., *Adv. Chem. Phys.*, (1990) **77**, 103.

[61] Ehrenson, S., Newton, M.D., *Chem. Phys. Lett.*, (1972) **13**, 24.

[62] Jørgensen, P., Simons, J., "Second Quantization-Based Methods in Quantum Chemistry", Academic Press, Toronto, 1981.

[63] Simons, J., *J. Phys. Chem.*, (1991) **95**, 1017.

[64] Saunders, V.R., van Lenthe, J.H., *Mol. Phys.*, (1983) **48**, 923.

[65] Shepard, R., *Adv. Chem. Phys.*, (1987) **69, part 2**, 63.

[66] Werner, H.-J., *Adv. Chem. Phys.*, (1987) **69, part 2**, 1.

[67] Sokalski, W.A., Sawaryn, A., *J. Chem. Phys.*, (1987) **87**, 526.

[68] Murray, J.S., Redfern, P.C., Seminario, J.M., Politzer, P., *J. Phys. Chem.*, (1990) **94**, 2320.

[69] Friesner, R.A., *Ann. Rev. Phys. Chem.*, (1991) **42**, 341.

[70] Joseph, T., Steckler, R., Truhlar, D.G., *J. Chem. Phys.*, (1987) **87**, 7036.

[71] Raff, L.M., Stivers, L., Porter, R.N., Thompson, D.L., Sims, L.B., *J. Chem. Phys.*, (1970) **52**, 3449.

[72] Walch, S.P., *J. Chem. Phys.*, (1980) **72**, 4932.

[73] Schatz, G.C., Walch, S.P., Wagner, A.F., *J. Chem. Phys.*, (1980) **73**, 4536.

[74] Valentini, J.J., Phillips, D.L., *in* "Bimolecular Collisions", p. 1, Ashford, M.N.R., Baggot, J.E., eds., The Royal Society of Chemistry, London, 1989.

[75] Truhlar, D.G., Garrett, B.C., *Ann. Rev. Phys. Chem.*, (1984) **35**, 159.

[76] Kuppermann, A., *J. Phys. Chem.*, (1979) **83**, 171.

[77] Gonzalez-Lafont, A., Truong, T.N., Truhlar, D.G., *J. Chem. Phys.*, (1991) **95**, 8875.

[78] Truhlar, D.G., Kuppermann, A., *J. Am. Chem. Soc.*, (1971) **93**, 1840.

[79] Garret, B.C., Truhlar, D.G., *J. Phys. Chem.*, (1979) **83**, 200.

[80] Child, M.S., "Molecular Collision Theory", Academic Press, New York, 1974.

[81] Schatz, G.C., *in* reference [3], p. 1.

[82] Truhlar, D.G., *J. Phys. Chem.*, (1979) **83**, 188.

[83] Landau, R.H., "Quantum Mechanics II", Wiley, Toronto, 1990.

[84] Neuhauser, D., Baer, M., Judson, R.S., Kouri, D.J. *J. Chem. Phys.*, (1989) **90**, 5882.

[85] Feynman, R.P., Leighton, R.B., Sands, M., "The Feynman Lectures on Physics", vol. III, Addison-Wesley, Don Mills, Ontario, 1964.

[86] Ramachandran, B., Wyatt, R.E., *in* reference [4], p. 169.

[87] Walker, R.B., Light, J.C., *Ann. Rev. Phys. Chem.*, (1980) **31**, 401.

[88] Bunker, D.L., Pattengill, M.D., *J. Chem. Phys.*, (1970) **53**, 3041

[89] Valencich, T., Bunker, D.L., *J. Chem. Phys.*, (1974) **61**, 21.

[90] Garrett, B.C., Joseph, T., Truong, T.N., Truhlar, D.G., *Chem. Phys.*, (1989) **136**, 271.

[91] Lowry, T.H., Richardson, K.S., "Mechanism and Theory in Organic Chemistry", 3rd. ed., Harper & Row, New York, 1987.

[92] Senba, M., Arseneau, D.J., Fleming, D.G., *in* "Handbook of Hot Atom Chemistry", p. 232, Adloff, J.-P., Gasper, P.P, Imamura, M., Maddock, A.G., Matsuura, T., Sano, H., Yoshihara, K., eds., VCH Publishers, New York, 1992.

[93] Senba, M., Arseneau, D.J., Gonzalez, A.C., Kempton, J.R., Pan, J.J., Tempelmann, A, Fleming, D.G., *Hyp. Int.*, (1990) **65**, 793.

[94] Cox, S.F.J., *in* "Muons and Pions in Materials Research", p. 137, Chappert, J., Grynszpan, R.I., eds., Elsevier Science Publishers, Amsterdam, 1984.

[95] James, F., Roos, M., MINUIT, CERN Computer 7600 Interim Program Library (1971).

[96] Gonzalez, A.C., Tempelmann, A, Arseneau, D.J., Fleming, D.G., Senba, M., Kempton, J.R., Pan, J.J., *J. Chem. Phys.*, (1992) **97**, 6309.

[97] Garner, D.M., Fleming, D.G., Arseneau, D.J., Senba, M., Reid, I.D., *J. Chem. Phys.*, (1990) **93**, 1732.

[98] Pan, J.J., Arseneau, D.J., Kempton, J.R., Fleming, D.G., Baer, S., Gonzalez, A.C., Snooks. R., *Phys. Rev. A*, in press.

[99] Senba, M., Fleming, D.G., Arseneau, D.J., Garner, D.M., Reid, I.D., *Phys. Rev. A*, (1989) **39**, 3871.

[100] Roduner, E., Louwrier, P.W.F., Brinkman, G.A., Garner, D.M., Reid, I.D., Arseneau, D.J., Senba, M., Fleming, D.G., *Ber. Bunsenges. Phys. Chem.*, (1990) **94**, 1224.

[101] Pan, J.J., Fleming, D.G., Senba, M., Arseneau, D.J., Snooks, R., Baer, S., Hahn, M, Kiefl, R.F., Percival, P.W., Brodovitch, J.-C., Cox, S.F.J., work in progress.

[102] Kempton, J.R., Senba, M., Arseneau, D.J., Gonzalez, A.C., Garner, D.M., Pan, J.J., Fleming, D.G., Percival, P.W., Brodovitch, J.-C., Leung, S.-K., *J. Chem. Phys.*, (1991) **94**, 1046.

[103] Kempton, J.R., Arseneau, D.J., Fleming, D.G., Senba, M., Gonzalez, A.C., Pan, J.J., Tempelmann, A., Garner, D.M., *J. Phys. Chem.*, (1991) **95**, 7338.

[104] Baer, S., Fleming, D.G., Arseneau, D.J., Senba, M., Snooks, R., Pan, J.J., Sloan,J.J., work in progress.

[105] Clark, G.S., "Replacement High Temperature Pressure Vessel for Dr. Fleming", TRIUMF design note TRI-DN-92-3, 1992.

[106] TRIUMF User's Group Executive Committee, "TRIUMF User's Guide', July 1987.

[107] Hawbolt, E.B., private communication.

[108] Marmier, P., Sheldon, E., "Physics of Nuclei and Particles", v. 1, Academic Press, New York, 1969.

[109] Greeniaus, L.G., "TRIUMF Kinematics Handbook", 2nd. ed., 1987.

[110] Garrett, B.C., Steckler, R., Truhlar, D.G. *Hyp. Int.*, (1986) **32**, 779.

Appendix A

Plots of Relaxation Rate Data

This appendix comprises the fits of the relaxation rates measured by μSR to the equation

$$\lambda = k[\mathrm{HR}] + \lambda_0$$

where k is the pseudo-first order rate coefficient for the title reactions, and R is CH_4 or C_2H_6. There are nine plots for the reaction

$$\mathrm{Mu} + \mathrm{CH_4} \rightarrow \mathrm{MuH} + \mathrm{CH_3}$$

and six for

$$\mathrm{Mu} + \mathrm{C_2H_6} \rightarrow \mathrm{MuH} + \mathrm{C_2H_5}$$

and the parameters k obtained from these are plotted in the Arrhenius plots of Chapter 6.

In each plot, each point shown represents two independent measurements of λ: one taken from a histogram collected by counters above the reaction vessel, and one from counters below the vessel. These are averaged in the plot for clarity but treated as independent in fitting the straight line. In general these are within one standard deviation of each other.

Runs of zero reactant are pure N_2 ("λ_0") runs. Others were done in every case such that muon stopping density was constant.

Following each plot is a table showing the concentrations of reactant with the (averaged) measured relaxation rate λ.

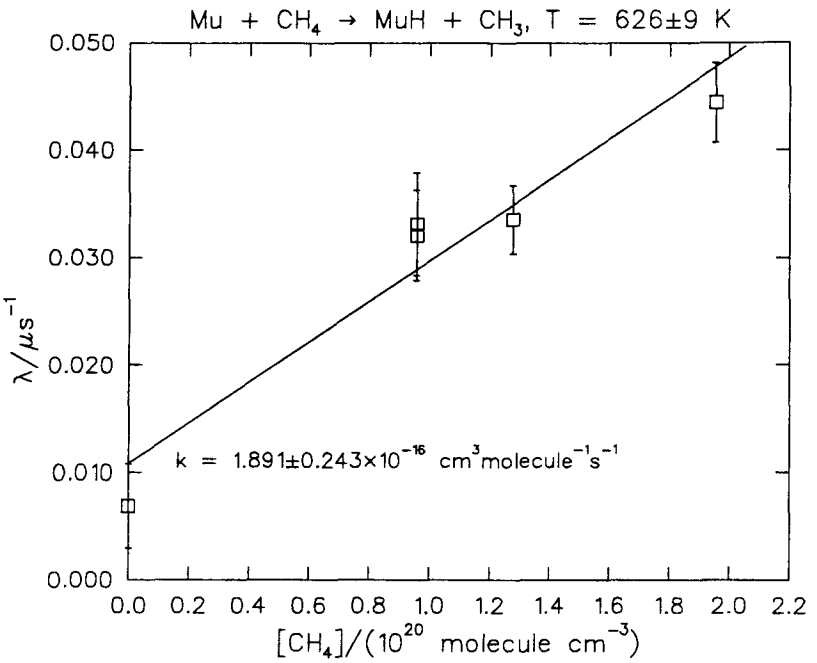

$[CH_4]/(10^{20}$ molecule $cm^{-3})$	$\lambda/\mu s^{-1}$
0	0.006841 ± 0.003909
1.084	0.032131 ± 0.004217
1.084	0.033157 ± 0.004768
1.445	0.033575 ± 0.003176
2.212	0.044450 ± 0.003713

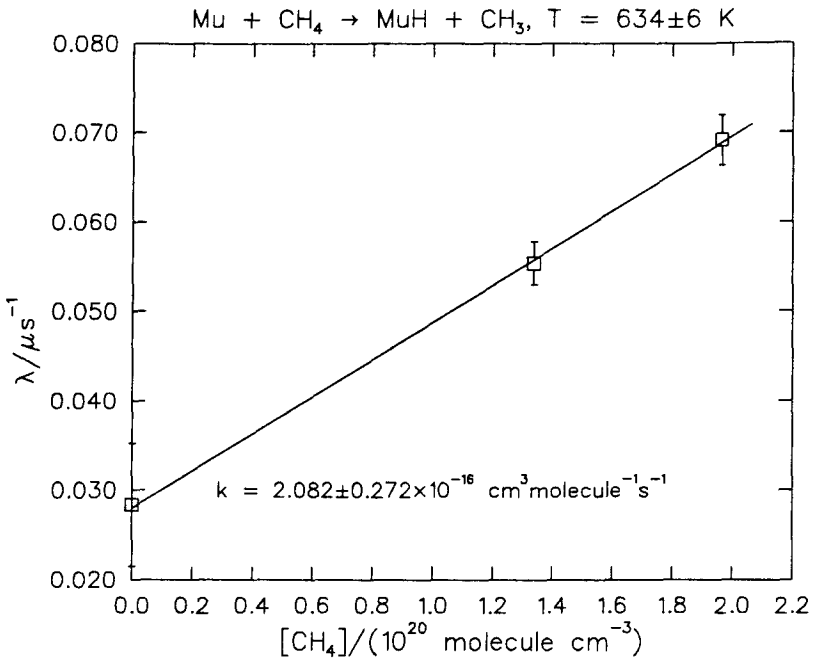

$[CH_4]/(10^{20}$ molecule $cm^{-3})$	$\lambda/\mu s^{-1}$
0	0.028330 ± 0.006849
1.338	0.055432 ± 0.002441
1.964	0.069139 ± 0.002808

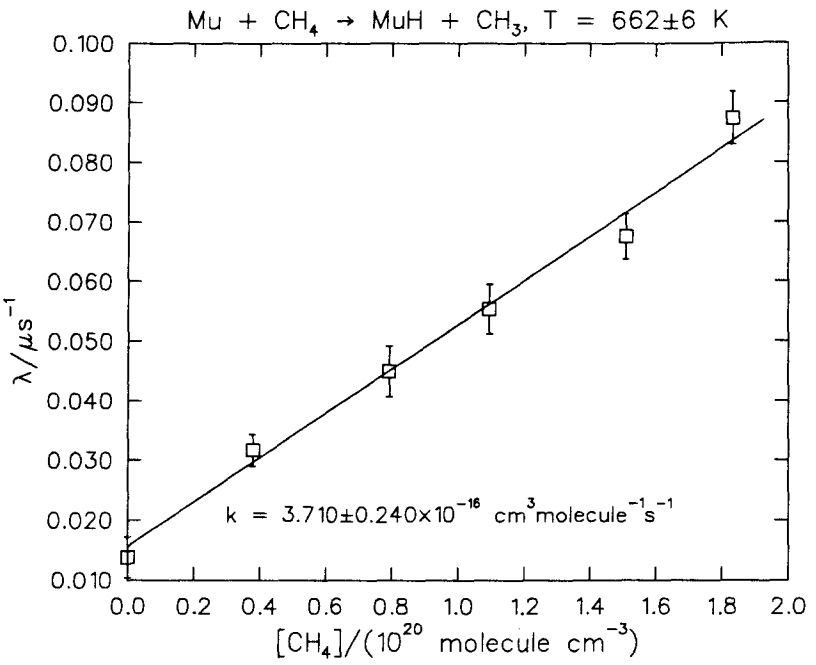

$[CH_4]/(10^{20}$ molecule $cm^{-3})$	$\lambda/\mu s^{-1}$
0	0.013785 ± 0.003416
0.3772	0.031677 ± 0.002656
0.7921	0.044984 ± 0.004239
1.094	0.055439 ± 0.004140
1.509	0.067621 ± 0.003862
1.833	0.087387 ± 0.004411

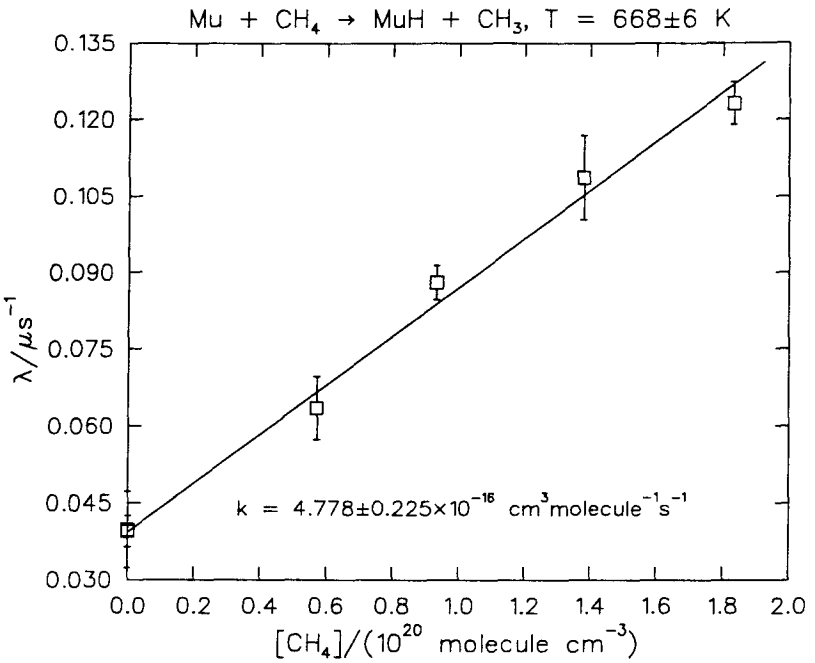

$[CH_4]/(10^{20}$ molecule $cm^{-3})$	$\lambda/\mu s^{-1}$
0	0.039469 ± 0.003038
0	0.039799 ± 0.007493
0.5710	0.063544 ± 0.006173
0.9328	0.088089 ± 0.003366
1.380	0.108702 ± 0.008252
1.832	0.123167 ± 0.004206

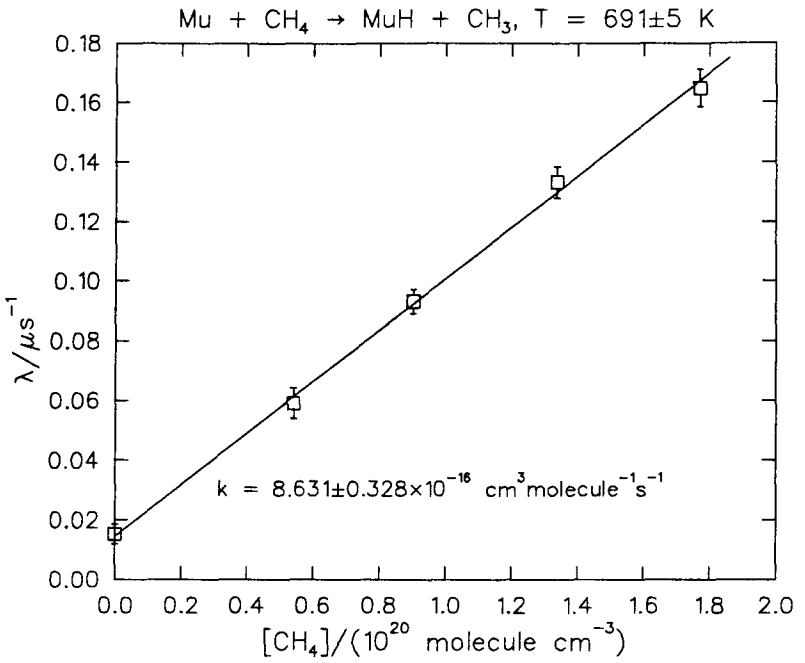

$[CH_4]/(10^{20}$ molecule cm$^{-3})$	$\lambda/\mu s^{-1}$
0	0.015220 ± 0.003289
0.5420	0.059092 ± 0.005121
0.9034	0.093238 ± 0.004016
1.337	0.133327 ± 0.005221
1.771	0.164787 ± 0.006295

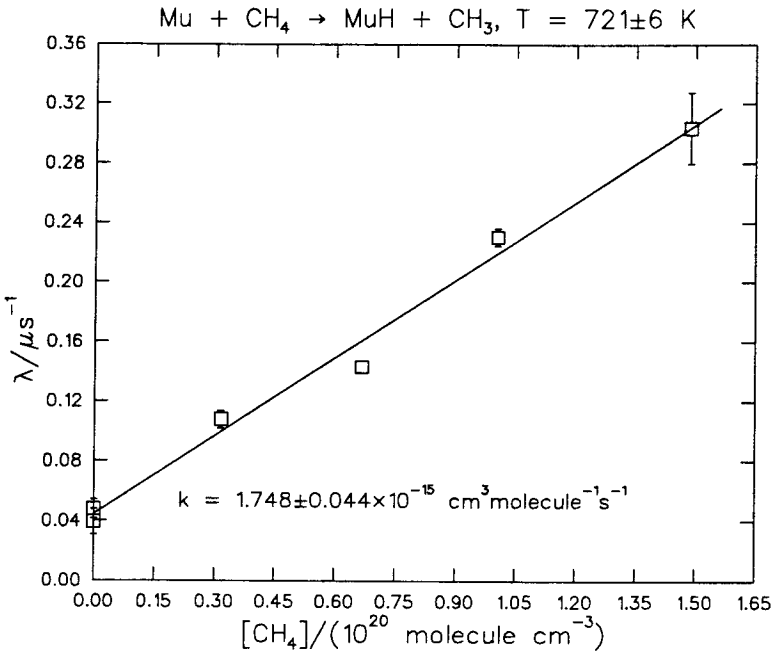

$[CH_4]/(10^{20}$ molecule cm$^{-3})$	$\lambda/\mu s^{-1}$
0	0.039229 ± 0.008633
0	0.047601 ± 0.006306
0.3160	0.107815 ± 0.005788
0.6671	0.143200 ± 0.004836
1.004	0.230634 ± 0.005752
1.487	0.303956 ± 0.024055

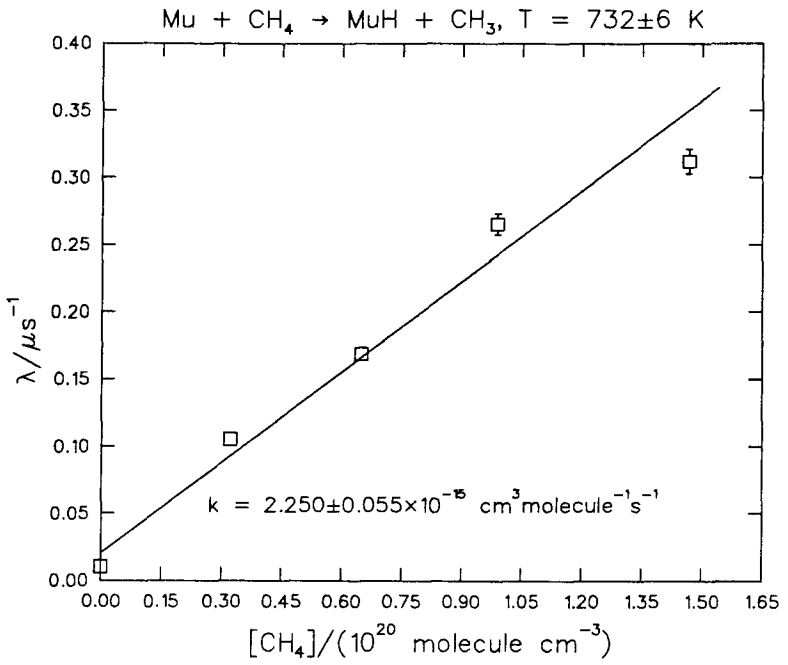

$[CH_4]/(10^{20}$ molecule $cm^{-3})$	$\lambda/\mu s^{-1}$
0	0.010411 ± 0.003647
0.3218	0.105085 ± 0.004592
0.6481	0.168750 ± 0.005412
0.9892	0.265820 ± 0.007877
1.467	0.312369 ± 0.009205

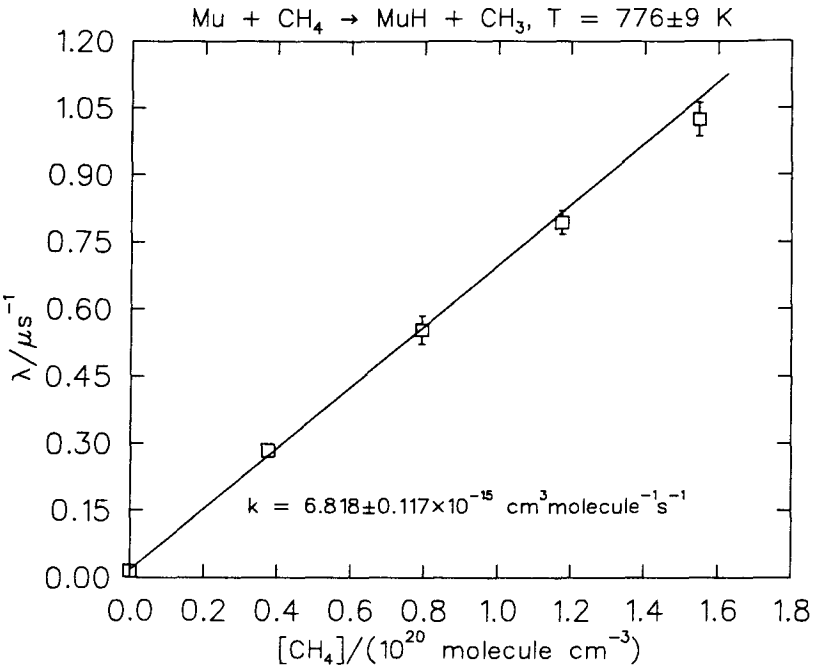

$[CH_4]/(10^{20}$ molecule $cm^{-3})$	$\lambda/\mu s^{-1}$
0	0.014257 ± 0.004089
0.3750	0.284509 ± 0.006473
0.7930	0.554011 ± 0.031405
1.175	0.794630 ± 0.025830
1.549	1.025124 ± 0.037914

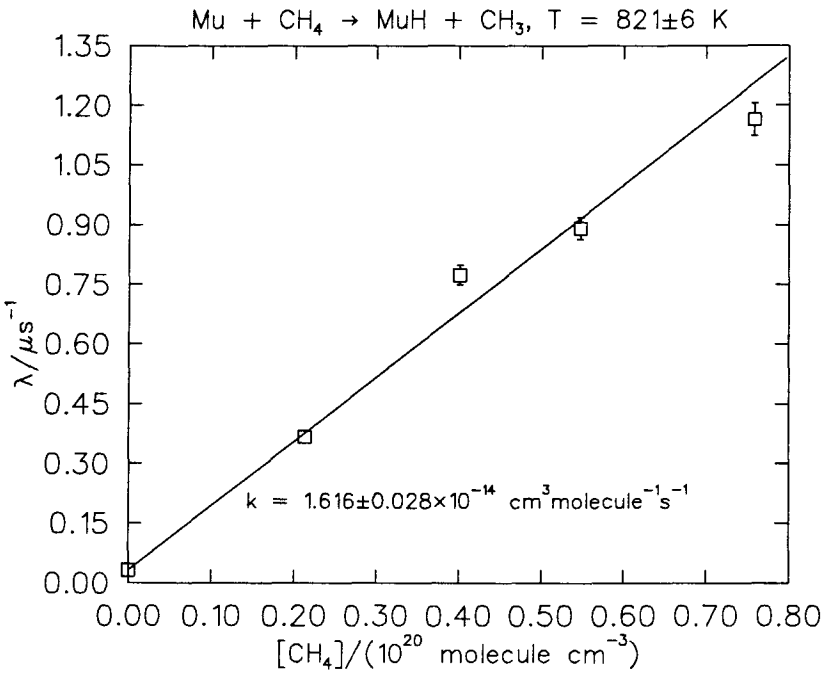

$[CH_4]/(10^{20}$ molecule $cm^{-3})$	$\lambda/\mu s^{-1}$
0	0.031125 ± 0.004847
0.2134	0.367023 ± 0.011344
0.4019	0.774750 ± 0.024708
0.5474	0.891673 ± 0.027794
0.7583	1.164704 ± 0.040282

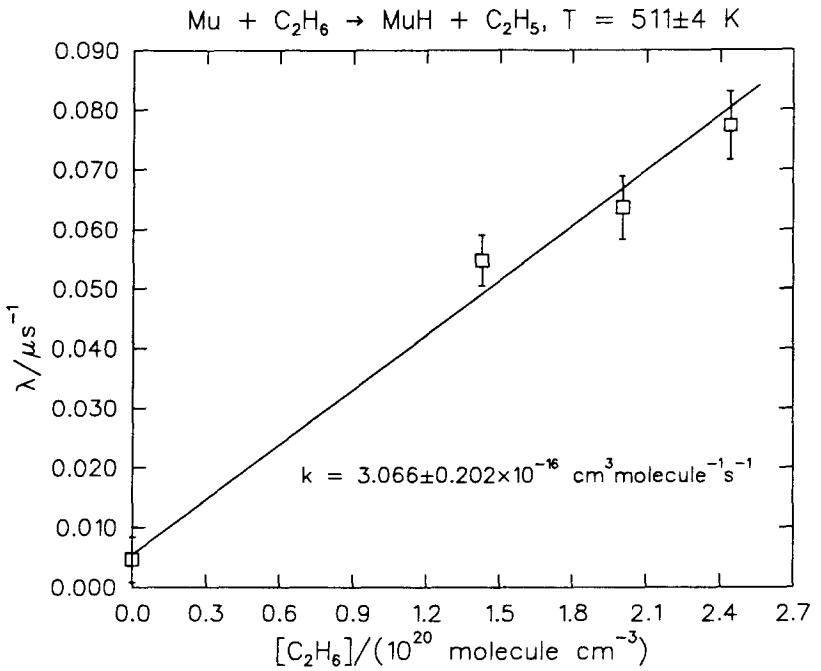

$[C_2H_6]/(10^{20}$ molecule $cm^{-3})$	$\lambda/\mu s^{-1}$
0	0.004630 ± 0.003799
1.426	0.054850 ± 0.004242
2.003	0.063688 ± 0.005297
2.442	0.077297 ± 0.005702

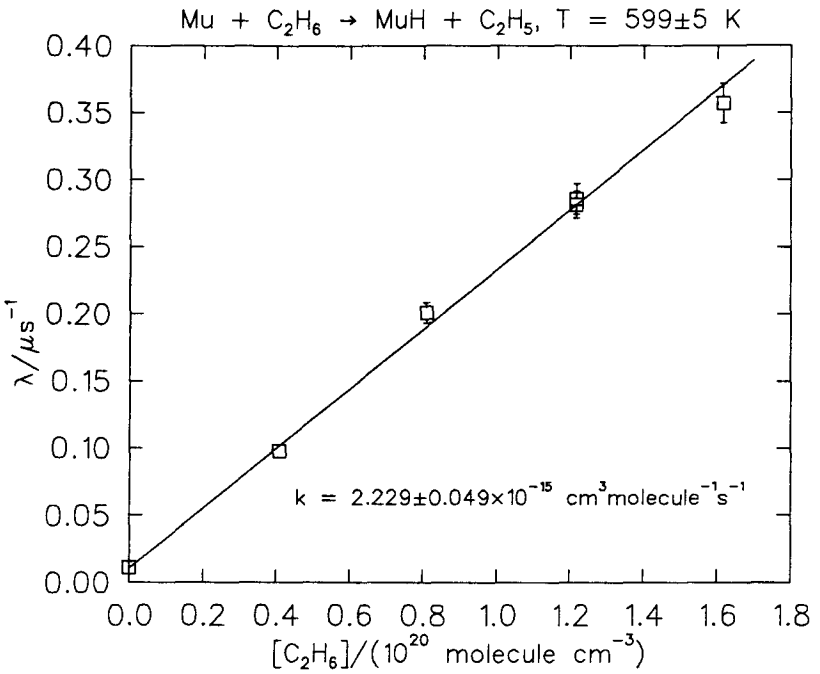

$[C_2H_6]/(10^{20}$ molecule cm$^{-3})$	$\lambda/\mu s^{-1}$
0	0.011852 ± 0.008264
0.4085	0.097486 ± 0.004722
0.8170	0.201049 ± 0.007798
1.217	0.281719 ± 0.009880
1.217	0.287138 ± 0.011072
1.634	0.357131 ± 0.014504

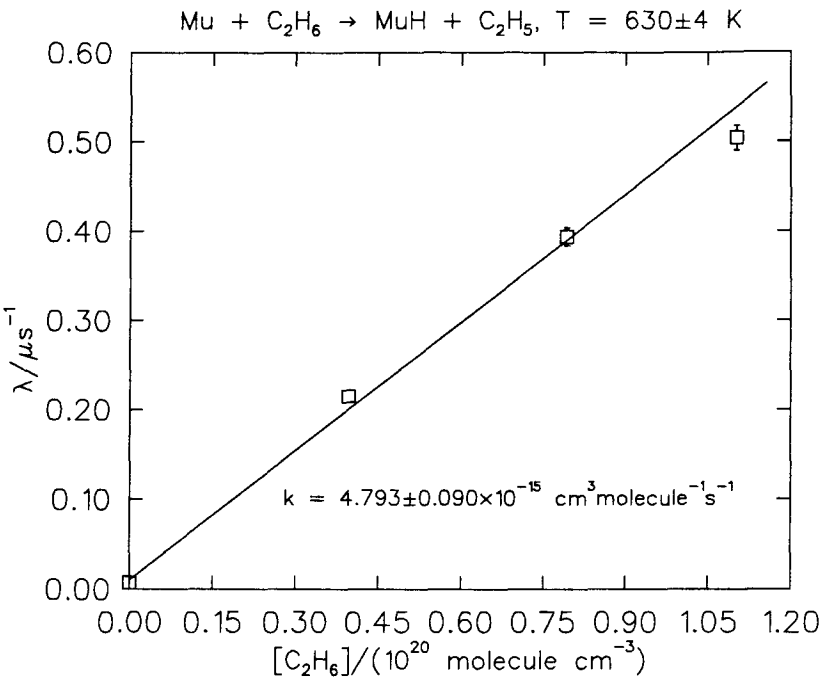

$[C_2H_6]/(10^{20}$ molecule cm$^{-3})$	$\lambda/\mu s^{-1}$
0	0.006841 ± 0.003909
0.3976	0.215061 ± 0.007666
0.7952	0.394024 ± 0.009662
1.105	0.504192 ± 0.013982

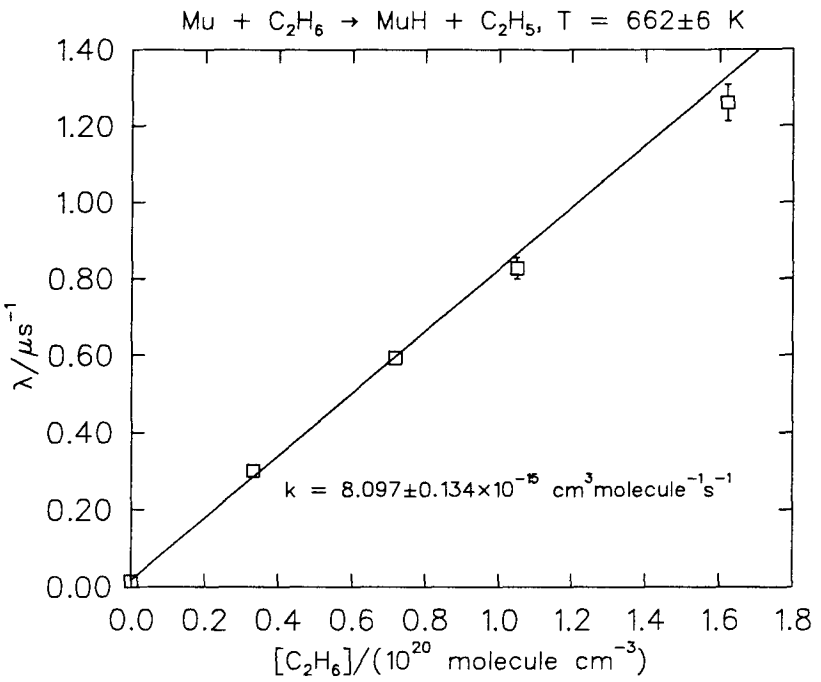

$[C_2H_6]/(10^{20}$ molecule cm$^{-3})$	$\lambda/\mu s^{-1}$
0	0.013774 ± 0.001681
0.3314	0.300854 ± 0.006900
0.7156	0.593513 ± 0.016879
1.047	0.828243 ± 0.028440
1.619	1.260624 ± 0.047012

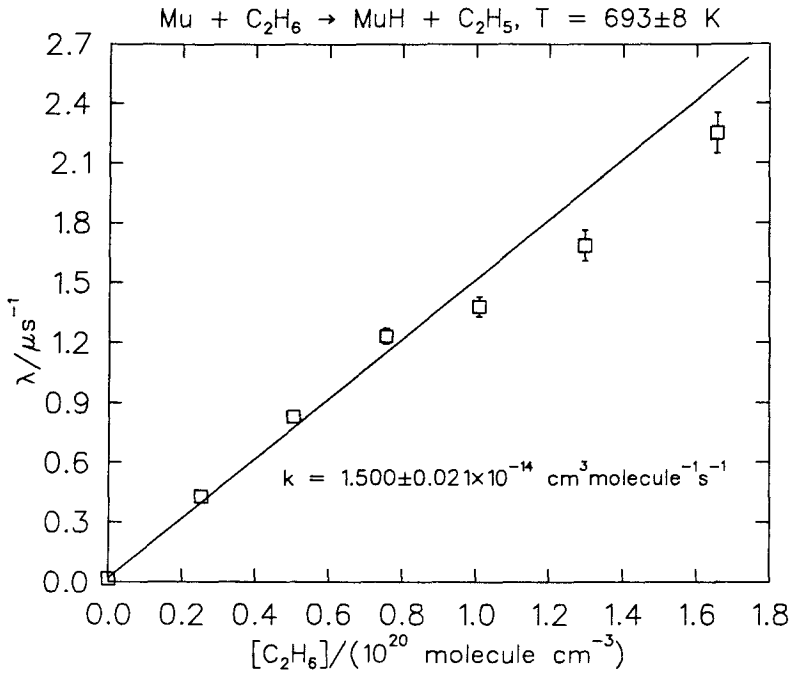

$[C_2H_6]/(10^{20}$ molecule cm$^{-3})$	$\lambda/\mu s^{-1}$
0	0.015220 ± 0.003289
0.2522	0.428846 ± 0.010048
0.5043	0.830209 ± 0.022343
0.7565	1.233618 ± 0.038823
1.009	1.380476 ± 0.049829
1.297	1.687174 ± 0.076420
1.657	2.251196 ± 0.103084

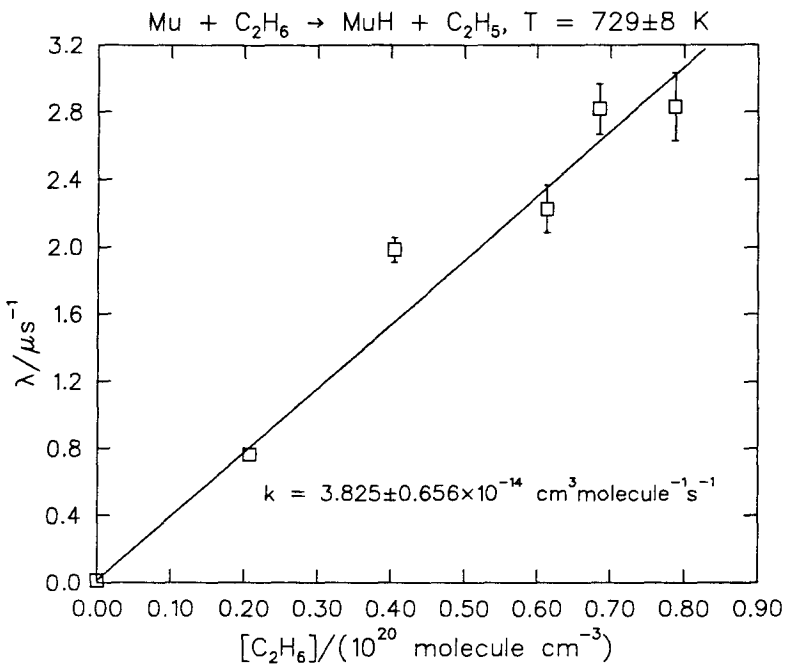

$[C_2H_6]/(10^{20}$ molecule $cm^{-3})$	$\lambda/\mu s^{-1}$
0	0.010411 ± 0.003647
0.2073	0.763854 ± 0.033779
0.4039	1.986954 ± 0.073391
0.6130	2.225998 ± 0.140749
0.6850	2.818614 ± 0.149635
0.7878	2.829827 ± 0.201463